Predictive Deadbeat Control For PMSM Drive

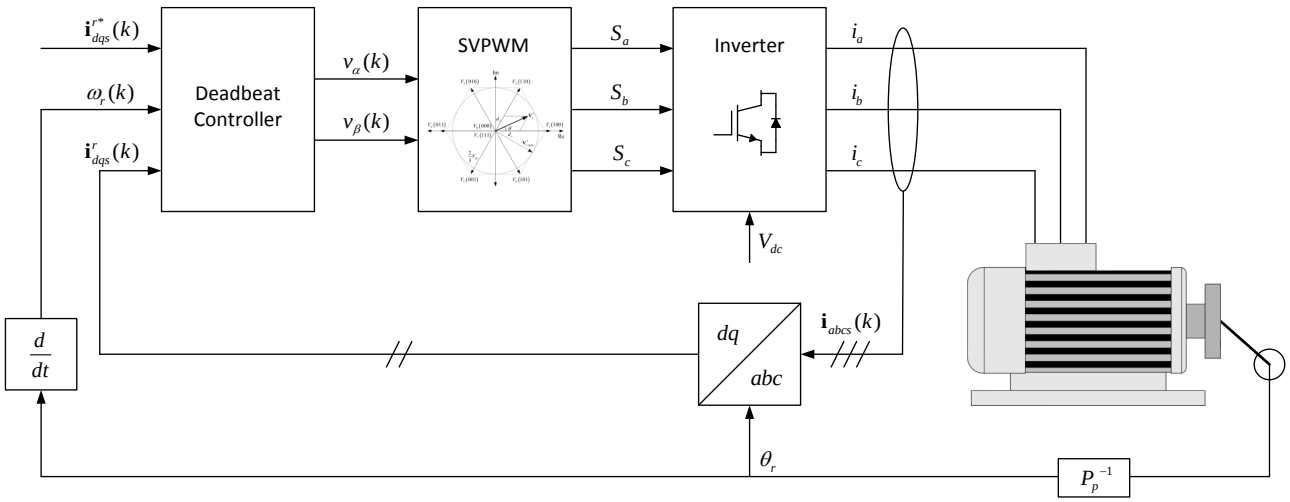

Master's Thesis
Power Electronics and Drives
Department of Energy Technology
Aalborg University, Denmark

Group PED4-1043
Jesper Moos

03/06/2014

AALBORG UNIVERSITY
STUDENT REPORT

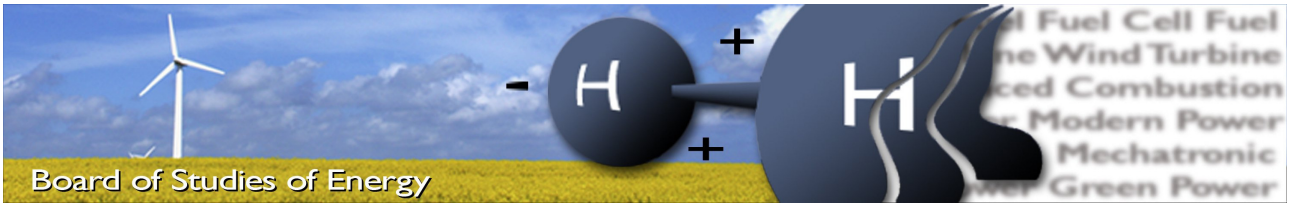

Title:	Predictive Deadbeat Control For PMSM Drive
Semester:	4^{th} semester M.Sc., PED4
Semester theme:	Master's Thesis - Power Electronics and Drives
Project period:	03/02-2013 - 03/06-2013
ECTS:	30
Supervisor:	Kaiyuan Lu
Project group:	PED4-1043

SYNOPSIS:

This thesis focuses on the design, analysis, and implementation of a predictive deadbeat current controller for controlling a Permanent Magnet Synchronous Machine (PMSM) drive system. The deadbeat controller is compared to a classical FOC PI controller in order to understand performance improvements and problems introduced by this type of controller. Two simulation models are developed in order to verify the theory of the controllers. Given inverter dead-time and DSP delay are influential for the performance of the deadbeat controller, compensation is developed and implemented in the deadbeat controller model. Based on results obtained from the simulation models, both controllers are implemented in a dSPACE DS1103 laboratory setup. Finally, the controllers are tested for parameter sensitivity. As a result of this thesis, the predictive deadbeat controller is found to be a simple and intuitive controller, which offers outstanding dynamic performance that can compete with the performance of the classical FOC PI controller. Based on the analysis, the deadbeat controller is shown to exhibit small steady state errors compared to the FOC PI controller due to the model parameter dependency and non-linearities of the inverter.

Jesper Moos

Copies: 3
Pages, total: 104
Appendix: 3
Supplements: 1 CD

By signing this document, each member of the group confirms that all participated in the project work and thereby that all members are collectively liable for the content of the report.

Preface

This Master Thesis is written by Jesper Moos, a 10^{th} semester master student at the Department of Energy Technology, Aalborg University. The semester theme is Power Electronics and Drives.

Reading instructions

This thesis contains a nomenclature list in the beginning including symbols, descriptions and units. Furthermore, a list of abbreviations is included. The denotation employed for equations throughout the thesis is based on the general notation (X.Y) which suggest that the specific X^{th} equation belongs to the Y^{th} chapter. The same notation applies to figures and tables, which also have a short caption attached. The units found to the right of each equation and in general throughout the thesis, are SI units as described by The International System of Units.

At the end of the thesis, the bibliography is found. The references are denoted by [Surname, year] throughout the report. As an ending to the thesis the appendixes are found. The appendixes are included as a supplement such that the interested reader can gain further insight into the employed methods. As a further attachment to the thesis, a CD with all relevant digital information is included. It contains the Matlab and Simulink models, the used articles, experimental data, and a PDF version of the thesis.

Abstract

The development of fast and powerful microprocessors and Digital Signal Processors (DSPs), have over the last decade increased and extended the application of model predictive control for Power Electronics and Drives.

This thesis focuses on the design, analysis, and implementation of a predictive deadbeat current controller for controlling a Permanent Magnet Synchronous Machine (PMSM) drive system. In order to evaluate and compare the performance of the proposed deadbeat controller, a classical Field Oriented Control (FOC) PI current controller is also designed.

The basic theory of the drive system is presented, and mathematical models of the inverter and PMSM are developed. Two simulation models are developed; one based on the classical PI current controller, and another based on the deadbeat controller. Given inverter dead-time and DSP delay are influential for the performance of the deadbeat controller, compensation is also developed and implemented in the deadbeat controller model. Based on the results obtained from simulations, the controllers are implemented in a dSPACE 1103 laboratory setup. Finally, the controllers are tested for parameter sensitivity both in simulations and in the experimental setup.

Additionally, this thesis discusses how the inductance of the machine may be determined using the inverter zero voltage vector, and discussed how the core losses of the machine may be decreased, by weakening the magnetic field flux density.

As a result of this thesis, the predictive deadbeat controller is found to be a simple and intuitive controller, which offers outstanding dynamic performance that can compete with the performance of the classical FOC PI controller. The deadbeat controller is found to suffer from small steady state errors, possibly caused by its dependency on model parameters and inverter non-linearities which must be properly compensated for under different system operation points.

Table of Contents

List of Symbols

Symbol	Description	Units
$V_{ab,bc,ca}$	Phase a, b or c line-to-line voltage	[V]
V_{dc}	DC-link voltage	[V]
$V_{an,bn,cn}$	Phase a, b or c line-to-neutral voltage	[V]
$S_{a,b,c}$	Phase a, b or c switching state	[-]
$f^r_{ds,qs,0s}$	Rotor reference direct-, quadrature-, or zero sequence component	[-]
$f^r_{as,bs,cs}$	Phase a, b or c stationary component	[-]
θ_r	Electrical angular rotor position	[rad]
$v^r_{ds,qs}$	Direct,- or quadrature axis voltage	[V]
V_{0-7}	Inverter switching state	[-]
$\mathbf{V}^*$	Reference voltage vector	[-]
$\mathbf{V}_{x,y,z}$	Adjacent voltage vector	[-]
$d_{x,y,z}$	Duty cycle of adjacent voltage vectors	[-]
θ	Angular position of reference voltage vector	[rad]
n	Sector number	[-]
R_{ph}	Stator resistance	[Ω]
$i_{a,b,c}$	Phase a, b or c current	[A]
$\lambda_{a,b,c}$	Phase a, b or c flux linkage	[Wb]
$L_{asas,bsbs,cscs}$	Phase a, b or c self inductance	[H]
$M_{asbs,bscs,csas}$	Mutual inductance of phase a, b or c	[H]
λ_{pm}	Permanent magnet flux linkage	[Wb]
$f_{\alpha,\beta}$	Stationary α or β component	[-]
$\mathbf{f}^r_{dqs}$	Rotor reference vector sum	[-]
$i^r_{ds,qs}$	Rotor reference direct-, or quadrature axis current.	[A]
ω_r	Electrical angular rotor speed	[rad/s]
$L_{d,q}$	Direct-, or quadrature axis synchronous inductance	[H]
T_e	Electromagnetic torque	[Nm]
P_p	Pole pairs	[-]
B_m	Viscous damping coefficient	[Ns/m]
J_m	Drive shaft inertia	[kg·m^2]
J_0	Drive shaft Coulomb friction	[Nm]
ω_m	Mechanical angular rotor speed	[rad/s]
δ	Torque angle	[rad]
$\mathbf{i}_s$	Stator current vector	[A]
$\mathbf{v}_s$	Stator voltage vector	[V]
ϕ	Angle between stator voltage- and current vector	[rad]
k	Sampling number	[-]
s	Laplace operator	[-]
K_{pc}	Proportional gain current controller	[-]
K_{ic}	Integral gain current controller	[-]
T_d	System time delay	[s]
G_{ol}	Open loop transfer function	[-]
G_{cl}	Closed loop transfer function	[-]
ω_n	Natural frequency	[rad/s]
ζ	Damping ratio	[-]
$\%OS$	Percent overshoot	[-]

Symbol	Description	Units
K_t	Torque constant	[Nm/A]
τ_q	Equivalent time constant	[s]
$K_{p\omega}$	Proportional gain speed controller	[-]
$K_{i\omega}$	Integral gain speed controller	[-]
$K_{a\omega}$	Anti-windup gain	[-]
n	System order	[-]
T_s	Sampling period	[s]
$\mathbf{i}^r_{dqs}$	Rotor reference current vector	[A]
$\hat{\mathbf{i}}^r_{dqs}$	Predicted rotor reference current vector	[A]
$\hat{i}^r_{dqs}$	Predicted direct- or quadrature axis current	[A]
t_d	Inverter dead-time	[s]
t_r	Rise time of IGBT	[s]
t_f	Fall time of IGBT	[s]
t_{off}	Off time of IGBT	[s]
V_{sw}	Transistor conduction voltage drop	[V]
V_d	Diode conduction voltage drop	[V]
ΔV	Average inverter voltage drop	[V]
$T_{amb,ref}$	Ambient and reference temperature	[°C]
$\epsilon i^r_{ds,qs}$	Steady state error	[A]
$\Delta i^r_{ds,qs}$	Steady state current ripple	[A]
λ_m	Total machine flux linkages	[Wb]
P_{IM}	Induction machine power	[W]
P_{PMSM}	Permanent magnet synchronous machine power	[W]

Abbreviations

Acronym	Description
PMSM	Permanent Magnet Synchronous Machine
SMPMSM	Surface Mounted Permanent Magnet Synchronous Machine
DSP	Digital Signal Processor
AC	Alternating Current
DC	Direct Current
FOC	Field Oriented Control
PWM	Pulse Width Modulation
PI	Proportional-Integral
DPC	Direct Predictive Control
FDSL	Flexible Drive Systems Laboratory
VSI	Voltage Source Inverter
PPC	PowerPC
RISC	Reduced Instruction Set Computing
IGBT	Insulated Gate Bipolar Transistor
IM	Induction Machine
SVPWM	Space Vector Pulse Width Modulation
THD	Total Harmonic Distortion
PPC	Predictive Current Control
PM	Permanent Magnet
EMF	Electromotive Force
ADC	Analog-to-Digital Converter

Chapter 1
Introduction

1.1 Background

The recent decades remarkable advancement of semiconductor devices, and the development of cost effective and powerful DSPs and microprocessors have given numerous opportunities for many industrial applications. One of the by now well-known applications is within AC-machine drives.

Today, power electronics have increased efficiency and reliability. For that reason an increased attention is given to the development of high performance adjustable speed AC drives, as they can decrease the cost, and outdo the performance and efficiency of traditional DC adjustable speed drives. With today's focus on energy efficiency optimization, this is a major industrial mean, while also the increased scope of application for electrical machines sets advanced demands for the dynamic performance.

Permanent Magnet Synchronous Machine (PMSM) drives have been found to be advantageous over other drives, e.g. due to its high efficiency and high power density. For that reason PMSMs are intensively studied among researchers, scientists, and engineers and is considered a hot topic of study.

Presently, the most widespread control technique used to control the PMSM is the Field Oriented Control (FOC). FOC is a vector control technique that decomposes the stator currents into a magnetic field-generating part and a torque-generating part. This allows separate control of the machine flux and torque, similar to the control of a DC machine. By controlling the stator current amplitude and frequency, the speed- and torque level of the machine is controlled. The traditional FOC technique uses classical Proportional-Integral controllers in the rotating dq reference frame to control the stator currents. The output of the current controllers, produces the necessary voltages, which by Pulse Width Modulation (PWM) are synthesized by an inverter to the machine terminals. The proportional- and integral gains must be carefully chosen to insure proper dynamic performance, and are normally tuned based on classical control theory. [Krishnan, 2010]

New trends concerning improvement of the dynamic performance of the PMSM has caused development of high performance control techniques. Deadbeat control is one of the control techniques that has shown to improve the dynamic performance. [Rodriguez, 2012] [Morel et al., 2009]

1.2 Deadbeat Control

Deadbeat control is a control strategy found in the predictive control family. The idea behind predictive control is to use a model of the system to calculate predictions of future controlled variables. Deadbeat control is a discrete-time model based control scheme, which uses the machine model to calculate the voltages that eliminate the current errors after one sampling period. The voltages are subsequently synthesized to the machine terminals using an inverter controlled by PWM.

The concept of deadbeat control is simple and intuitive compared to a PI controller based strategy, as parameter tuning is avoided. Deadbeat control uses a fixed inverter switching frequency as FOC. This permits designing an input filter for the PMSM opposite to for example Direct Predictive Control (DPC) which utilize a finite set of switching states with variable switching frequency. Moreover, the deadbeat control algorithm allows for incorporation of system constraints and other non-linearities, and finally it requires relatively low computation power compared to DPC.

When utilizing deadbeat control one can expect a fast transient response i.e. a high bandwidth, but as the deadbeat control strategy is based on a model of the system, it is sensitive to parameter errors, system delays, and inverter non-linearities as the manipulated variables are a direct product of the system model. For this cause, to increase the reliability and robustness, further development of the conventional deadbeat controller has been seen. [Rodriguez, 2012]

1.3 Literature Study

The literature on deadbeat control of the PMSM is reasonable, and several articles have presented excellent results based on deadbeat control. It is a general understanding through the studied literature that the stability and performance of the deadbeat control algorithm is poor under model parameter mismatches and system delays, hence effort is put into improving the stability under these conditions.

In [Moon et al., 2003] the authors have modified the conventional deadbeat controller and built-in system delay compensation, which was shown to increase the dynamic performance significantly avoiding torque oscillations caused by the system delay. In [Springob and Holtz, 1998] the authors have gone even further and improved the system delay compensation technique in form of an improved current predictor which uses average system variables and incorporated a dead-time compensation technique to increase the steady state accuracy. Based on their results, it can be concluded that their work have improved the torque ripple significantly on the cost of increased computational power.

In [Wang et al., 2011] the authors have improved the performance of the conventional deadbeat algorithm under inductance parameter mismatch. Their results show that, using a method based on relaxing the deadbeat constraint, the system stability under inductance parameter mismatch was improved with up to 53 %. [Li et al., 2012] have similarly presented a method to compensate for inductance parameter mismatch in the deadbeat algorithm. They have adapted a robust current control algorithm with two weighting factors, which is based on zero direct axis current control. Their results show a decreased ripple current under increased model stator inductance, which is beneficial.

1.4 Objective

The objective of this project is to design and implement a high performance deadbeat control strategy as a replacement of the classical PI current controllers found in FOC. This is done both in simulations and in an experimental setup in order to map out the performance and understand the possible improvements and problems compared to the classical PI controller. This includes modeling and implementing both a classical FOC- and a deadbeat control strategy.

As the electromagnetic torque is a product of the stator currents, these must be controlled with high accuracy and a minimum transient in order to improve the torque and thereby the system performance. Therefore, it is pursued to mitigate the system delay effects and inverter non-linearities as these effects distort the torque performance. Also the system hardware limitations must be respected at all times.

A further objective is to investigate possible improvements of the algorithm which could eventually result in an increased industrial interest.

1.5 Problem Statement

To improve the dynamic performance of a drive system of which the PMSM forms part of, a deadbeat current control strategy is a possible candidate. The results must be compared to existing control strategies to understand the improvements. The accuracy with this strategy is known to decrease with parameter errors, hence it could be beneficial to map out the performance under such case, and introduce algorithm modification that can account for such. Finally, based on acquired knowledge an

energy optimization of the drive system could have industrial interest. Specifically, this project will answer the following questions:

- How is the deadbeat current control applied to replace the PI current control in the traditional FOC strategy?
- What kind of performance improvements can the deadbeat control offer compared to PI control?
- How can the conventional deadbeat controller be improved?
- What kind of performance can be expected by deadbeat control under model parameter error?
- How can system parameter variation be incorporated into the deadbeat algorithm?
- How can the electrical losses of the PMSM be minimized?

1.6 Thesis Outline

This thesis is mainly organized as follows: First, an overview of the system will be presented in Chapter 2. This includes modeling of the two-level voltage source inverter, its modulation strategy, and the PMSM electrical- and mechanical model. Second, the classical FOC theory is presented and its controller parameters are theoretically tuned, followed by an adjustment according to experimental results. Third, the deadbeat current controller theory, together with a delay compensation method, an inverter dead-time compensation method, and several other important considerations are presented. Fourth, the simulation and experimental results of both control strategies are presented in Chapter 5 and 6. Fifth, both the performance of the PI control and deadbeat control are tested for parameter errors in order to point out what sort of problems may occur under these conditions. Moreover, Chapter 8 considers the effects of machine iron saturation which causes the inductance to change and presents a method to identify the inductance variation. Also it considers a method to decrease the occupied electrical power of the PMSM, causing the efficiency to increase. The overall results, discoveries, and considerations are at last discussed, and then advantages and disadvantages are pointed out in a final conclusion which also consider possible directions of future work.

1.7 Limitations and Assumptions

Under the preparation of this thesis several limitations and assumptions are made. Since the primary objective of the project is to design, analyse, and implement the high performance deadbeat controller, and not directly dedicated to improve the deadbeat control known from the literature, the focus was laid on design, implementation, and mapping and evaluation of the experimental performance. Therefore, and because of time constraint, the latter part has been given minor attention. A thorough study on experimental performance using stator inductance compensation and power loss minimization is therefore suggested.

The assumptions made in the simulations can be listed as shown below:

PMSM model:
The PMSM is assumed properly described by the *dq* model presented. By using this model formulation the following assumptions are made:

- The supply voltages are symmetrically balanced.
- The machine stator windings produce sinusoidal MMF distribution in the air-gap.
- The synchronous inductances contains a DC component and a sinusoidally varying component.
- Magnetic saturation is neglected.
- Core losses are neglected.
- Constant stator resistance, e.g. temperature changes are not modeled.
- The mechanical system is modeled as an one mass system, hence any elasticity in the coupling is neglected.

Inverter model:
The two-level voltage source inverter is assumed ideal e.g. without losses in transistors and diodes, hence the only modeled non-linearity is the dead-time.

- The modeled dead-time is 2.5 μs as in the experimental setup.
- The switching frequency is 5 kHz.

The assumptions made in the experimental work can be listed as shown below:

- The waveforms obtained using the dSPACE system are assumed to be valid. This assumption was verified using an oscilloscope, since the frequencies of interest are lower than the utilized sampling frequency of 5 kHz.
- The delays introduced by the dSPACE system are equal to approx. 2 sampling periods.
- The measurement devices are assumed calibrated and their measurements are trusted.

Chapter 2
System Description

In this chapter the drive system is presented, starting with a description of the dSPACE test setup. A list of technical data for the test setup is then presented. Next, an inverter model is developed and its space vector modulation strategy is explained. Finally, the PMSM electrical- and mechanical models are presented, all with the purpose of designing a simulation model of the test setup.

2.1 System Configuration

The test setup of which this project is based, is a dSPACE DS1103 system found in the Flexible Drive Systems Laboratory (FDSL). Figure 2.1 presents the practical test setup and Figure 2.2 the technical configuration of the system.

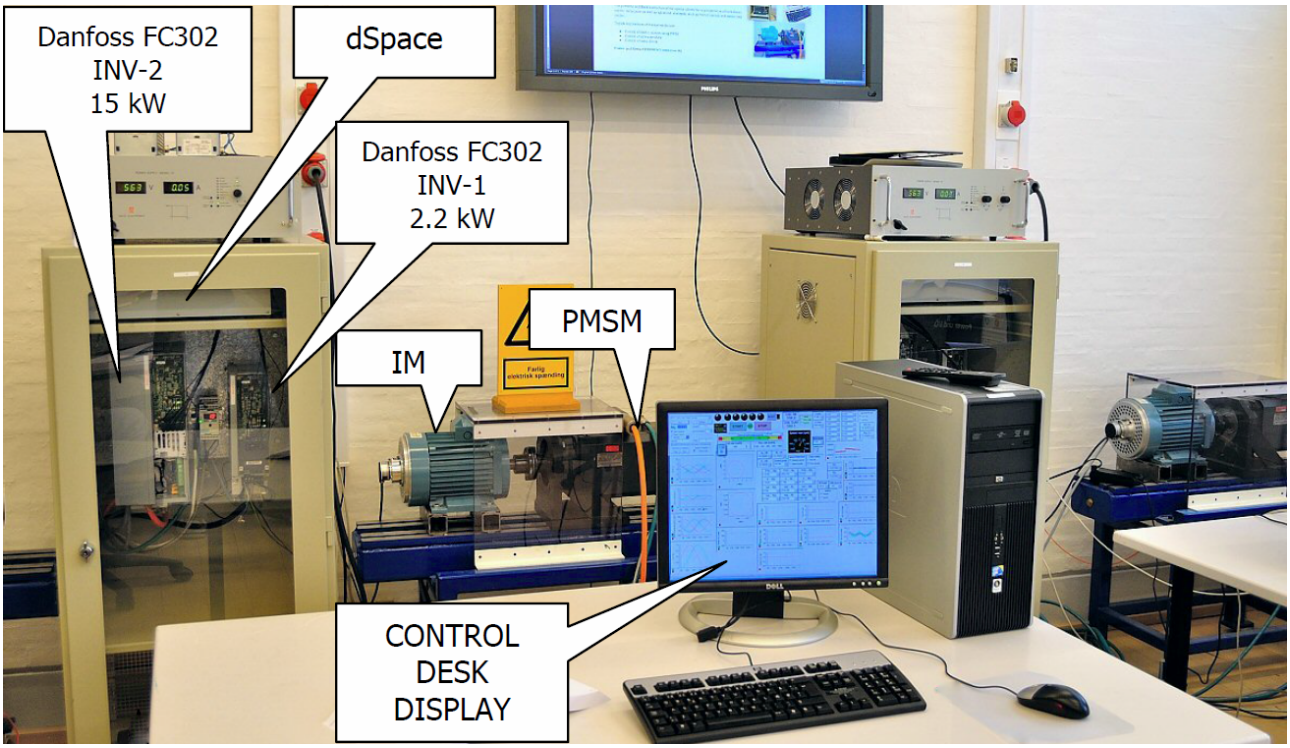

Figure 2.1. The practical dSPACE test setup found in the Flexible Drive Systems Laboratory.

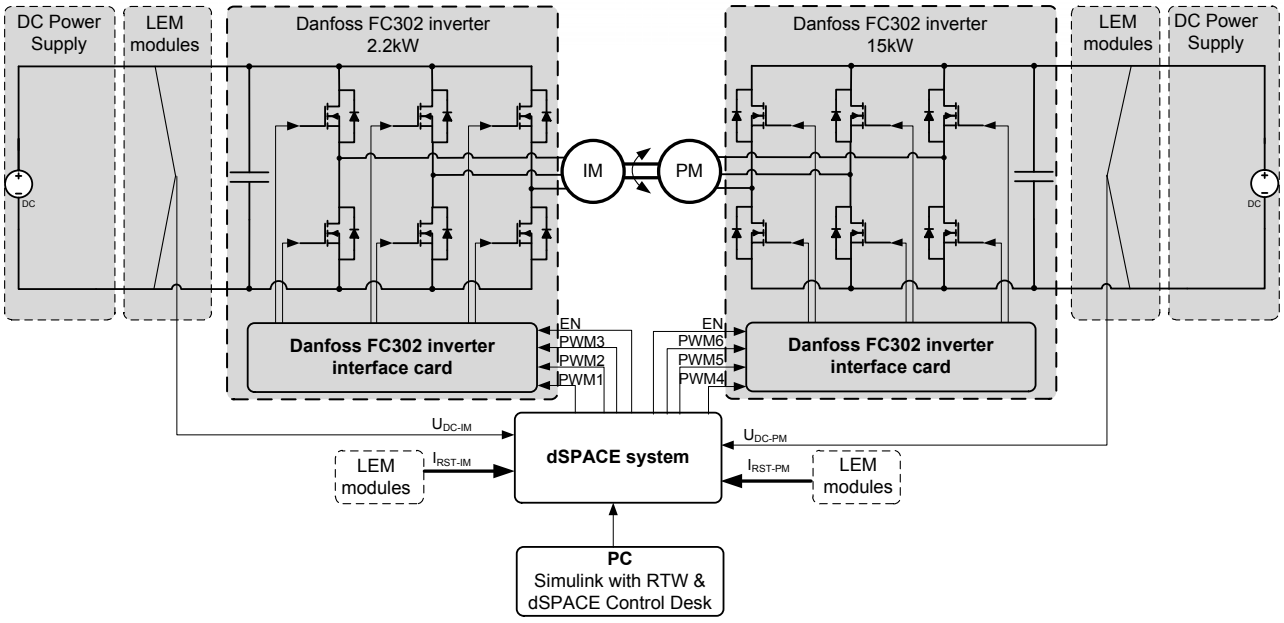

Figure 2.2. The technical configuration of the dSPACE test setup.

As shown in Figure 2.1 and Figure 2.2 the setup consists of two AC machines that are operated by two Danfoss FC302 Voltage Source Inverters (VSI). Both inverters are controlled by the dSPACE DS1103 PPC system, which is programmed and operated using Simulink and dSPACE Control Desk.

The dSPACE DS1103 PPC is a mixed RISC/DSP digital controller providing a powerful processor for floating point calculations as well as comprehensive I/O capabilities. It features a software Simulink interface that allows all applications to be developed in the MATLAB/Simulink environment. DSP code compiling and downloading are carried out automatically in the software environment, meaning that the Simulink models are compiled into useable C-code. To increase the computational speed, the environment allows one to use s-functions, which are more properly converted into c-code. An experimental software called dSPACE Control Desk, allows real-time management of the running process by providing a virtual control panel with instruments and scopes.

The Danfoss 2-level FC302 VSI 15 kW operating the PMSM is DC supplied by a Siemens SIMOVERT RRU regenerative line rectifier. The specifications of the VSI are listed in Table 2.1. Using a VSI can cause terminal voltage errors due to several non-linearities found inside the VSI. These include inverter dead-time to avoid shoot through faults, IGBT voltage drop and turn on/off time. The latter two factors are frequency and current-level dependent.

The test setup system parameters are obtained from a laboratory test procedure shown in Appendix A and directly from the manufacturer specifications. Since the IM is used simply as a mechanical load for the PMSM, the specifications are not presented here. The complete system specifications are presented in Table 2.1.

Table 2.1. Technical data of the test setup, obtained partly from the test procedure in Appendix A.

Siemens PMSM ROTEC 1FT6084-8SH7		
Rated speed	n_n	4500 $\mathtt{min^{-1}}$
Pole pairs	p_p	4
Rated torque	M_n	20 Nm
Rated current	I_n	24.5 A
Rated power	P_n	9.42 kW
Torque constant	k_T	1.01 Nm/A
Winding resistance	R_{ph}	0.19 Ω*
Field inductance	L	2.2 mH*
Magnetic flux	λ_{pm}	0.12256 Wb*
Danfoss FC302 VSI 15 kW		
Rated input voltage	V_{in}	380-500 V
Rated output voltage	V_{out}	0-500 V
Rated input current	I_{in}	29 A
Rated output current	I_{out}	32 A
Dead-time	t_{dead}	2.5 μs
Output voltage frequency	f_{out}	0-1000 Hz
Utilized switching frequency	f_{sw}	5 kHz
Mechanical system		
Drive shaft inertia	J_m	0.0146 $\mathtt{kg{\cdot}m^2}$*
Viscous damping	B_m	0.00167 Ns/m*
Coulomb friction	J_0	0.2295 Nm*
dSPACE DS1103 PPC		
Sampling frequency	f_s	5 kHz

*obtained from laboratory test.

2.2 Voltage Source Inverter

The Danfoss FC302 2-level VSI is a full bridge power electronic device that is formed by 6 IGBTs positioned in three legs. The mathematical formulation of the VSI presented in this section do not consider dead-time and other non-linearities, i.e. the otherwise non-linear IGBTs are considered as ideal switches. The non-linearities are easily modelled using Simulink. The topology of a 2-level VSI is shown in Figure 2.3.

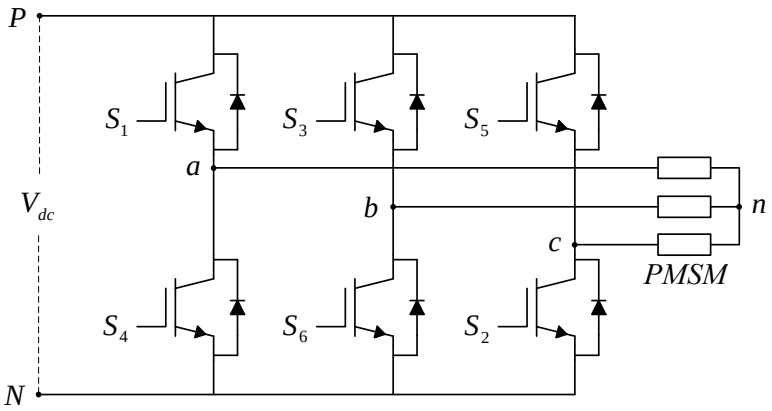

Figure 2.3. A full bridge 2-level Voltage Source Inverter (VSI) with IGBT switches.

By considering that each leg has two switches that each either can be ON or OFF depending on the applied gate signals S_x, several scenarios are available. To avoid DC voltage short circuits, the switches of each leg are always controlled with opposite gate signals. This demand results in 8 possible switching states, where two of them result in zero voltages. The terminal line-to-line voltages can from Figure 2.3 be described as in (2.1)

$$\begin{bmatrix} v_{ab} \\ v_{bc} \\ v_{ca} \end{bmatrix} = V_{dc} \begin{bmatrix} 1 & -1 & 0 \\ 0 & 1 & -1 \\ -1 & 0 & 1 \end{bmatrix} \begin{bmatrix} S_a \\ S_b \\ S_c \end{bmatrix} \quad [\mathtt{V}] \tag{2.1}$$

where $\mathbf{S}$ is the switching state vector representing the switching states of the three legs. By connecting the symmetrically wye-balanced PMSM, the line-to-neutral voltages can be described as shown in (2.2) using Kirchhoffs laws.

$$\begin{bmatrix} v_{an} \\ v_{bn} \\ v_{cn} \end{bmatrix} = \frac{V_{dc}}{3} \begin{bmatrix} 2 & -1 & -1 \\ -1 & 2 & -1 \\ -1 & -1 & 2 \end{bmatrix} \begin{bmatrix} S_a \\ S_b \\ S_c \end{bmatrix} \quad [\mathtt{V}] \tag{2.2}$$

Since the electrical model of the PMSM will be formulated in the rotor fixed dq reference frame, it is convenient to formulate the line-to-neutral voltages in that reference frame. To transform the stationary three phase variables into the rotor fixed dq reference frame, the transformation procedure in (2.3) is used.

$$\begin{bmatrix} f^r_{ds} \\ f^r_{qs} \\ f^r_{0s} \end{bmatrix} = \frac{2}{3} \begin{bmatrix} \cos(\theta_r) & \cos(\theta_r - \frac{2\pi}{3}) & \cos(\theta_r + \frac{2\pi}{3}) \\ -\sin(\theta_r) & -\sin(\theta_r - \frac{2\pi}{3}) & -\sin(\theta_r + \frac{2\pi}{3}) \\ \frac{1}{2} & \frac{1}{2} & \frac{1}{2} \end{bmatrix} \begin{bmatrix} f_{as} \\ f_{bs} \\ f_{cs} \end{bmatrix} \quad [-] \tag{2.3}$$

The transformation matrix decomposes by trigonometric relations the three phase variables into a complex vector that rotates around the origin at a speed equal to the electrical speed of the PMSM. By assuming symmetric voltages the zero component is zero and the rotor reference frame dq inverter voltages are described as in (2.4).

$$\begin{bmatrix} v^r_{ds} \\ v^r_{qs} \end{bmatrix} = \frac{2V_{dc}}{3} \begin{bmatrix} \cos(\theta_r) & \cos(\theta_r - \frac{2\pi}{3}) & \cos(\theta_r + \frac{2\pi}{3}) \\ -\sin(\theta_r) & -\sin(\theta_r - \frac{2\pi}{3}) & -\sin(\theta_r + \frac{2\pi}{3}) \end{bmatrix} \begin{bmatrix} S_a \\ S_b \\ S_c \end{bmatrix} \quad [-] \tag{2.4}$$

2.2.1 Modulation Strategy

In order to supply the necessary amplitude and frequency of the voltage demanded by the PMSM controller, the inverter switches must be controlled. There exist several Pulse Width Modulation (PWM) techniques, that allows one to control the voltages. The method applied in this thesis is the Space Vector PWM (SVPWM) technique which has a better DC-link utilization, a lower harmonic content, and facilitates the digital implementation compared to traditional Carrier Based sinusoidal PWM (CB SPWM). [Kazmierkowski et al., 2002]

Space Vector Modulation

A three-phase, two-level converter provides eight possible switching states (i.e. $2^3 = 8$), made up of six active and two zero switching states. Space vector modulation is based on space vector representation of the desired ac side reference voltages which is a spatial vector sum of the three-phase voltages. The six active vectors divide the space vector plane into six sectors each spanning 60 degrees. The desired reference voltage $\mathbf{v}^*_s$ is obtained by switching the two adjacent vectors and the two zero vectors for the proper time in each sector. By using this switching approach it is possible during each sampling to synthesize the desired reference voltage vector. The inverter space vector plane is shown in Figure 2.4.

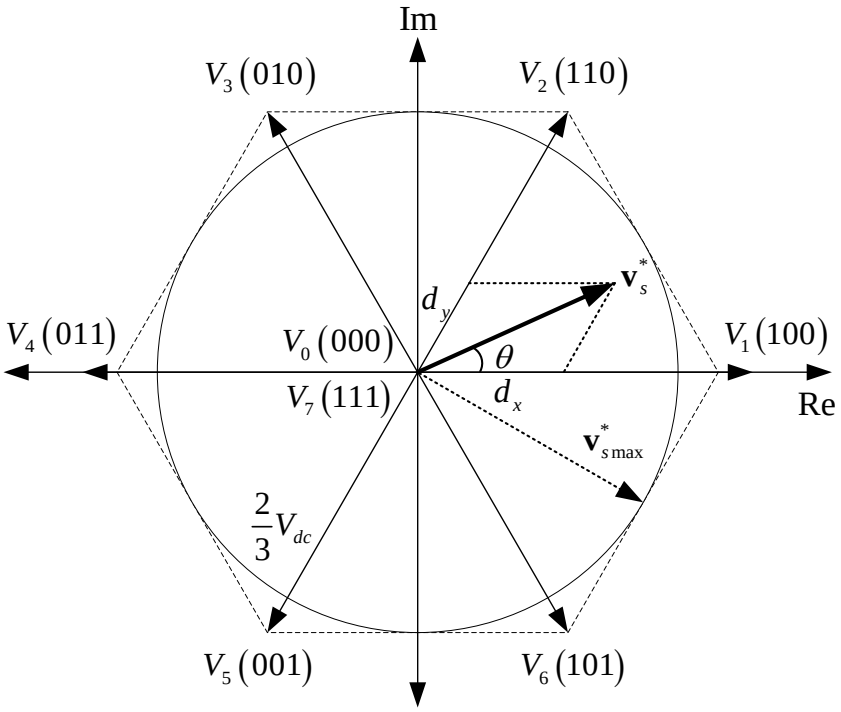

Figure 2.4. Space vector representation of the two-level inverter.

As seen from Figure 2.4 the zero vectors are located in the center of the hexagon as they produce no voltages. The maximum line-to-neutral voltage that can be applied by the inverter is $2/3V_{dc}$, and the allowable voltage amplitude $|\mathbf{v}_s^*| = \mathbf{v}_{s\,max}^*$ that can be commanded by the controller is $V_{dc}/\sqrt{3}$ which corresponds to the radius of the inner circle of the hexagon or 86.6% of the maximum available line-to-neutral voltage. Higher voltage amplitudes (up to $2/3V_{dc}$) can be obtained by an additional non-linear overmodulation algorithm. [Kazmierkowski et al., 2002]

Considering that the only possibility using the inverter to synthesize the desired reference voltage is to take the time average value of the adjacent voltage vectors together with the zero vectors, the reference voltage can be described as in (2.5)

$$\mathbf{v}_s^* = d_x\mathbf{V}_x + d_y\mathbf{V}_y + d_z\mathbf{0} \quad [-] \tag{2.5}$$

$$|\mathbf{v}_s{}^*| \begin{bmatrix} \cos(\theta) \\ \sin(\theta) \end{bmatrix} = d_x\frac{2}{3}V_{dc}\begin{bmatrix} 1 \\ 0 \end{bmatrix} + d_y\frac{2}{3}V_{dc}\begin{bmatrix} \cos(\frac{\pi}{3}) \\ \sin(\frac{\pi}{3}) \end{bmatrix} + d_z\mathbf{0}$$

where during one sampling period the duty cycles must satisfy (2.6),

$$d_x + d_y + d_z = 1 \quad [-] \tag{2.6}$$

where:
d_x percentage of sample time period where $\mathbf{V}_x$ is applied
d_y percentage of sample time period where $\mathbf{V}_y$ is applied
d_z residual percentage of sample time period where $\mathbf{V}_0$ and $\mathbf{V}_7$ are applied
θ is the voltage vector argument

By using simple trigonometrical relationships present in Figure 2.4 which is based on the line-to-neutral voltages, the duty cycles for the adjacent active voltage vectors (d_x, d_y) and the zero voltage vector(s) (d_z) can be calculated.

Once the sampled reference voltage vector argument ($\arg(\mathbf{v}_s^*) = \theta$) and absolute value ($|\mathbf{v}_s^*|$) are calculated, these are used to determine the duty cycles according to (2.7), (2.8), and (2.9).

$$d_x = \frac{|\mathbf{v}_s^*|\sqrt{3}}{V_{dc}} \sin\left(\frac{n}{3}\pi - \theta\right) \quad [-] \tag{2.7}$$

$$d_y = \frac{|\mathbf{v}_s^*|\sqrt{3}}{V_{dc}} \sin\left(\theta - \frac{n-1}{3}\pi\right) \quad [-] \tag{2.8}$$

$$d_z = 1 - d_x - d_y \quad [-] \tag{2.9}$$

In SVPWM, the duty cycles are uniquely determined using the general formulation in (2.7), (2.8), and (2.9) which accounts for the trigonometric relations that exists in each sector (n). The only variations that are utilized are the choice of the zero vector(s), and the sequence in which the active voltage vectors are applied within the switching cycle. The switching sequence applied in this project is the symmetric 7-segment switching sequence, as shown in Figure 2.5, which has been shown in previous work to have the lowest Total Harmonic Distortion (THD). [Krishnan, 2010]

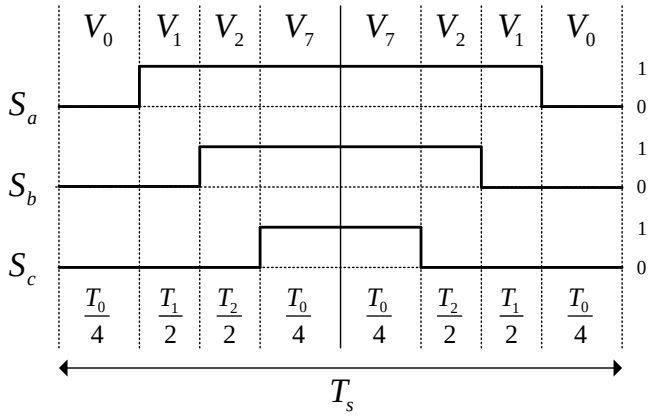

Figure 2.5. Phase gate signals for sector 1 in SVPWM when using symmetric placement of zero vectors.

2.3 Permanent Magnet Synchronous Machine

This section presents the rotor reference frame dq model of the PMSM. The Siemens PMSM ROTEC 1FT6084-8SH7 is modelled by three model components - a stator voltage equation, a flux linkage equation and a mechanical system equation. The stationary stator voltage equation used to describe any three phase electrical machine as shown in (2.10) consists of a resistive part plus the time rate of change of the flux linkage.

$$\begin{bmatrix} v_{an} \\ v_{bn} \\ v_{cn} \end{bmatrix} = \begin{bmatrix} R_{ph} & 0 & 0 \\ 0 & R_{ph} & 0 \\ 0 & 0 & R_{ph} \end{bmatrix} \begin{bmatrix} i_a \\ i_b \\ i_c \end{bmatrix} + \frac{d}{dt} \begin{bmatrix} \lambda_a(\theta_r) \\ \lambda_b(\theta_r) \\ \lambda_c(\theta_r) \end{bmatrix} \quad [\mathtt{V}] \tag{2.10}$$

The stationary flux linkage equation for the PMSM as shown in (2.11), consists of self- and mutual inductances and the permanent magnet rotor flux linkage.

$$\begin{bmatrix} \lambda_a(\theta_r) \\ \lambda_b(\theta_r) \\ \lambda_c(\theta_r) \end{bmatrix} = \begin{bmatrix} L_{asasm} & M_{asbsm} & M_{ascsm} \\ M_{asbsm} & L_{bsbsm} & M_{bscsm} \\ M_{ascsm} & M_{bscsm} & L_{cscsm} \end{bmatrix} \begin{bmatrix} i_a \\ i_b \\ i_c \end{bmatrix} + \lambda_{pm} \begin{bmatrix} \cos(\theta_r) \\ \cos(\theta_r - \frac{2\pi}{3}) \\ \cos(\theta_r + \frac{2\pi}{3}) \end{bmatrix} \quad [\mathtt{Wb}] \tag{2.11}$$

As can be observed from (2.10) and (2.11), the model complexity is noticeable since the flux linkage equation is dependent on the rotor position. By applying reference frame transformation using the rotor position, the complexity is reduced and a simplified rotor reference frame dq model of the

PMSM can be formulated. Utilizing the transformation procedure of (2.3) transforms the three phase stationary voltage equation into a rotor reference frame *dq* model. In Figure 2.6 the principle of the transformation procedure is shown.

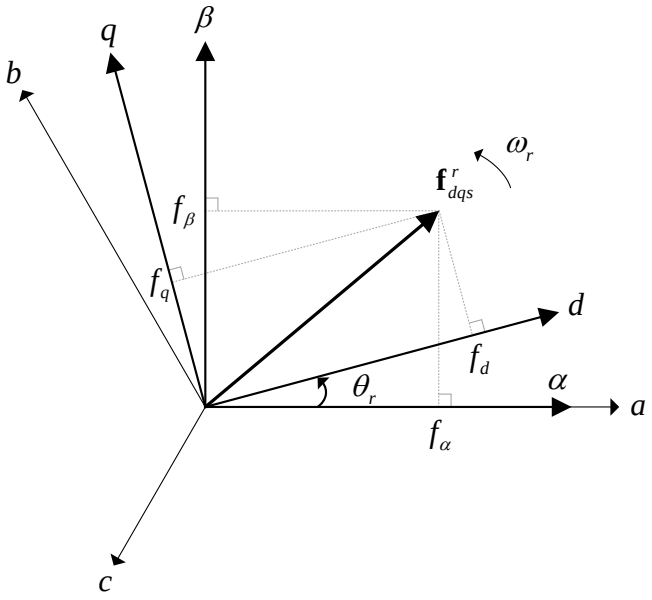

Figure 2.6. Principle of the machine model *dq* reference frame transformation.

Figure 2.6 illustrates a rotating vector. The vector is the sum of the three phase instantaneous quantities which is the outcome of the trigonometric relations in (2.3). The reference frame transformation hence creates a rotating vector which use the position of the rotor magnetic flux axis, and the instantaneous stator variables to create the *d*- and *q*-axis components. By aligning the *dq* reference frame with the rotor magnetic magnetic flux axis i.e. the *d*-axis, the inductance terms will become constants, hence simplifying the stator voltage equation. Thus using this transformation, sinusoidal *abc* variables are converted into *dq* constants in steady state. The outcome of the transformation for the stator voltage equation is shown in (2.12) and (2.13)

$$v^r_{ds} = R_{ph} i^r_{ds} - \omega_r L_q i^r_{qs} + L_d \frac{d}{dt} i^r_{ds} \quad [\mathtt{V}] \tag{2.12}$$

$$v^r_{qs} = R_{ph} i^r_{qs} + \omega_r (L_d i^r_{ds} + \lambda_{pm}) + L_q \frac{d}{dt} i^r_{qs} \quad [\mathtt{V}] \tag{2.13}$$

where:
$\omega_r = \frac{d}{dt}\theta_r$ is the electrical rotor speed
$L_{d,q}$ are the *d*- and *q*-axis inductances
$i^r_{ds,qs}$ are the *d*- and *q*-axis currents
$v^r_{ds,qs}$ are the *d*- *q*-axis voltages
λ_{pm} is the rotor permanent magnet flux linkage

The electromagnetic torque produced by the PMSM can be derived based on power considerations, and is shown in (2.14).

$$T_e = \frac{3}{2} p_p \left[\lambda_{pm} + (L_d - L_q) i^r_{ds}\right] i^r_{qs} \quad [\mathtt{Nm}] \tag{2.14}$$

where:
p_p is the magnetic pole pairs of the PMSM

Fundamentally, there exists two types of PMSMs, one where the permanent magnets are mounted

internally, and one where the magnets are mounted on the rotor surface. Depending on the type, the d- and q-axis inductances vary. The Siemens PMSM ROTEC 1FT6084-8SH7 has surface mounted magnets, hence the d- and q-axis inductances are equal, $L = L_d = L_q$. This allow controlling the electromagnetic torque solely by controlling the i^r_{qs} current as shown in (2.14).

The mechanical system of which the PMSM forms part of, is described by (2.15)

$$T_e = T_l + B_m\omega_m + J_0 + J_m\frac{d}{dt}\omega_m \quad [\mathtt{Nm}] \tag{2.15}$$

where:
T_l is the load torque
B_m is the drive system viscous damping coefficient
ω_m is the mechanical rotor speed
J_0 is the drive system Coulomb friction
J_m is the drive system inertia coefficient

Together, (2.12), (2.13), (2.14), and (2.15) constitute the complete continuous time rotor reference frame dq machine model and mechanical system of the drive system. The parameters in the model are determined according to the procedure shown in Appendix A.

Chapter 3
Field Oriented Control

In this chapter the Field Oriented Control (FOC) theory is presented. It is presented to form basis for designing the classical FOC of the PMSM. The PI current controller design is then carried out, followed by the design of the speed loop controller, which produces the reference for the q-axis PI current controller. Several design requirements are listed, and the anti-windup technique is also presented, such that system limitations can be kept at all times.

The classical FOC will serve as a reference for comparison to the deadbeat controller performance which is developed in the following chapter.

3.1 Vector Control

Vector control or Field Oriented Control (FOC) is a well known technique used to control the torque and speed of a PMSM. FOC has been developed on the basis of DC drives that allow decoupled control over the electrical torque and the magnitude of the rotor flux through its stator-excitation inputs. Many variations of vector control for the PMSM are available, including e.g. unity power-factor control or flux-weakening control. The method applied in this chapter is the constant torque-angle control or zero direct axis current control.

By aligning the stator variables with the rotor flux, using a reference frame transformation, vector control can be utilized. The reference frame transformation is accomplished using trigonometric relations which uses the position of the rotor flux axis, and the instantaneous stator variables to create a rotating complex vector which can be decomposed into d- and q-axis components. As input, the stationary stator currents in (3.1) are considered for vector control,

$$\begin{bmatrix} i_{as} \\ i_{bs} \\ i_{cs} \end{bmatrix} = i_s \begin{bmatrix} \cos(\theta_r + \delta) \\ \cos(\theta_r + \delta - \frac{2\pi}{3}) \\ \cos(\theta_r + \delta + \frac{2\pi}{3}) \end{bmatrix} \quad [\mathtt{A}] \tag{3.1}$$

where θ_r is the electrical rotor position, and δ the angle between the stator current vector and the rotor permanent magnet flux direction. The angle δ is also know as the torque angle, since depending on this angle the torque can be controlled. Transforming the three phase currents into d- and q-axis components using the transformation procedure in (2.3) produce the stator currents in rotor reference frame coordinates as shown in (3.2).

$$\begin{bmatrix} i^r_{ds} \\ i^r_{qs} \end{bmatrix} = i_s \begin{bmatrix} \cos(\delta) \\ \sin(\delta) \end{bmatrix} \quad [\mathtt{A}] \tag{3.2}$$

As seen from (3.2) the d- and q-axis currents are assumed constants since δ is constant for a given load torque. In Figure 3.1 the space vector diagram for an arbitrary torque angle is shown.

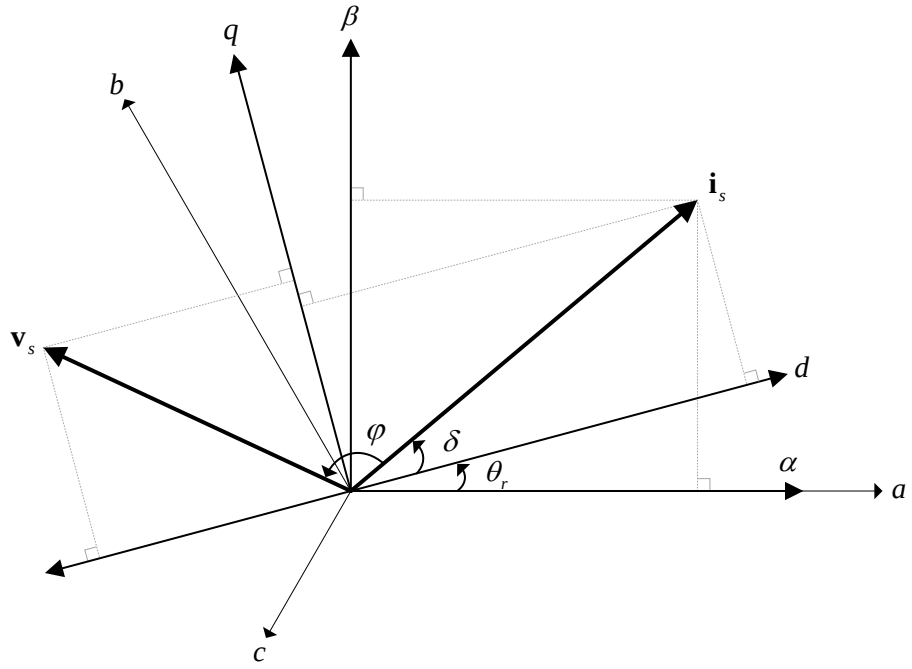

Figure 3.1. Space vector diagram of a two pole Permanent Magnet Synchronous Machine.

In Figure 3.1 the a, b, and c axes represents the direction of the stationary stator phase flux paths, and the d and q axes respectively the direction of the PM flux and the direction 90° ahead of the PM flux. Based on Figure 3.1 controlling the stator voltage vector $\mathbf{v}_s$ allows one to control the stator current vector $\mathbf{i}_s$, which by torque angle control allows control of the electrical torque. The stator current vector is composed of d and q axes components, which respectively can be thought of as the rotor flux producing component and the torque producing component.

At $\delta = 90°$ or solely q-axis current, maximum torque is produced since the interaction between the rotor flux and the stator flux is at its maximum, which is also mentioned in Section 2.3. This is referred to as the constant torque-angle control or zero direct axis current control. Flux weakening control is based on controlling also the d-axis current.

FOC is based on linear control of the non-linear inverter supplying the PMSM. Given a modulation stage for the inverter (which linearizes the inverter), any linear controller can be used with the inverter - the most common choice being Proportional-Integral (PI) controllers. The structure of FOC of a PMSM drive system is shown in Figure 3.2. The vector control type applied for this drive is the zero direct axis current control.

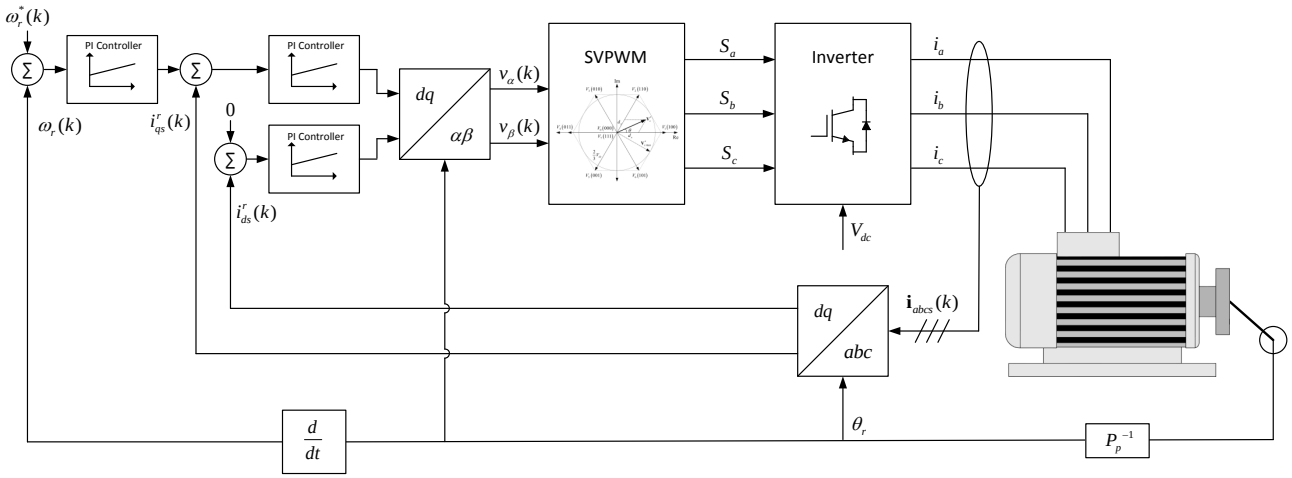

Figure 3.2. Sensored vector controlled PMSM drive utilizing the zero direct axis current control strategy. The outer loop controls the speed.

As Figure 3.2 shows, three PI controllers are utilized for controlling the speed of the PMSM. Two PI controllers controls the inner d- and q-axis current loops which translates the current errors into voltages in the rotor reference frame. The voltages are subsequently transformed into the stationary reference frame and the voltages are finally synthesized to the machine terminals using the SVPWM technique. The outer PI controller control the speed of the PMSM, hence the speed error translates into the necessary q-axis current level, which is the reference for the inner q-axis PI controller.

As the inner current loops dynamics are faster than the mechanical speed loop they can be tuned independently. The q-axis current loop and speed loop configuration is a cascade system which utilizes the advantages of cascade control that improves the dynamic performance and accounts for disturbances in the primary variable (load torque) faster.

3.2 Controller Requirements

Concerning the design of the classical FOC for the PMSM, certain requirements must be met to insure proper functionality. Therefore, a list of performance requirements are listed such that the FOC PI controllers can be designed with regards to these.

- The current loop overshoot should be 2-4% or lower.
- The rise time of the current loop should be lower than 10 sampling periods (2 `ms`).
- The rise time of the speed loop must be 4-10 times slower than the current loop in order not to cause problems due to insufficient control performance from the inner loop (6-20 `ms`).
- The speed loop must be able to suppress torque disturbances (load torque variations).
- The overshoot of the speed loop must be below 25%.
- Generally the system hardware limitations must be respected at all times.

These six requirements are used throughout the controller design procedures in the next two sections which respectively deal with the design of the current loop controllers and the speed loop controller.

3.3 Current Loop Controller Design

In order to design the current loop controllers, the system is analysed such that the dominant dynamics existing in the current loops are included. The control of the current loops, are derived based on the machine stator voltage equations (2.12) and (2.13). In order to obtain the desired currents, the transfer function between the d- and q-axis voltages, and d- and q-axis currents are required for design of the current loop controllers. The voltage equations are repeated in (3.3) and (3.4) using the Laplace variable.

$$v_{ds}^r(s) = (R_{ph} + sL_d)\, i_{ds}^r(s) - \omega_r L_q i_{qs}^r(s) \quad [\mathtt{V}] \tag{3.3}$$

$$v_{qs}^r(s) = (R_{ph} + sL_q)\, i_{qs}^r(s) - \omega_r \left(L_d i_{ds}^r(s) + \lambda_{pm}\right) \quad [\mathtt{V}] \tag{3.4}$$

The last terms to the right are known as the Back-EMF terms or the speed voltages. These terms makes the current loops dependent on each other, which is impractical concerning controller design. As both the electrical rotor speed and d- and q-axis currents are measured it is possible to eliminate these dependent terms. By adding into the current loops two blocks known in literature as the Back-EMF decoupling terms, these Back-EMF terms are excluded from the control loops. The Back-EMF decoupling terms are the original Back-EMF terms with opposite sign, hence the transfer functions for the d- and q-axis currents reduces to (3.5) and (3.6) which are two identical first order systems as the synchronous inductances are equal.

$$\frac{i_{ds}^r(s)}{v_{ds}^r(s)} = \frac{1}{sL_d + R_{ph}} \quad [\mathtt{A/V}] \tag{3.5}$$

$$\frac{i_{qs}^r(s)}{v_{qs}^r(s)} = \frac{1}{sL_q + R_{ph}} \quad [\mathtt{A/V}] \tag{3.6}$$

As the transfer functions are identical, only the design of the q-axis current loop is considered when designing the current PI controllers. By considering the transfer function in (3.6), it becomes obvious that the open loop is stable but requires a compensator to eliminate steady state error. Therefore the current loop block diagram can be constructed as shown in Figure 3.3 which includes the delays present in the system.

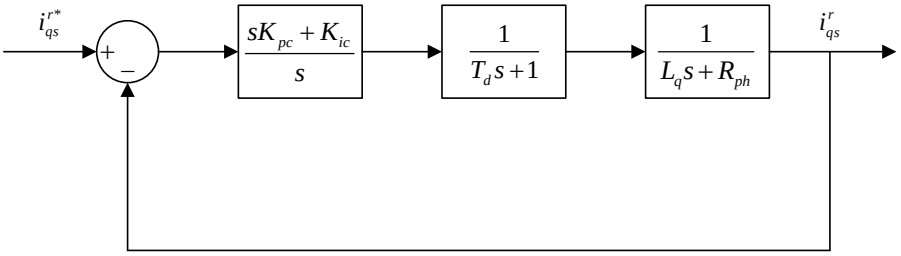

Figure 3.3. Block diagram of the q-axis current loop including the system delays.

The delay block is modelled as a first order time lag system, which simplifies the design of the continuous-time PI controller. The approximation of the time delay is considered adequate in practice for many drive system applications. [Krishnan, 2010]

By including the delay, the DSP and VSI delays in the actual setup are approximated hence the design of the PI controller becomes more realistic. Based on observation in the laboratory, the delay time equals two sampling periods $T_d = 0.4$ `ms`, which constitute of the inverter delay, the DSP calculation delay and analog-to-digital converter (ADC) delay. Considering the PI controller design the open loop transfer function can be formulated as shown in (3.7).

$$G_{ol}(s) = G_c(s) + G_d(s) + G_p(s) = \frac{K_{pc}s + K_{ic}}{s} + \frac{1}{1 + T_d s} + \frac{1}{R_{ph} + L_q s} \quad [\mathtt{A/V}] \tag{3.7}$$

The open loop transfer function is a third order system. By canceling the pole introduced by the electrical plant with the controller zero, the open-loop transfer function reduces to a second order system not dominated by the electrical pole. By setting the integrator gain equal to $K_{ic} = K_{pc}K_{ipc}$, and choosing $K_{ipc} = R_{ph}L_q^{-1}$, result in the open loop transfer function shown in (3.8).

$$G_{ol}(s) = \frac{K_{pc}}{L_q T_d} \frac{1}{s\left(s + \frac{1}{T_d}\right)} \quad [\mathtt{A/V}] \tag{3.8}$$

Based on the reduced open loop transfer function, the closed loop transfer function is derived as shown in (3.9) which resembles a general second order transfer function when $K = K_p(T_d L)^{-1}$.

$$G_{cl}(s) = \frac{G_{ol}(s)}{1 + G_{ol}(s)} = \frac{K}{s^2 + \frac{1}{T_d}s + K} = \frac{\omega_n^2}{s^2 + 2\omega_n\zeta s + \omega_n^2} \quad [\mathtt{A/V}] \tag{3.9}$$

Having the current loop formulated as a general second order transfer function, allows one to choose the remaining two parameters according to desired closed loop characteristics. The overshoot for a second order system is determined by the damping ratio ζ. By specifying the desired overshoot to 2% the required damping ratio can be calculated according to (3.10) which is based on the general underdamped second order transfer function.

$$\zeta = \frac{\ln\left(\frac{1}{\%\mathrm{OS}}\right)}{\sqrt{\ln\left(\frac{1}{\%\mathrm{OS}}\right)^2 + \pi^2}} \quad [-] \tag{3.10}$$

With the desired overshoot of 2% the damping ratio is calculated to $\zeta = 0.78$. Using this result, the proportional gain of the PI controller is calculated to $K_{pc} = 2.26$ by using (3.11).

$$K_{pc} = \frac{L_q}{T_d 4\zeta^2} \quad [-] \tag{3.11}$$

The integral gain of the PI controller is calculated to $K_{ic} = 195.33$ using (3.12).

$$K_{ic} = K_{pc} K_{ipc} \quad [-] \tag{3.12}$$

In Figure 3.4 the closed loop step response is shown.

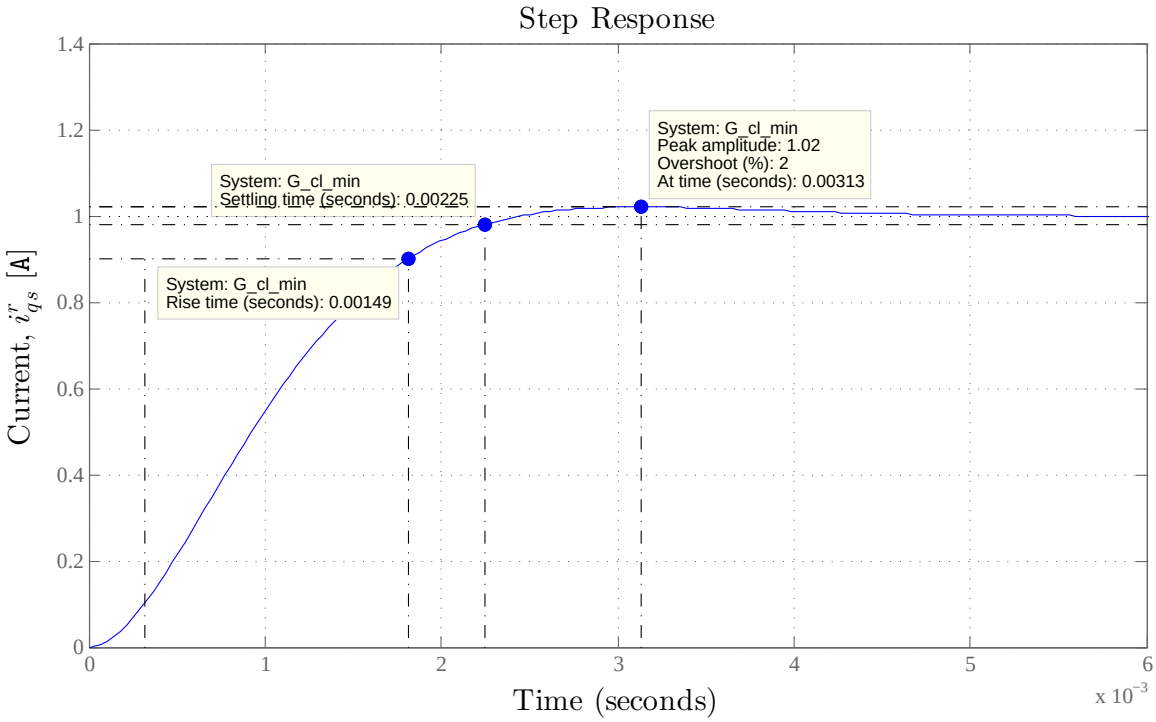

Figure 3.4. Current closed loop step response with inclusion of the system time delay.

It can be seen that the requirements for the current loop previously specified are kept as the overshoot is 2% and the rise time is within the requirement of ten sampling periods. Figure 3.5 presents the root locus plot which show the pole-zero cancellation of the dominant electrical pole.

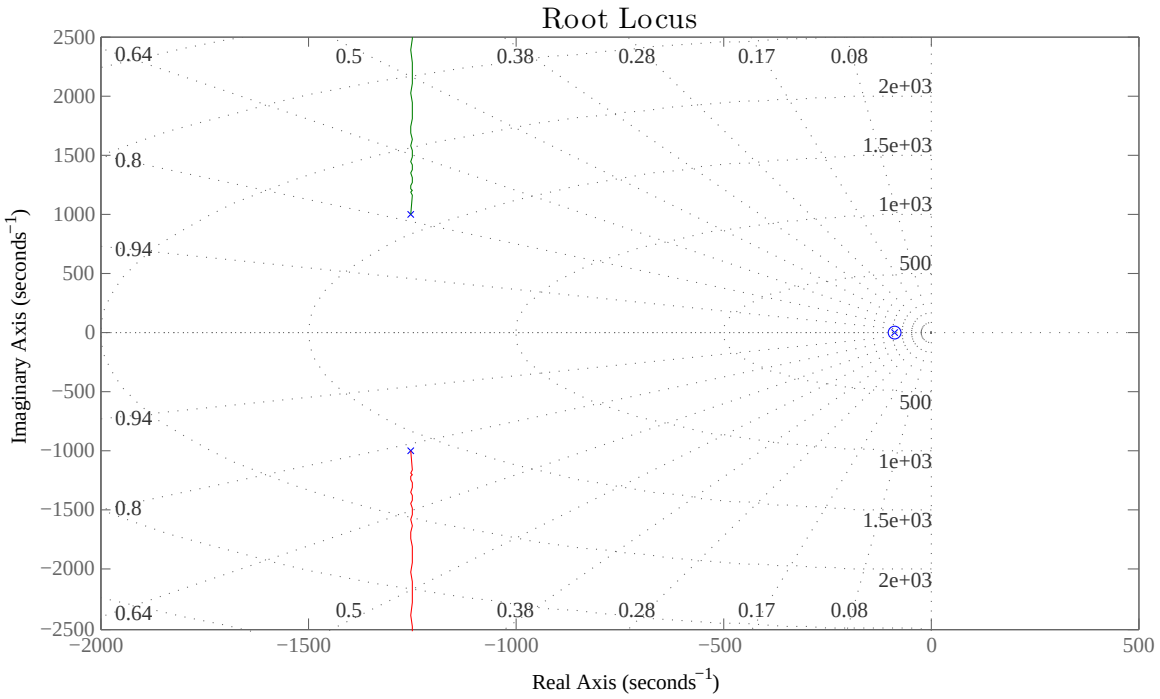

Figure 3.5. Current closed loop root locus with inclusion of the system time delay.

From Figure 3.4 and 3.5 it can be concluded that the designed PI controller removes the steady state error, reduces the settling time, produces the desired overshoot, and maintains the system stable hence the current controller design requirements are fulfilled. The closed-loop bandwidth is 1438.3 `rad/s`.

3.3.1 Experimental Verification

To verify that the designed PI controller parameters produce an acceptable step response in the dSPACE setup, Figure 3.6 presents the experimental results obtained for a 10 `A` q-axis step response at 1000 `min`$^{-1}$.

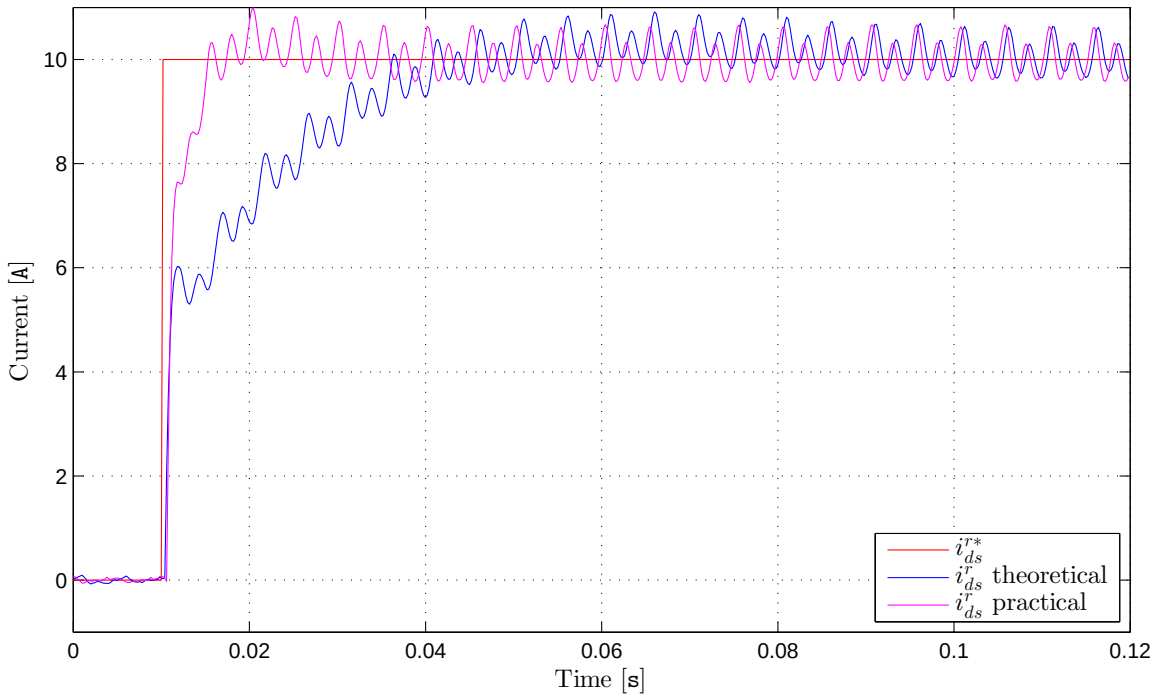

Figure 3.6. Experimental closed loop dSPACE d-axis current response, including the response based on the theoretical- and readjusted PI parameters.

As seen in Figure 3.6 the theoretically designed PI parameters do not produce the expected response in the dSPACE setup. The 10 % settling time is calculated to 25.4 ms, the rise time to 24.8 ms, and the overshoot to approx. 3%. The settling time in this thesis is defined as the time is takes to get within 10 % of the final value.

In the theoretical design procedure the non-linearities of the inverter are not considered. The non-linearities, such as dead-time and conduction losses causes distortion of the inverter voltages, sacrificing the PI controller performance if the parameters are not adjusted. The practical PI parameters are therefore readjusted to $K_{pc} = 2.7$ and $K_{ic} = 1000$. The parameters are tuned by first setting the integral gain $K_{ic} = 0$, and then increasing the proportional gain K_{pc} until a further increase causes oscillation. Then K_{ic} is increased until the desired overshoot is reached. Using this procedure insures that the proportional gain is tuned correctly to obtain a proper system bandwidth. Addition of the integral gain then eliminate any steady state error, and adjusts the damping of the response. These parameters are adapted for computer simulations. The 10 % settling time is calculated to 4.7 ms, the rise time to 4 ms, and the overshoot to approx. 2% after the parameter adjustment which is more acceptable, even though the rise time is too high compared to the initial requirements.

3.4 Speed Loop Controller Design

In order to control the speed of the PMSM drive system, a PI controller is utilized in an outer speed loop. The speed of the outer loop is dependent on the speed of the inner q-axis current loop. The speed loop PI controller is designed based on the mechanical system of which the PMSM forms part of. In (3.13) the mechanical system equation (2.15) is repeated using the Laplace variable to form the speed loop transfer function.

$$T_e(s) = B_m\omega_m(s) + J_m s\omega_m(s) + T_l(s) + J_0 \quad [-] \tag{3.13}$$

In order to control the mechanical speed the electromagnetic torque of the machine, which is a direct product of the q-axis current according to (2.14) is to equalize the mechanical torque. The electromagnetic torque is given as shown in (3.14) by considering that $i_{ds}^{r*} = 0$ and $L_d = L_q$

$$T_e = K_t i_{qs}^r = \left(\frac{3}{2}P_p\lambda_{pm}\right) i_{qs}^r \quad [-] \tag{3.14}$$

where:
K_t is the machine torque constant.

In order to obtain the transfer function for the speed loop, the load torque T_l and Coulomb friction are modelled as disturbances for the speed loop controller, as their combined magnitude is a variable in the practical setup. The block diagram for the speed loop is shown in Figure 3.7.

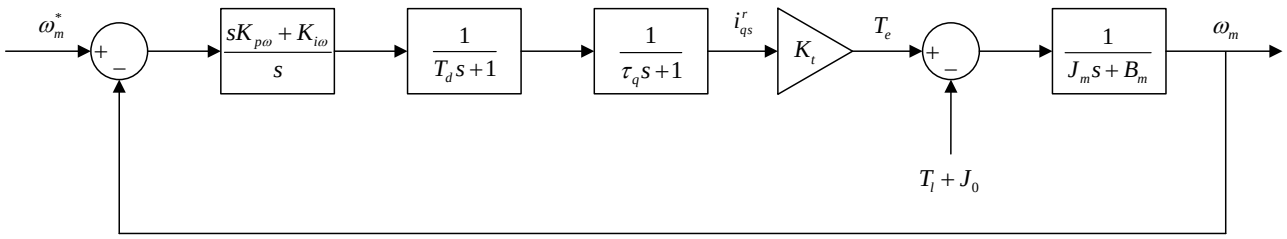

Figure 3.7. Block diagram of the speed loop including the approximate current loop delay and system delay.

The open-loop transfer function for the speed loop can according to Figure 3.7 be formulated as in (3.15) when the load torque and Coulomb friction are modelled as disturbances.

$$\frac{\omega_m^*(s)}{\omega_m(s)} \cong \frac{sK_{p\omega} + K_{i\omega}}{s}\frac{1}{T_d s+1}\frac{1}{\tau_q s+1}K_t\frac{1}{J_m s + B_m} \quad [-] \tag{3.15}$$

The simplified open-loop speed transfer function is a third order system when excluding the PI controller. Again the delays present in the system are modelled as a first order lag system, including the DSP calculation and ADC delays equal to $T_d = 0.4$ ms. The inner q-axis current loop which is a second order system, is approximated as a first order lag system in order to simplify the design of the speed controller. The approximate time constant representing the delay from the inner current loop is found from Figure 3.4 to $\tau_q = 1.15$ms.

Concerning the design of the PI speed controller, the controller requirements must be met. Therefore in order to investigate what must be modified in the speed loop, the uncompensated closed-loop step response is shown in Figure 3.8.

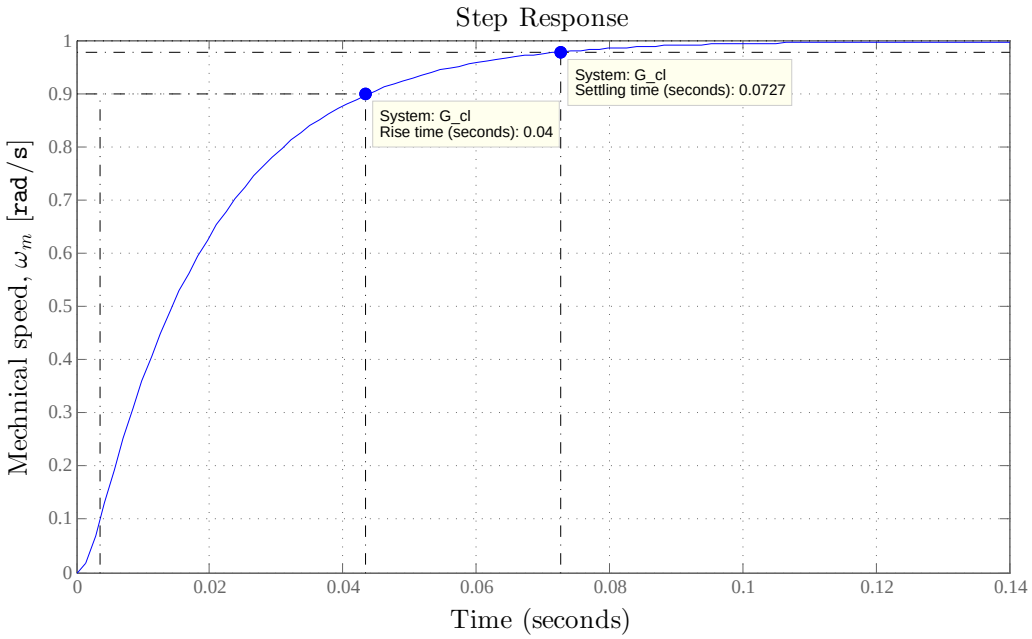

Figure 3.8. Uncompensated speed closed loop step response with inclusion of the system time delays and simplified current loop delay.

As seen in Figure 3.8 the loop is stable, and has a relatively fast transient response without compensation. Due to the viscous damping, the steady state value is 0.2% from the reference. The transient response is dominated by the single mechanical pole. In order to respect the requirements the mechanical pole effects must be suppressed using the PI controller. According to the requirements, the speed loop should be faster and must be able to reject external disturbances. As the loop does not contain an integrator the loop will not reach the reference value if load torque is applied.

The parameters of the PI controller are determined such that the speed loop response is sped up, and a phase-margin $> 45°$, and gain margin > 8dB to assure proper stability margins. [Phillips, 2011]

For robustness and fast disturbance rejection, the loop gain must be large over the largest possible frequency range without increasing the disturbance effects on the system output. Using the information from the open-loop bode diagram in Figure 3.9 indicates that the bandwidth is approx. 60dB. The bandwidth is proportional to the rise time, hence the bandwidth should be increased according to the requirements. Therefore the loop gain should be increased to achieve a faster transient response and better disturbance rejection.

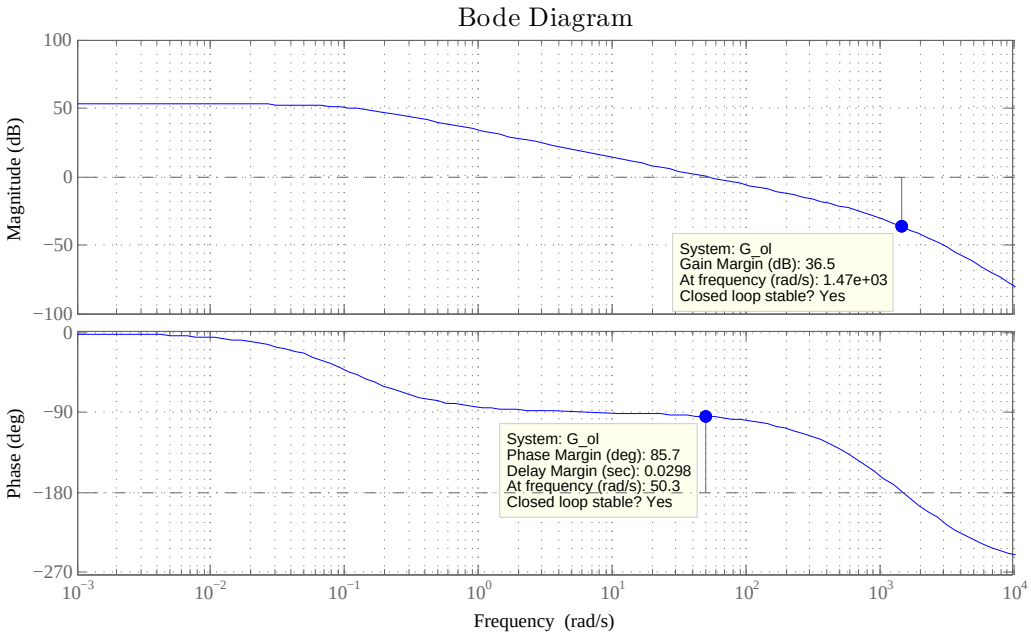

Figure 3.9. Uncompensated speed open-loop bode diagram with inclusion of the system time delays and simplified current loop delay.

Using PIDtool, which is a graphical user-interface found in the MATLAB software package, the controller gains are adjusted until the desired closed-loop step response characteristics are obtained. By inserting two dominating complex conjugated poles in the closed loop transfer function, the requirements are met. The controller parameters obtained are $K_{p\omega} = 1.41$ and $K_{i\omega} = 46.61$ which produces the closed-loop step response shown in Figure 3.10.

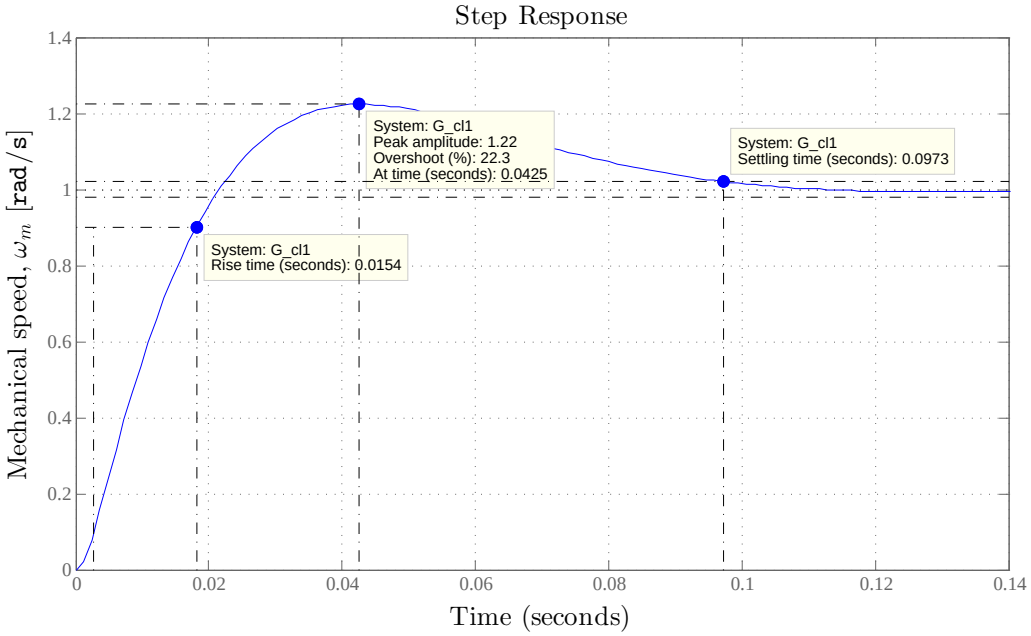

Figure 3.10. Compensated speed closed loop step response with inclusion of the system time delays and simplified current loop delay.

It is seen that the requirements to the rise time and the overshoot are met compared to the theoretically designed current controller. The closed-loop system is stable. To show the stability margins and disturbance rejection capabilities, the Bode diagram for the closed loop system is shown in Figure 3.11.

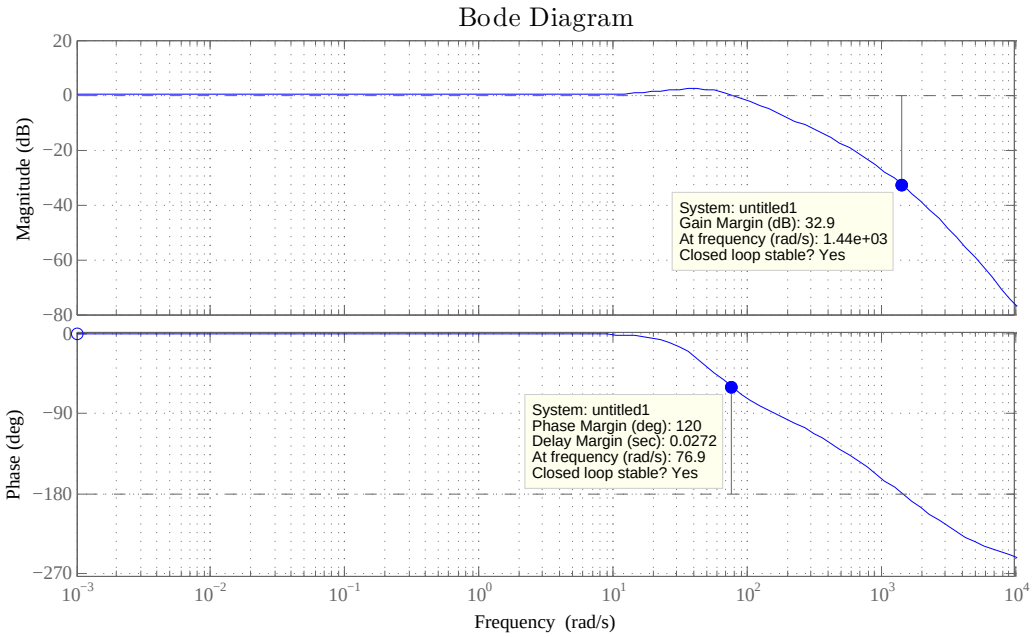

Figure 3.11. Compensated speed closed-loop bode diagram with inclusion of the system time delays and simplified current loop delay.

It is seen that the bandwidth is increased to approx. 110dB and that the phase margin and the gain margin requirements are respected. It can also be seen that an overshoot is expected for a step input due to the resonance peak which is caused by the complex conjugated pole. By analysing the closed loop step response including DC step load torque disturbances, the effectiveness of the PI controller was verified using Simulink. For optimizing the speed loop in the practical setup, the proportional gain of the speed controlelr should be decreased a few percent, to decrease the speed of the loop in the laboratory setup, such that the controller requirements are met.

3.5 Integral Wind-up Compensation

When designing the current- and speed loop controllers, the controller output signals can reach very high amplitudes which are outside of the system hardware limitations shown in Table 2.1. In order to avoid these undesired and damaging control signals, a saturation block is inserted after the controller. The saturation block resets the input to the maximum or minimum allowed value if the input is either larger or less than the allowable limits. This causes the control signal amplitude to respect the constraints of the practical system.

Unavoidable, since the PI control algorithm assumes the manipulated variable is unconstrained, the integral error term continues to grow without bound when the manipulated variable does saturate due to the saturation block. The outcome of this scenario is that the response becomes overly oscillatory since the integral value is still large. This is known as integral wind-up.

By using a technique called anti-windup tracking, the integral windup can be prevented. The principle is to compute the difference between the desired manipulated variable and the saturated version, and feed this back to the integrator within the PI controller.

The integral anti-windup block diagram is shown in Figure 3.12 for the speed loop controller.

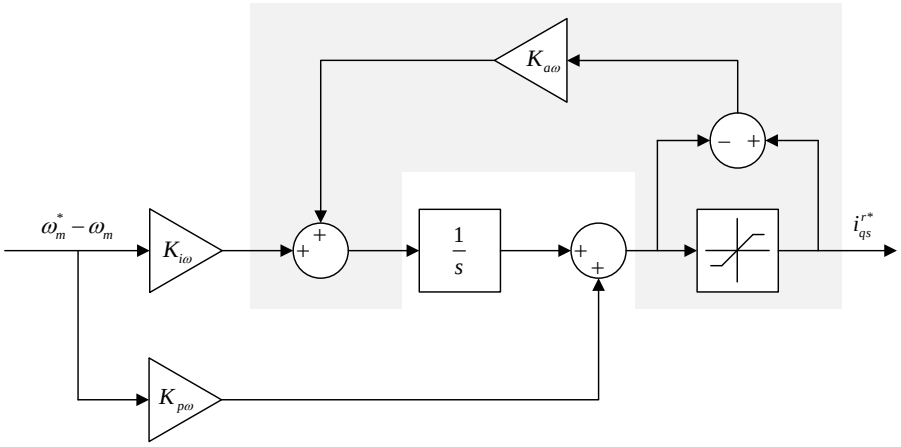

Figure 3.12. Block diagram of the anti-windup configuration applied to the speed loop PI controller. The grey area represents the anti-windup tracking technique.

The anti-windup gain $K_{a\omega}$ is chosen based on analysis of the system model and is chosen to $K_{a\omega} = 2K_{i\omega}$. The modified controller reduces the overshoot, but decreases the rise time of the response since the rate of change of the speed is now limited by the saturation block. The same anti-windup configuration is applied to the d- and q-axis current PI controllers to respect the electrical limitations of the system.

Chapter 4
Predictive Deadbeat Control

In this chapter the predictive deadbeat control theory is described. The theory forms basis for designing the predictive deadbeat controller in simulations and experiment. The conventional deadbeat controller which is based on a discretized PMSM model is first presented. It is followed by development of a technique that can mitigate the effects of digital implementation by predicting the machine currents. To compensate for the non-linear behaviour of the inverter, which deteriorates the controller performance, this chapter also presents a dead-time compensation technique for the predictive deadbeat controller.

Furthermore, to remain in the linear region of the SVPWM technique a limitation on the controller voltages are incorporated in the deadbeat controller. Finally, as the rotor position is also delayed by the digital implementation, a compensation for this delay is presented. To summarize, the predictive deadbeat algorithm is at the end of the chapter presented in a flowchart.

4.1 Deadbeat Control

Conventional deadbeat control is an utilization of the pole placement method, that places the pole(s) of the controlled discrete system at the origin of the discrete z-plane. If the system is controllable such that any arbitrary poles are allowable, then placing them at the origin will eliminate the system dynamics hence achieving a near perfect response.

In deadbeat control, any nonzero error vector will be driven to zero in at most n sampling periods if the amplitude of the scalar control input $u(k)$ is unbounded, where n is the order of the controlled system. There exist only one design parameter in deadbeat control which is the sampling time. Using a low sampling time causes the settling time to become small. When using a low sampling time it implies that the control signal $u(k)$ must have an extremely large magnitude, which in psychical systems causes a problem, since the control signal is bounded by the system hardware limitations. Therefore in the design of actual deadbeat control one must be aware of the trade-off between magnitude of the control signal and the response speed.

4.2 Deadbeat Current Control

The controller structure of the deadbeat controller is shown in Figure 4.1. It can directly replace the inner PI current controllers used in the classical FOC scheme shown in Figure 3.2. As in classical FOC the machine voltages are generated using the SVPWM block to control the inverter. This guaranties a fixed switching frequency, which simplifies the design of a possible input filter.

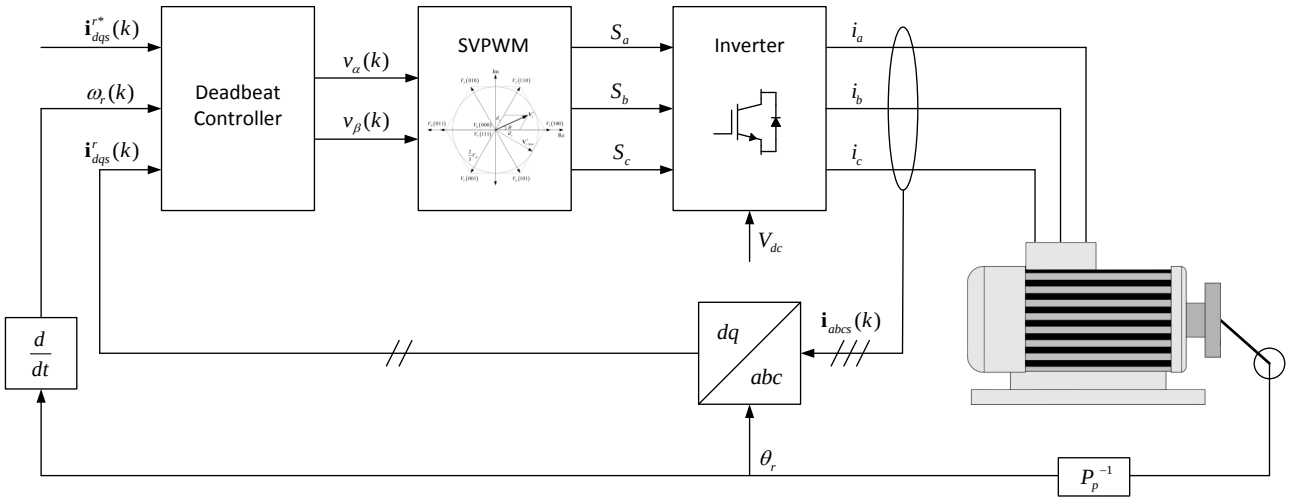

Figure 4.1. Sensored deadbeat current controlled PMSM drive.

The deadbeat control algorithm is based on the electrical machine model. By discretizing the model, the voltage required to obtain the desired current vector $\mathbf{i}^{r*}_{dqs}(k)$ at the next sampling instant can be obtained. The electrical machine model equations (2.12) and (2.13) can be discretized and thereby approximated using Newton's forward difference quotient as shown in (4.1) by assuming a fixed sampling time approaching zero.

$$\frac{di(t)}{dt} \approx \frac{i(k+1) - i(k)}{T_s} \quad [\mathtt{A/s}] \tag{4.1}$$

By substituting the derivatives in (2.12) and (2.13) and rearranging for the currents at the next sampling instant, the necessary discretized model is obtained as shown in (4.2) and (4.3).

$$i^r_{ds}(k+1) = \frac{T_s}{L_d} v^r_{ds}(k) + \left(1 - \frac{T_s R_{ph}}{L_d}\right) i^r_{ds}(k) + \frac{T_s \omega_r(k) L_q}{L_d} i^r_{qs}(k) \quad [\mathtt{A}] \tag{4.2}$$

$$i^r_{qs}(k+1) = \frac{T_s}{L_q} v^r_{qs}(k) + \left(1 - \frac{T_s R_{ph}}{L_q}\right) i^r_{qs}(k) - \frac{T_s \omega_r(k) L_d}{L_q} i^r_{ds}(k) - \frac{T_s \omega_r(k) \lambda_{pm}}{L_q} \quad [\mathtt{A}] \tag{4.3}$$

By sampling at a rate small enough to neglect the changes of electrical angular speed $\omega_r(k)$, the otherwise nonlinear speed voltages, can be considered as constants. [Rodriguez, 2012]

In order to obtain the deadbeat control voltages, the current reference is set equal to the currents at the next sampling instant $\mathbf{i}^{r*}_{dqs}(k) = \mathbf{i}^{r}_{dqs}(k+1)$, as shown in (4.4) and (4.5) which are rearranged for the desired deadbeat control voltages.

$$v^r_{ds}(k) = L_d \left(\frac{i^{r*}_{ds}(k) - i^r_{ds}(k)}{T_s}\right) + R_{ph} i^r_{ds}(k) - \omega_r(k) L_q i^r_{qs}(k) \quad [\mathtt{V}] \tag{4.4}$$

$$v^r_{qs}(k) = L_q \left(\frac{i^{r*}_{qs}(k) - i^r_{qs}(k)}{T_s}\right) + R_{ph} i^r_{qs}(k) + \omega_r(k) L_d i^r_{ds}(k) + \omega_r(k) \lambda_{pm} \quad [\mathtt{V}] \tag{4.5}$$

By assuming $\mathbf{i}^{r*}_{dqs}(k) - \mathbf{i}^{r}_{dqs}(k) = 0$ at sampling instant k it can be seen that the reference voltages need not change in the next sampling instant since the speed voltages are constant. The deadbeat control method functions as a kind of high gain proportional controller if the rotor speed and back-EMF terms are compensated properly.

4.3 Predictive Current Delay Compensation

Ideally, the deadbeat control voltages produces zero current error within one sampling interval T_s, but since digital signal processing are used in the psychical drive system, the evaluation of the deadbeat control voltages causes an inherent calculation delay, hence the deadbeat voltages are first available at the beginning of the $(k+1)$th sampling interval. Not taking this delay into account will cause the current loop response to exhibit persistent oscillation. [Springob and Holtz, 1998] [Moon et al., 2003]

The variables on the right hand side of (4.4) and (4.5) are acquired at the sampling instant k, but due to the DSP calculation delay, the voltages are first applied at the beginning of the $(k+1)$th sampling interval. This signal delay can be overcome using a current predictor that predicts the currents one sampling period ahead and then use this prediction to calculate the deadbeat voltages. Using (4.2) and (4.3) to predict the currents, the improved deadbeat voltages can be written as (4.6) and (4.7)

$$v_{ds}^r(k+1) = L_d\left(\frac{i_{ds}^{r*}(k) - \hat{i}_{ds}^r(k+1)}{T_s}\right) + R_{ph}\hat{i}_{ds}^r(k+1) - \omega_r(k)L_q\hat{i}_{qs}^r(k+1) \quad [\mathrm{V}] \tag{4.6}$$

$$v_{qs}^r(k+1) = L_q\left(\frac{i_{qs}^{r*}(k) - \hat{i}_{qs}^r(k+1)}{T_s}\right) + R_{ph}\hat{i}_{qs}^r(k+1) + \omega_r(k)\left(L_d\hat{i}_{ds}^r(k+1) + \lambda_{pm}\right) \quad [\mathrm{V}] \tag{4.7}$$

where $\hat{i}_{ds}^r(k+1)$ and $\hat{i}_{qs}^r(k+1)$ are calculated using respectively (4.2) and (4.3) based on the previous sampling.

By implementing the delay compensation, the calculation time increase. Therefore the deadbeat voltages are first applied at the $(k+2)$th sampling interval as the predicted current is available at the beginning of the $(k+1)$th sampling period.

The difference between the ideal timing sequence and the delay compensated timing sequence can be seen by comparing Figure 4.2 and 4.3.

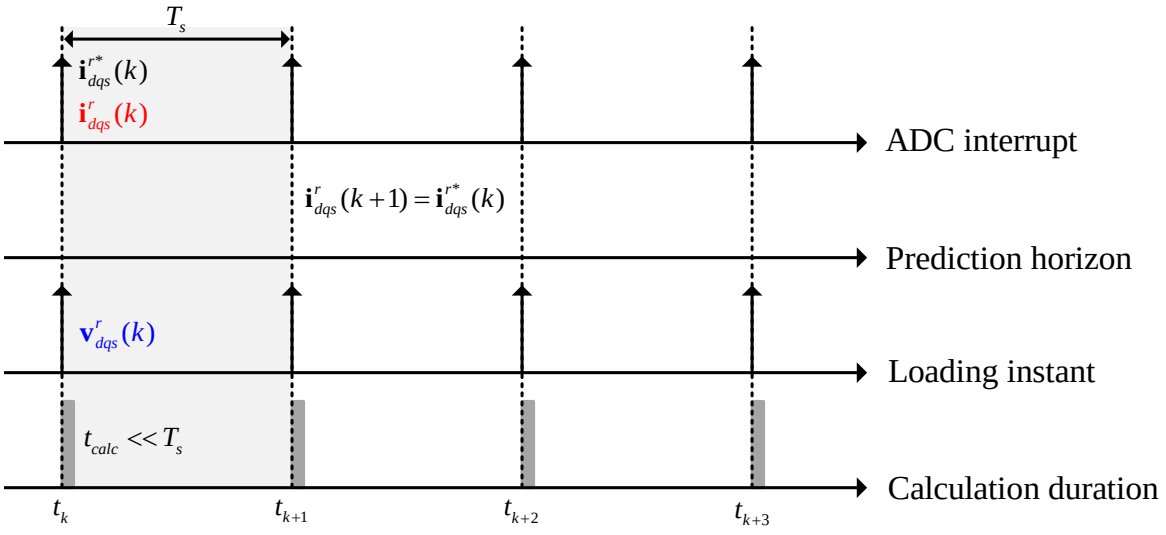

Figure 4.2. Ideal timing sequence for the deadbeat control when using a DSP. (red: measurements from ADC, blue: calculated variables)

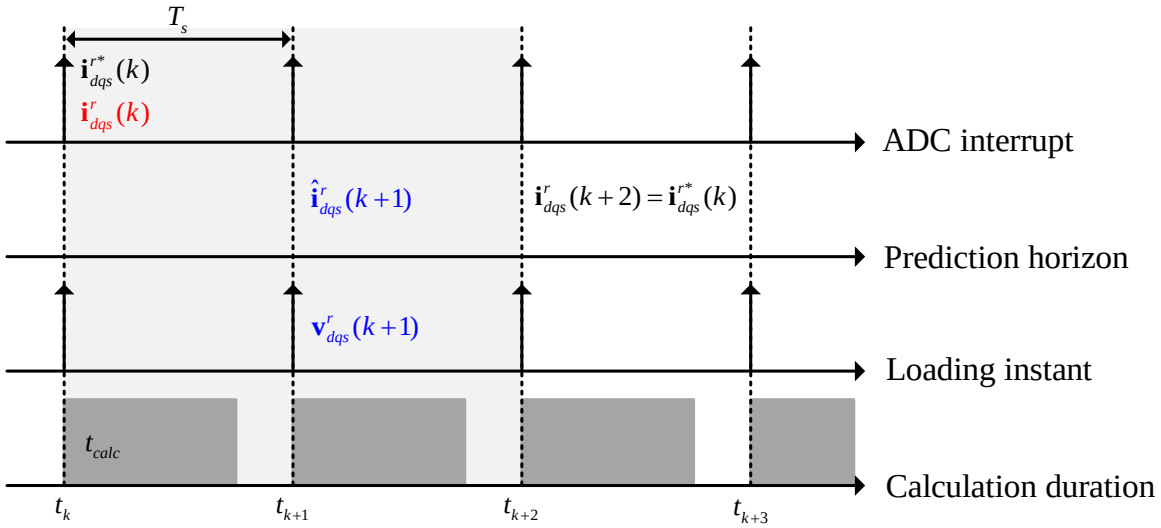

Figure 4.3. Delay compensated timing sequence for the deadbeat control when using a DSP. (red: measurements from ADC, blue: calculated variables)

4.3.1 Rotor Position Delay Compensation

As the rotor angular speed is also read by the DSP and is utilized with the delayed voltages, due to the calculation of the current prediction, followed by the delay compensated deadbeat voltages, the rotor position must also be compensated to improve the calculated deadbeat voltages. By phase shifting the deadbeat stator voltage vector, the change of the rotor position during calculation can be compensated. By phase shifting the stator voltage vector with $1.5T_s\omega_r(k)$, the calculated deadbeat voltages are adjusted to the delay caused by the DSP sampling and calculation delay. Shifting the stator voltage vector 1.5 sampling period, has on the basis of simulation- and experimental results shown to be the optimal value. The rotor position is read at the kth interrupt, and the deadbeat voltages are applied during the $(k+1)$th period. When the rotor rotates, there is a rotor position difference between these two samples. As the voltages are applied during the $(k+1)$th period, the difference in rotor position approx. occurs for 1.5 period.

The phase shift is incorporated in the model by multiplying the complex stator voltage vector with $e^{1.5T_s\omega_r(k)}$. Results obtained based on this phase shift show an improvement of the steady state accuracy.

4.4 Deadbeat Voltage Constraint

As in the case of using FOC with PI current controllers, the physical limits of the system hardware must be respected at all times in order not to damage the system. Therefore, a restriction on the maximum deadbeat voltages must be incorporated. The reference voltage vector for the SVPWM, has a maximum amplitude in order to operate within the linear modulation region. This criteria is therefore implemented as the limit for the maximum deadbeat voltages.

If the amplitude of the deadbeat voltage vector is outside of the maximum allowable limit of $V_{dc}/\sqrt{3}$, the d- and q-axis voltages are modified according to (4.8) and (4.9).

$$v^{r*}_{ds}(k+1) = \frac{v^{r}_{ds}(k+1)}{|\mathbf{v}^{*}_{s}(k+1)|}\frac{V_{dc}}{\sqrt{3}} \quad [\mathrm{V}] \tag{4.8}$$

$$v^{r*}_{qs}(k+1) = \frac{v^{r}_{qs}(k+1)}{|\mathbf{v}^{*}_{s}(k+1)|}\frac{V_{dc}}{\sqrt{3}} \quad [\mathrm{V}] \tag{4.9}$$

By using (4.8) and (4.9), the deadbeat voltages are scaled according to the maximum voltage available, where the deadbeat voltage vector amplitude is calculated as in (4.10).

$$|\mathbf{v}_s^*(k+1)| = \sqrt{v_{ds}^r(k+1)^2 + v_{qs}^r(k+1)^2} \quad [\mathrm{V}] \tag{4.10}$$

The effect of implementing the voltage scaling is that the deadbeat constraint is relaxed in certain cases. In case of commanding a high amplitude current step, the required voltage is unavailable and only the maximum voltage is applied as the deadbeat voltage. In such a scenario the rise time increase due to the voltage limitation.

4.5 Dead-time Compensation

When using the VSI to synthesize variable frequency voltages for the PMSM, the non-linearities that exist for practical switching devices must be taken into account as they cause distortion of the voltage output, and thereby affect the closed-loop control performance. The switching devices in the inverter are IGBTs that require turn-on and turn-off time, corresponding respectively to the transient periods when the devices are turned on and off. Furthermore, in order to avoid the shoot trough phenomenon, that is a short circuit of the DC link when one switch is turned on and the other has not yet turned off completely, a dead-time is added between the activation of the top and bottom switches.

Since the inverter non-linearities seriously affects the output voltages, several articles have presented compensation techniques that can compensate for the inverter non-linearities. In [Kim et al., 2010] the authors have used a vectorial disturbance estimator to identify the error voltages, whereas in [Hwang and Kim, 2010] the authors use the *d*-axis current harmonics to identify the error voltages, which in turn compensates both the fundamental and harmonic components.

Based on the phase *a* leg as shown in Figure 4.4, the effect of the inverter non-linearities can be examined and illustrated.

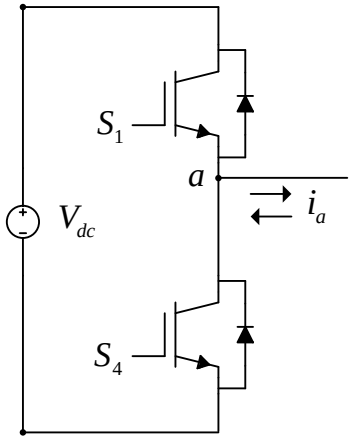

Figure 4.4. Phase *a* leg of the three phase VSI.

The dead-time delay is intentionally inserted to avoid shoot through, and has a time equal to at least the sum of the storage time, current fall time, and voltage rise time of the device. These times vary with system operation point and temperature, and therefore it is prudent to add a small safety margin. Depending on the polarity of the phase current, the effect of the dead-time delay and psychical device characteristics can be illustrated as shown in Figure 4.5.

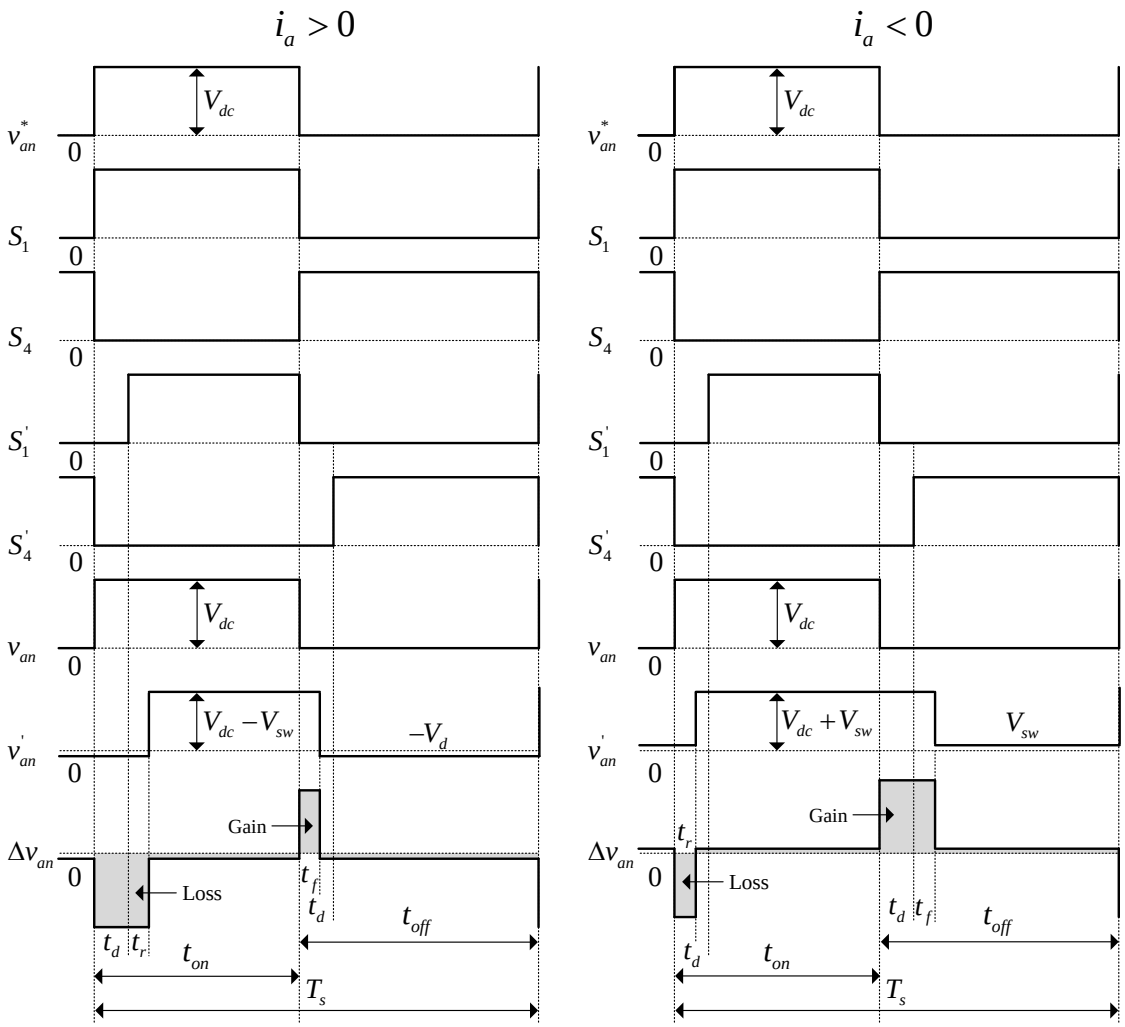

Figure 4.5. Dead-time effects with practical devices.

Considering the effects of a real IGBT for switching, shows according to Figure 4.5, that when the load current is positive the desired voltage v_{an} as illustrated by the shaded area for Δv_{an}, is distorted by an amount of lost volt-seconds hence the actual voltage is different than the desired voltage. This difference in output voltage also occurs when the load current is negative, the difference is that the actual output voltage is gained by the amount of volt-seconds equal to the shaded area for Δv_{an}. The mathematical representation of the average voltage distortion can be formulated as the total shaded area in Figure 4.5 as shown in (4.11). [Krishnan, 2010]

$$\Delta V_{an} = \frac{t_d + t_r + t_f}{T_s}(V_{dc} - V_{sw}) + \frac{t_{off} + 2t_d + t_r - t_f}{T_s}V_d + \frac{T_s - t_{off} - t_d + t_f}{T_s}V_{sw} \quad [\mathrm{V}] \tag{4.11}$$

As many of the parameters in (4.11) are not constants but are dependent on device current and temperature, it is very difficult to calculate the precise amount of voltage distortion. By analysing (4.11), it can be observed that the time delays generally cause poor performance if the duty cycle is low, as then the size of the shaded area is increased compared to the total area. What it means is that the voltage loss is relatively high at low-voltage commands and has less influence at high-voltage commands.

Considering that the rise- and fall times in (4.11) are load- and temperature dependent, and that their effect, and the device voltage drops are not in the scope of this thesis, these are excluded concerning compensation for the inverter voltage distortion. As seen in Figure 4.5 the voltage distortion due to the dead-time is highest. Therefore, by neglecting the non-linear device characteristics the average voltage distortion both for negative, and positive load currents can be described as in (4.12) [Hwang

and Kim, 2010]

$$\Delta V = \frac{t_d}{T_s} V_{dc} \quad [\mathtt{V}] \tag{4.12}$$

where:
t_d is the inverter dead-time

This amount of voltage loss/gain must be added to the dq deadbeat voltage references before generating the machine terminal voltages. In the experimental setup the dead-time is implemented in the inverter hardware and is set to 2.5 $\mu\mathtt{s}$ according to the recommendations from Danfoss. For a 528 $\mathtt{V}$ DC link voltage, and a switching period of T_s=1/5000 $\mathtt{s}$ the average voltage error is 6.6 $\mathtt{V}$.

In [Sukegawa et al., 1991] a method for adding the distortion voltages to the d- and q- axis reference voltages has been proposed. It is a feed-forward compensation method, meaning that the compensation voltages are calculated and added to the d- and q-axis voltages using knowledge of the current space vector position before generating the d- and q-axis voltage references. The average distorted voltages can be obtained based on the polarity of the three phase currents as shown in Figure 4.6 for phase a. [Hwang and Kim, 2010]

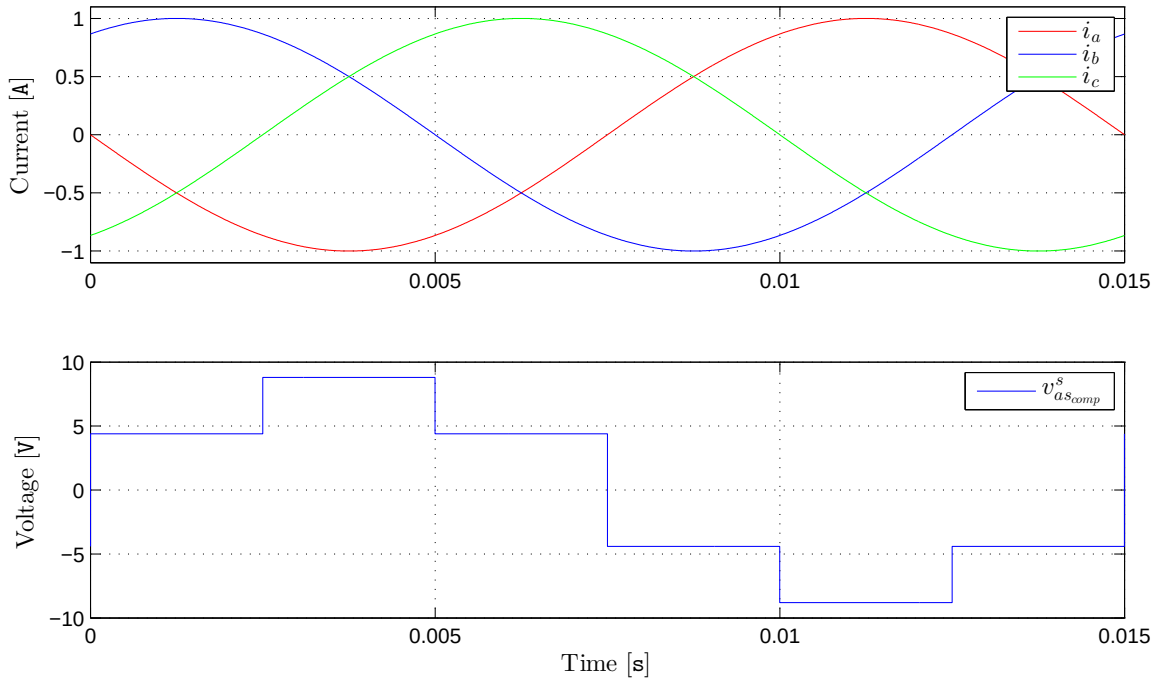

Figure 4.6. Stationary 66.667 $\mathtt{Hz}$ phase a six step dead-time distortion voltage (bottom) generated based on the polarity of the three phase currents (top).

The phase b and c distortion voltages are similar, just shifted 120° and 240° in phase. The distorted three phase voltages generate primarily 5th and 7th order harmonics in the machine currents because of the voltage distortion waveform. These distorted voltages transform into 6th order harmonics in the rotor fixed reference frame, hence it can be expected that the dead-time deteriorates the torque performance, as the electromagnetic torque is a product of the q-axis current.

Transforming the three phase distorted voltages into the two phase stationary $\alpha\beta$ reference frame, allows formulation of the distorted voltages in the rotor fixed dq reference frame as shown in Figure 4.7.

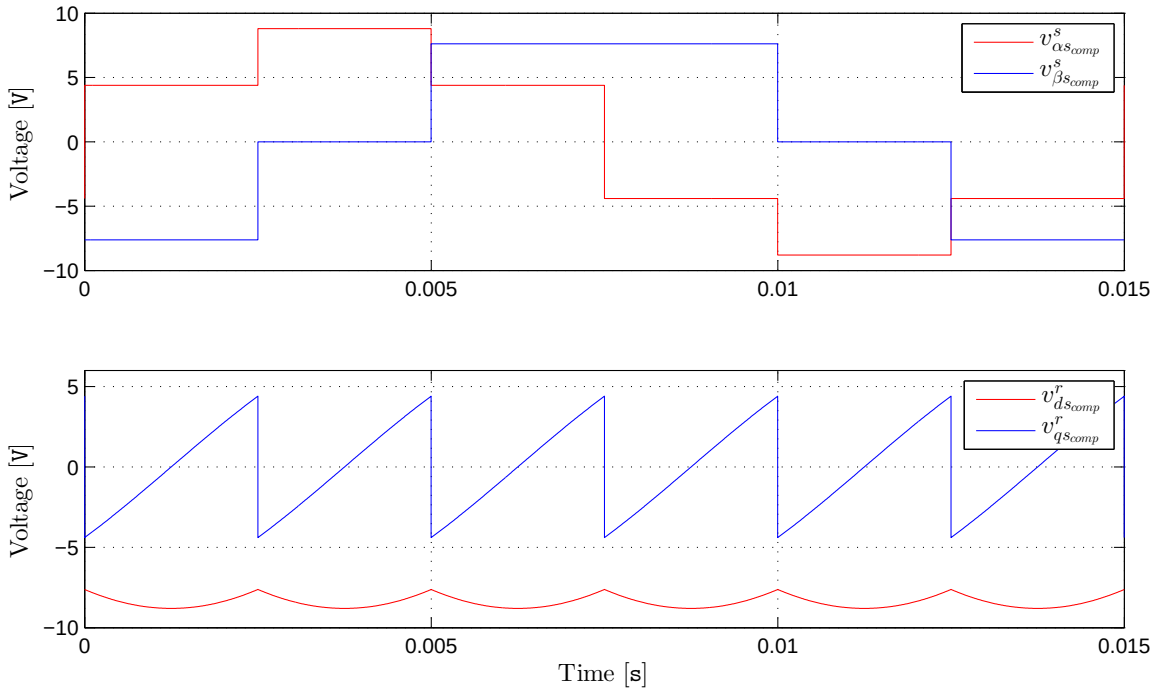

Figure 4.7. Stationary 66.667 Hz α and β dead-time distortion voltages (bottom). Rotor fixed d and q dead-time distortion voltages (bottom).

By feeding forward the d- and q-axis distortion voltages to the d and q voltage references, the dead-time effects are suppressed, hence both fundamental voltage amplitude correction and harmonic compensation are achieved.

Based on the d- and q-axis distortion voltages shown in Figure 4.7, [Sukegawa et al., 1991] has used the formulation in (4.13) and (4.14) to represent the signals. The formulation is adopted for this thesis.

$$v^r_{ds_{comp}} = \frac{4}{3}\Delta V \cos\left(\frac{\pi}{3}\text{Trunc}\left(\theta_r + \theta^* + \frac{\pi}{6}, \frac{\pi}{3}\right) - \theta_r\right) \quad [\text{V}] \tag{4.13}$$

$$v^r_{qs_{comp}} = \frac{4}{3}\Delta V \sin\left(\frac{\pi}{3}\text{Trunc}\left(\theta_r + \theta^* + \frac{\pi}{6}, \frac{\pi}{3}\right) - \theta_r\right) \quad [\text{V}] \tag{4.14}$$

where:
θ_r is the electrical angular position
θ^* is the current reference argument, $\tan^{-1}(i^{r*}_{qs}/i^{r*}_{ds})$
Trunc is the truncated value, denoted as $\text{Trunc}(A, B) = m$ when $A = mB + C$ and $C < B$

By using the presented formulation, the location of the current vector is incorporated, hence knowledge about the direction of the load currents are built-in and the voltage loss/gain is added as desired. Furthermore, the adopted equations uses the commanded current vector argument to insure proper voltage correction in four quadrant operation.

Using (4.13) and (4.14) to suppress the effects of dead-time, generates the d- and q-axis compensating voltages shown in Figure 4.8 while operating at 1000 min^{-1} for two cases.

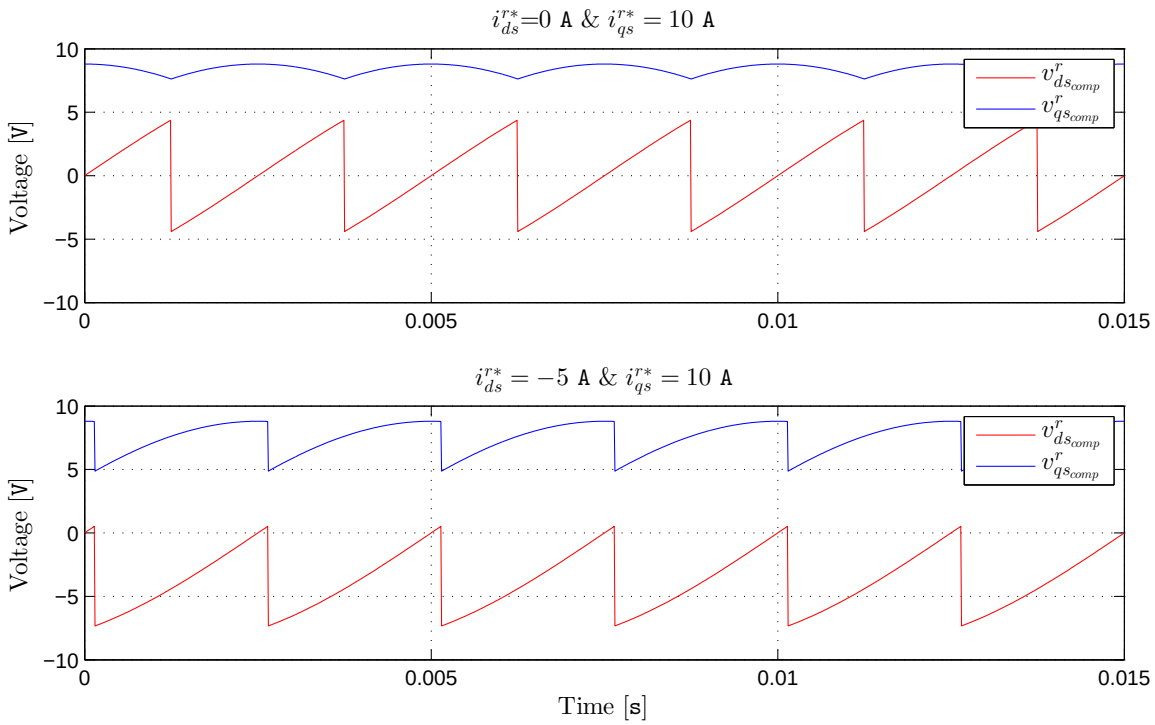

Figure 4.8. Dead-time compensation signal for solely q-axis current reference (top) and compensation signal for both d- and q-axis current references (bottom).

As seen using the zero direct axis current control strategy, the average value of the d-axis voltage is as expected very close to zero, whereas the q-axis voltage compensation as expected has an average value added to the voltage reference in order to compensate for the dead-time distortion. In the case where the d and q axes current are both commanded, the compensation signal shifts average value and shape in order to compensate properly for the new current vector position.

4.6 Implementation of Predictive Deadbeat Control

A flowchart illustrating the process of the deadbeat control algorithm, including the digital implementation delay compensation, the inverter dead-time compensation, and deadbeat voltage constraint is shown in Figure 4.9.

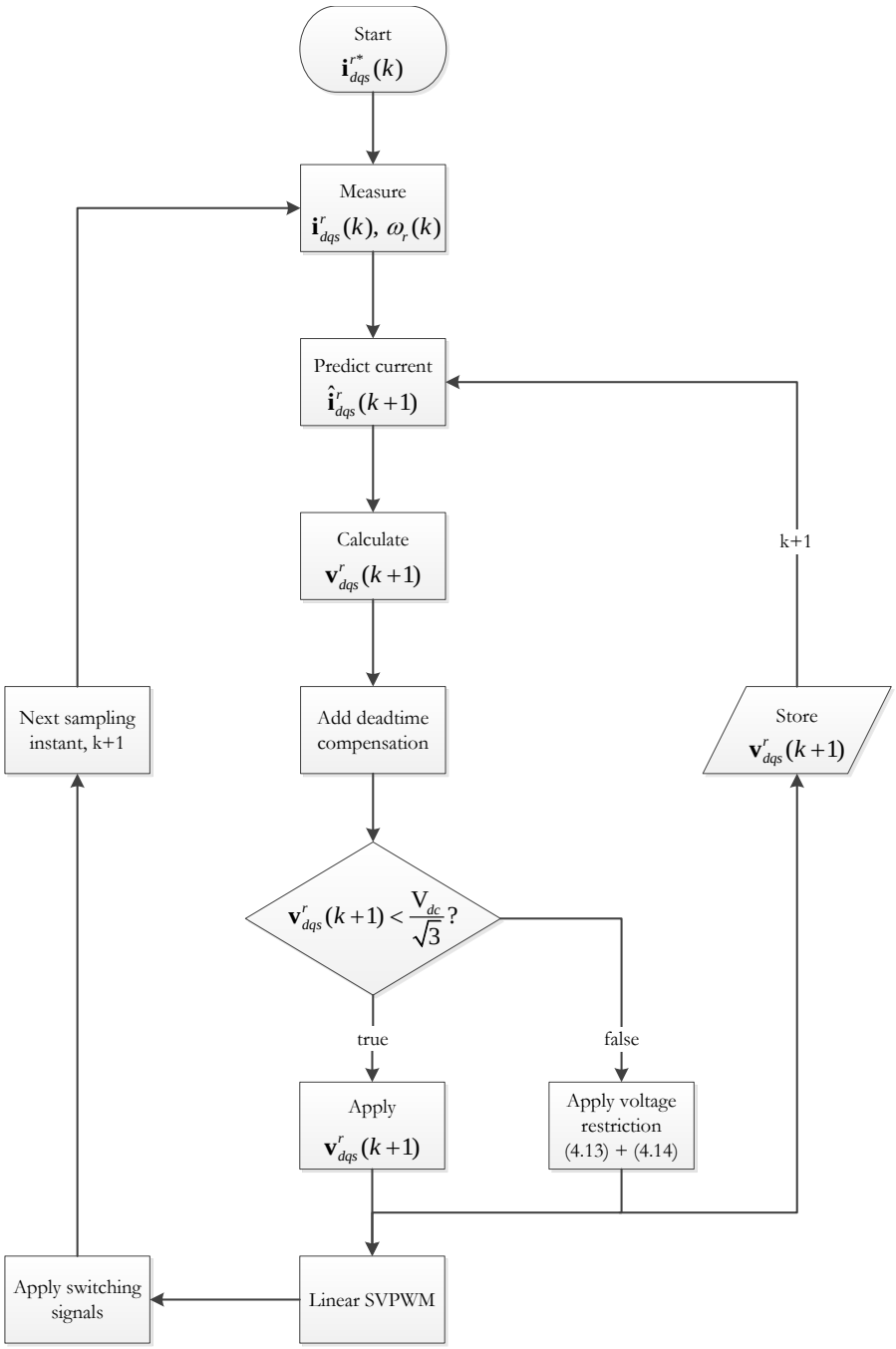

Figure 4.9. Flowchart of the predictive deadbeat control algorithm including inverter dead-time- and delay compensation.

The whole loop is executed once every sampling period. The previous value of the predicted voltage is stored as input for calculation of the next current prediction. After the delay compensated deadbeat control voltages are calculated, the dead-time compensation voltages are added, and a decision is taken if the voltage restriction must be utilized or not. Finally, the delay- and dead-time compensated voltage vector is synthesized to the machine terminals through the inverter using SVPWM, and the next sampling of the current and rotor speed is acquired.

Chapter 5
Simulation Results

This chapter is dedicated to analysis of simulation results obtained using two developed Simulink models, respectively the FOC PI Controller model and the alternative predictive deadbeat controller model.

The simulation models are used to verify the functionality of the controllers, and to form an idea of expected experimental performance. Characteristics such as settling time, overshoot, and steady state error are given for different operation conditions. The settling time in this thesis is defined as the time is takes to get within 10 % of the final value. The extracted information serve as a comparison of the two controller performances, and for comparison to the experimental performance in the following chapter.

To properly compare the simulation results of the models, they are tested under the exact same conditions. The conditions are listed as follows:

- The predictive deadbeat controller is based on the parameters in Table 2.1.
- The FOC PI controller parameters are $K_{pc} = 2.7$ and $K_{ic} = 1000$.
- The stator voltage vector is phase shifted by $1.5T_s\omega_r(k)$ due to position sampling delay.
- The DC-link voltage is fixed to 528 `V`.
- The DSP delay is modelled as an unit delay in a sampled subsystem.
- The simulation results are sampled at 5 `kHz`.

Since the experimental results are obtained using 5 `kHz` sampled dSPACE signals, the simulation results shown in this chapter are also sampled at 5 `kHz` to properly compare the responses.

The controller performances will be tested in three cases. A 0-10 `A` q-axis current step change, a 10-(-10) `A` q-axis current step reversal, and a -5 `A` d-axis current step change at $i_{qs}^r = 10$ `A` for the predictive deadbeat controller. All results are obtained at a constant mechanical speed of 1000 $\texttt{min}^{-1}$.

5.1 PI Control

The simulation results presented in this section are obtained using the classical FOC PI current controller developed in Chapter 3. The Simulink model of which the results are obtained is shown in Appendix B and can be found on the enclosed CD. In Figure 5.1 the simulation result of a 10 `A` q-axis current step command is presented.

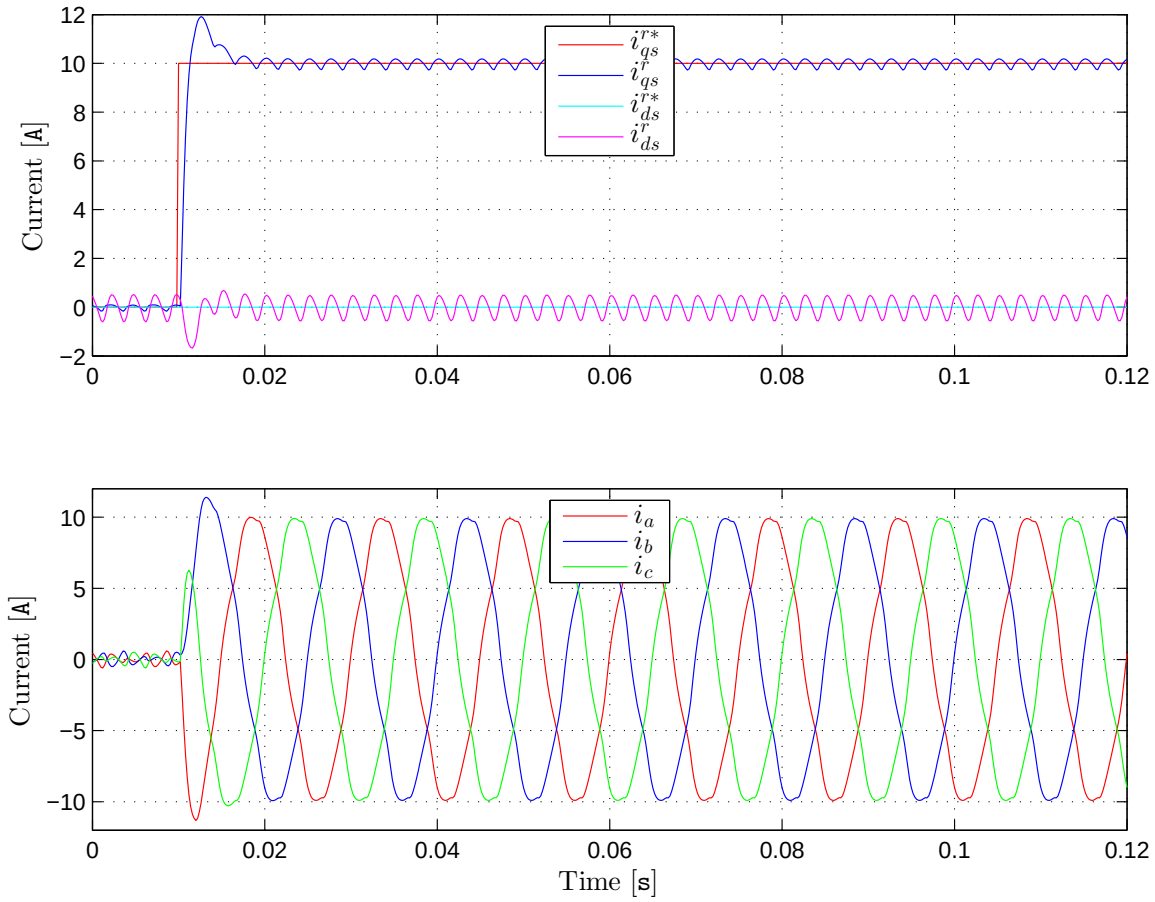

Figure 5.1. Simulated performance of a 10 A q-axis current step response. Sampled at 5 kHz.

The q-axis current has a settling time of approx. 9 ms and an initial overshoot of approx. 19 %. The average steady state error is eliminated both prior the q-axis current command and after, for both the d- and q-axis currents due to the controller integrator.

Figure 5.2 presents the simulation results obtained for a -10 A q-axis current step reversal command at an initial current of 10 A.

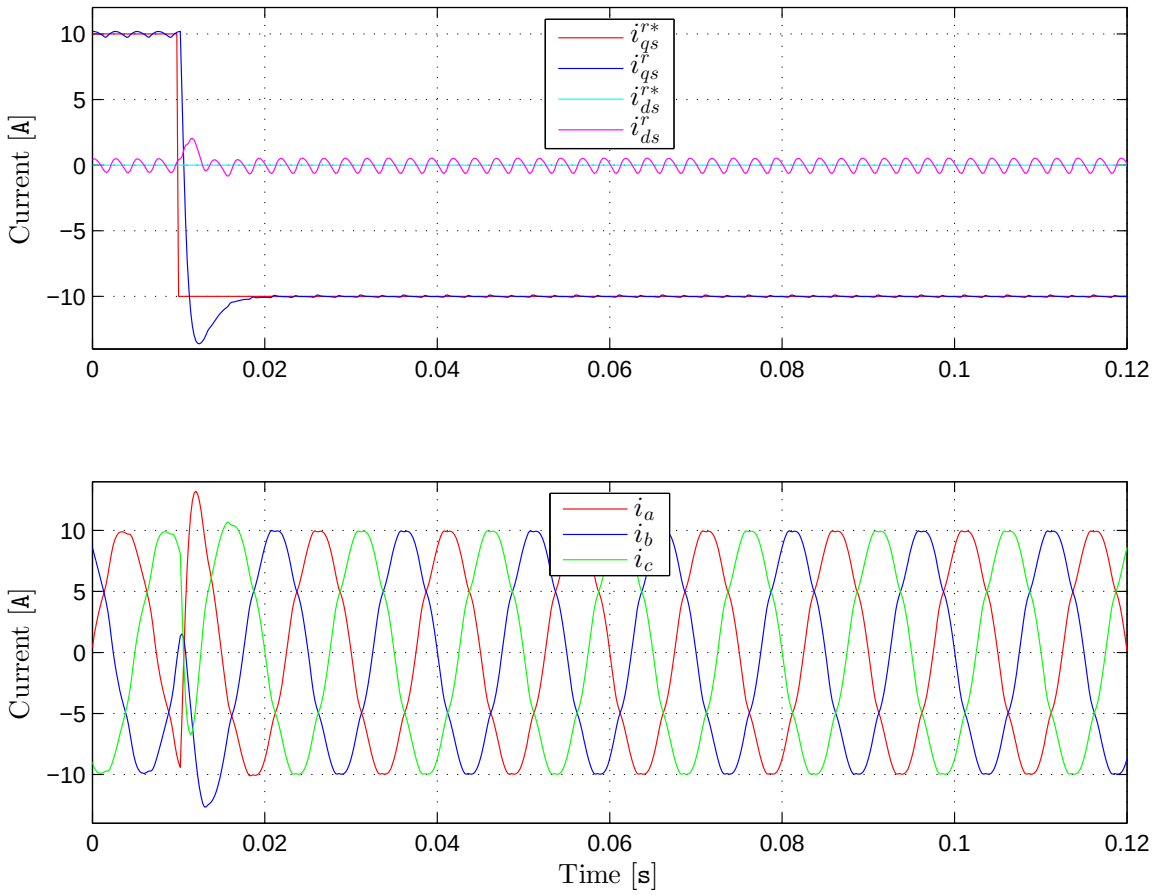

Figure 5.2. Simulated performance of a -10 A q-axis current step command when the initial current is 10 A. Sampled at 5 kHz.

From Figure 5.2 a settling time of approx. 9 ms and an initial overshoot of 40.5 % is observed. Again the average steady state error is eliminated.

Since the PI controller eliminates the steady state error continuously, further simulations show as expected that a step command for the d-axis current has similar characteristics as a step command for the q-axis current. Further figures are therefore not presented. The percent overshoot observed from the results are over the 2 % requirement. As the simulation controller parameters are the experimental parameters, the overshoot is explained as the inverter model components are ideal.

Based on the results in this section a low amplitude persistent oscillation is observed for both the q- and d-axis currents. This oscillation is caused by the model inverter dead-time. It causes as expected based on the analysis in Section 4.5 a distortion of the output voltages, hence the machine currents.

5.2 Predictive Deadbeat Control

This section presents the simulation results obtained using the predictive deadbeat current controller including dead-time- and digital delay compensation developed in Chapter 4. The Simulink model of which the results are obtained is shown in Appendix C and can be found on the enclosed CD. Figure 5.3 presents the results obtained for a 10 A q-axis current step command.

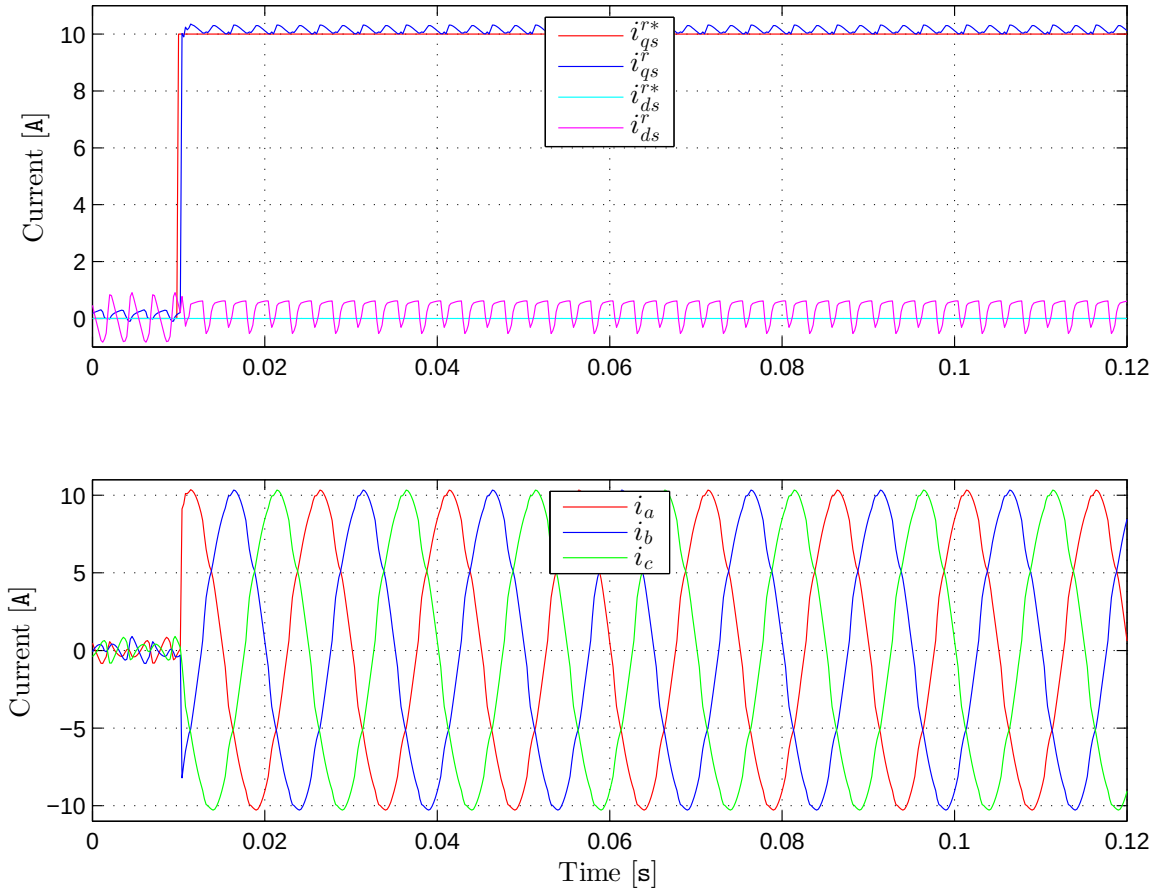

Figure 5.3. Simulated deadbeat controller performance of a 10 A q-axis current step response. Sampled at 5 kHz.

As seen from Figure 5.3, the settling time is approx. 3 sampling periods corresponding to 0.6 ms without any initial overshoot. The average steady state error for the q- and d-axis currents are respectively 1.53 % and 0.31 A. Looking at the d-axis current, an oscillation of approx. 400 Hz is observed. The oscillation is caused by the inverter dead-time which as shown in Section 4.5, generates 6th order harmonics in the d- and q-axis currents.

Concerning the performance of a q-axis current reversal, Figure 5.4 presents the simulated performance of a 10-(-10) A current step reversal.

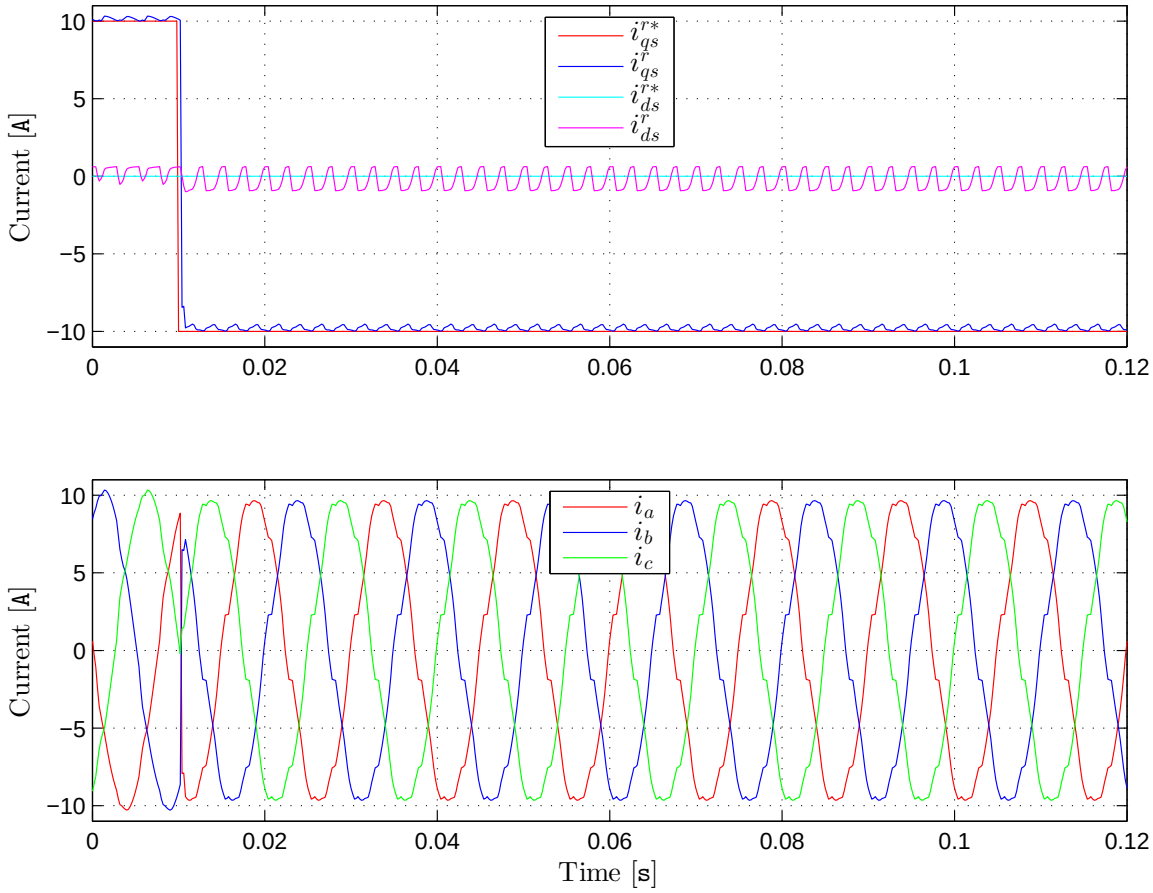

Figure 5.4. Simulated deadbeat controller performance of a -10 A q-axis current step response with an initial current reference of 10 A. Sampled at 5 kHz.

In Figure 5.4 the settling time is approx. 0.6 ms with no overshoot for the q-axis current. The average q- and d-axis steady state errors are in this case respectively 2.14 % and 0.29 A.

Concerning the performance of the predictive deadbeat controller in a case where both q- and d-axis currents are desired, such as in flux weakening, Figure 5.5 presents the performance of a -5 A d-axis current step command while the q-axis current is maintained at 10 A.

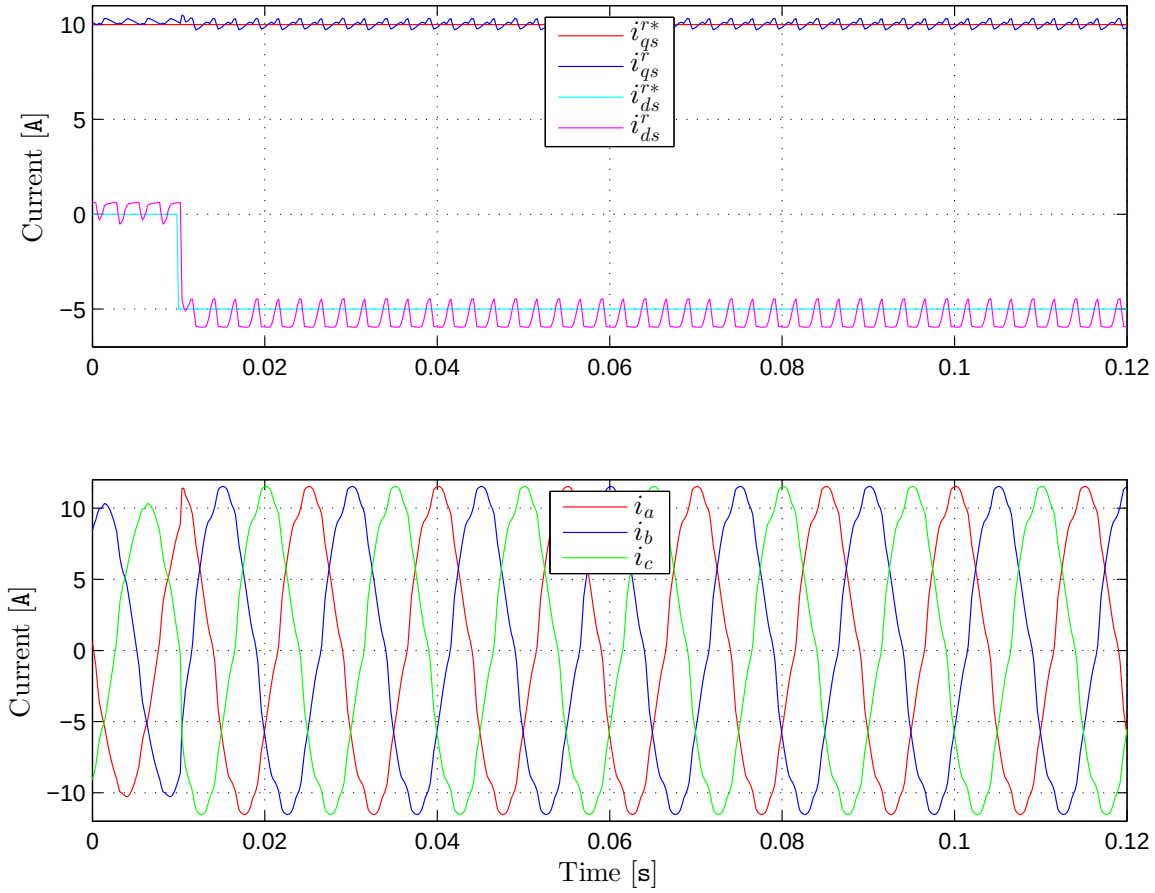

Figure 5.5. Simulated deadbeat controller performance of a -5 A d-axis current step response while maintaining the q-axis current at 10 A. Sampled at 5 kHz.

From Figure 5.5 the d-axis current settling time is observed to approx. 2 sampling periods, while a persistent oscillation is present. The q-axis response is almost unaffected during the step change. The average q- and d-axis steady state errors are calculated respectively to 2.36 % and 10 %.

As the deadbeat controller do not make use of an integrator to eliminate the steady state error continuously, steady state errors can as shown in this section be expected in the experiments. Observing Figure 5.3 reveals that also prior to any current commands, steady state errors are present. The average q- and d-axis steady state errors in this case are respectively 0.146 A and 0.046 A.

5.3 Performance Comparison

Based on the simulation results obtained for the classical FOC PI current controller and the predictive current deadbeat controller, certain conclusions can be drawn.

Since the FOC PI controller has no dead-time compensation technique, there is observed oscillations in the measured d- and q-axis currents. The oscillations are caused by the inverter dead-time. Since the deadbeat controller utilizes an inverter dead-time compensation technique, the amplitude of the oscillations are as seen decreased.

As expected the PI current controller eliminates the average steady state error, whereas the predicitve deadbeat controller exhibits steady state errors due to the inverter non-linearities. As the deadbeat voltages are calculated based on the model parameters, the settling time and thereby the dynamics are much faster for the deadbeat controller. Therefore, when implementing the deadbeat controller algorithm in the DSP and operating it in the laboratory, it could be expected as the simulations shows that steady state errors and faster dynamics will be seen.

For gaining a further insight into the controller performances Figure 5.6 presents the frequency spectrum of the phase a machine current. This frequency spectrum is obtained in steady state for $i_{ds}^{r*} = 0$ A and $i_{qs}^{r*} = 10$ A for respectively the FOC PI controller and the predictive deadbeat controller.

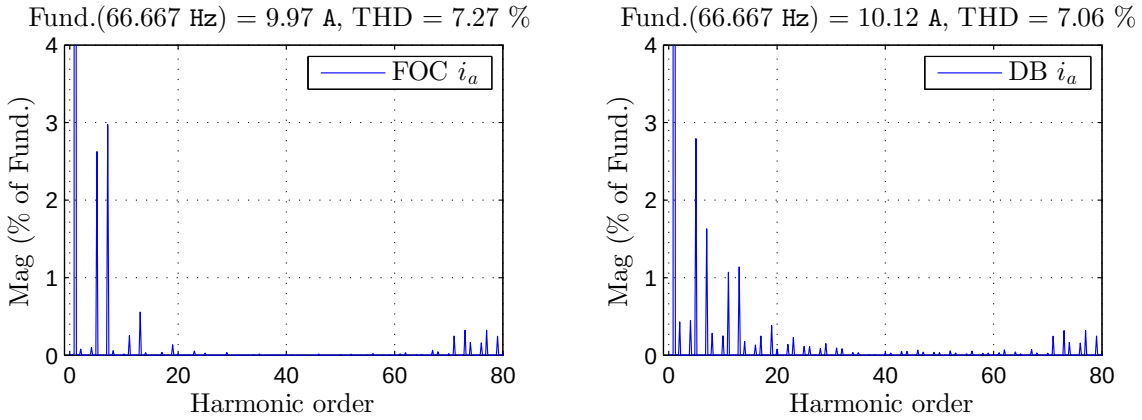

Figure 5.6. Frequency spectrum of the simulated phase a machine current. Left: PI Control, Right: Deadbeat Control.

As seen from Figure 5.6 the THD level of the phase current is for the deadbeat controller is 0.21 % lower than that of the PI controller. The improvement is caused by the dead-time compensation technique implemented in the deadbeat controller, that as seen decreases the 5th and 7th order harmonics. Figure 5.7 presents the simulated frequency spectrum of the torque current i_{qs}^{r}, for the same conditions.

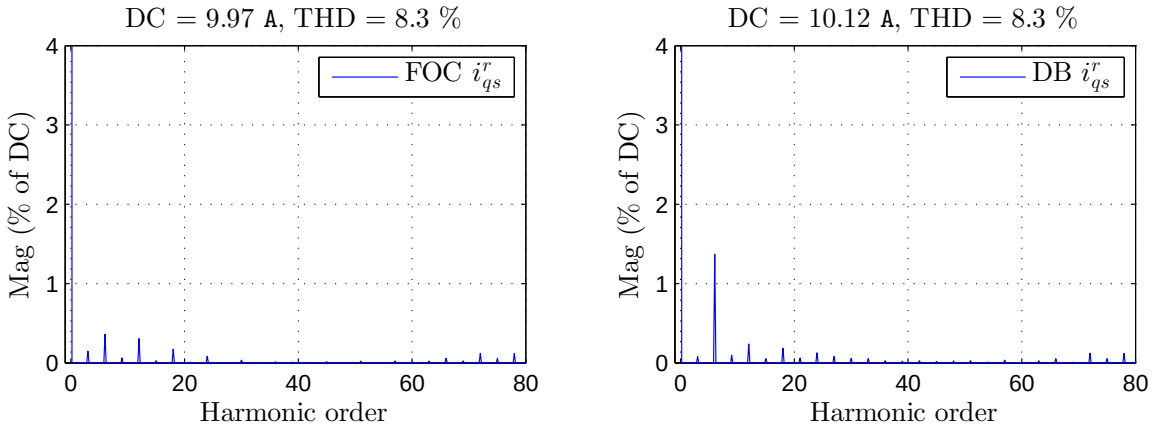

Figure 5.7. Frequency spectrum of the simulated torque current i_{qs}^{r}. Left: PI Control, Right: Deadbeat Control.

From Figure 5.7 it is seen that the THD levels are similar for both controllers. Based on the frequency spectrum of the simulated machine currents the performance of the deadbeat controller can be expected to overcome the experimental performance of the FOC PI controller as the practical non-linearities of the inverter are even more significant. This means that the torque current is improved by the predictive deadbeat controller.

Chapter 6
Experimental Results

This chapter is dedicated to analysis of the acquired experimental results. The experimental results are obtained using two developed dSPACE models; one for the classical FOC PI current controller, and one for the predictive deadbeat controller.

The dSPACE results are used to verify the simulation results, and to verify the experimental functionality of the controllers. Once a result is presented, the settling time, overshoot, and steady state error are given. The extracted information is used to compare the experimental performance of the controllers.

The experimental results are obtained under equal conditions in order to properly compare the experimental controller performances, and to compare with the simulation results. The conditions are listed as follows:

- The predictive deadbeat controller is based on the parameters in Table 2.1 and implemented according to Chapter 4.
- The FOC PI controller parameters are $K_{pc} = 2.7$ and $K_{ic} = 1000$.
- The stator voltage vector is phase shifted by $1.5T_s\omega_r(k)$ due to position sampling delay.

In the experimental work, the FOC PI controller performance is tested by both d- and q-axis step commands. Specifically, a 0-10 `A` q-axis step change and a 10-(-10) `A` q-axis step reversal both at zero d-axis current. The same two steps are applied for the d-axis with zero q-axis current.

The deadbeat controller testing is extended compared to the PI controller in order to verify the performance improvements introduced by the dead-time compensation and current prediction techniques. Therefore, the conventional deadbeat controller is first tested, followed by the inclusion of the dead-time compensation. Next, the current prediction improvement is demonstrated. Finally, the complete proposed predictive deadbeat controller is tested. All tests of the deadbeat controller are attempted with the same step tests as the FOC PI controller. As in the simulations a -5 `A` d-axis current step change at $i_{qs}^r = 10$ `A` is also performed.

A q-axis current step corresponds to a step in electromagnetic torque while the d-axis current command controls the magnetic flux in the machine. As in the simulations, the tests are performed at a constant shaft speed of 1000 $\texttt{min}^{-1}$ by operating the IM in speed control mode.

6.1 PI Control

This section contains the experimental results obtained for the classical PI current controller found in Chapter 3. The measurement obtained for a 10 `A` q-axis current step command is presented in Figure 6.1.

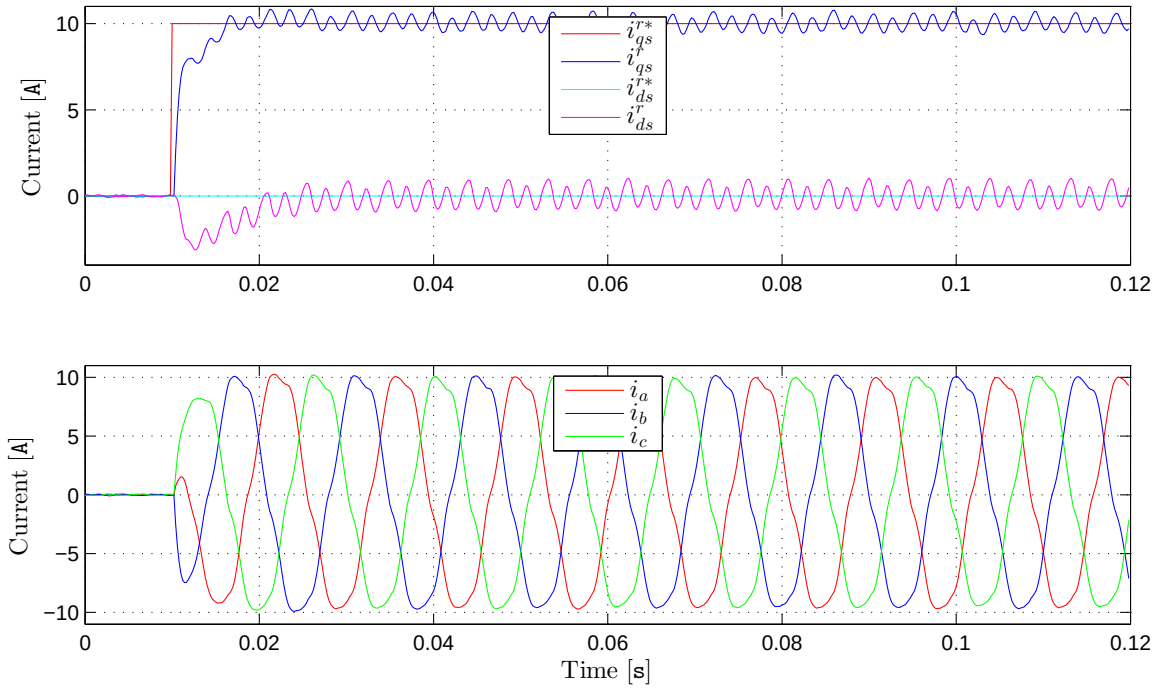

Figure 6.1. Performance of a 10 A q-axis current step response.

Observed from Figure 6.1 is a settling time of 5.4 ms with approx. 2 % overshoot, and an average steady state error of 0 %. A low amplitude oscillation is observed in steady state for both the q-axis and the d-axis currents.

In Figure 6.2 the measurement of a 10-(-10) A q-axis current step is shown.

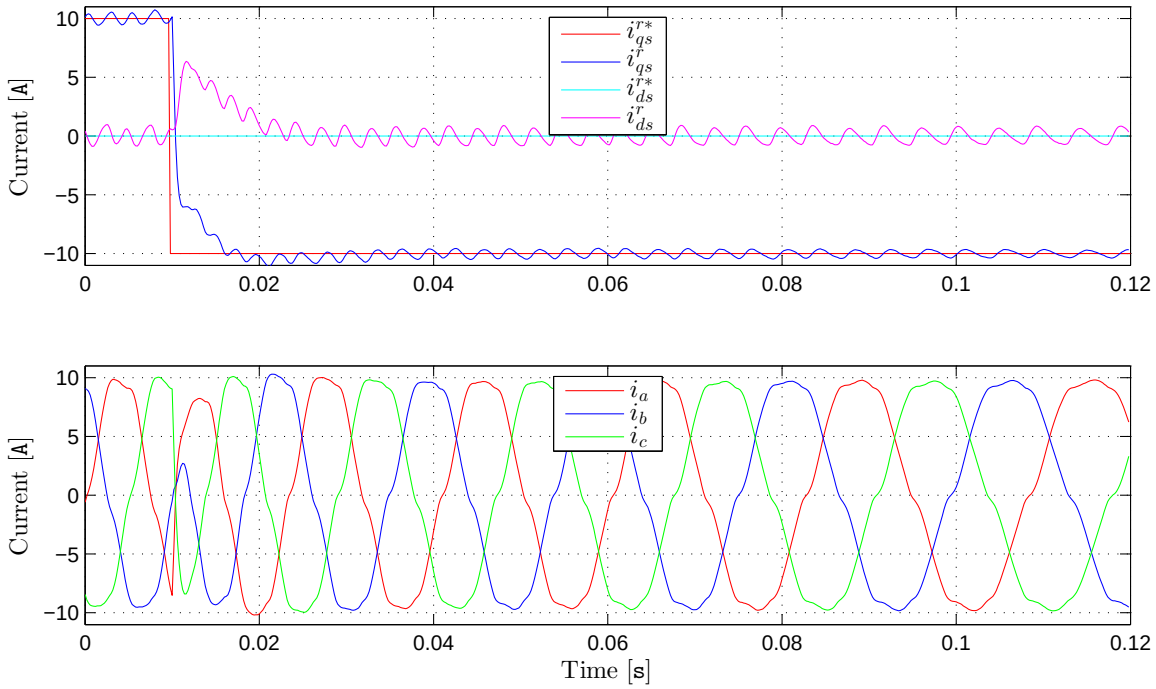

Figure 6.2. Performance of a -10 A q-axis current step command when the initial current is 10 A.

Figure 6.2 reveals similar characteristics as Figure 6.1. Again a low amplitude oscillation is observed. A small overshoot of approx. 2 %, and a settling time of approx. 5.5 ms is seen. The average steady state error is eliminated. Figure 6.3 presents the measurement of a 10 A d-axis current reference step

command.

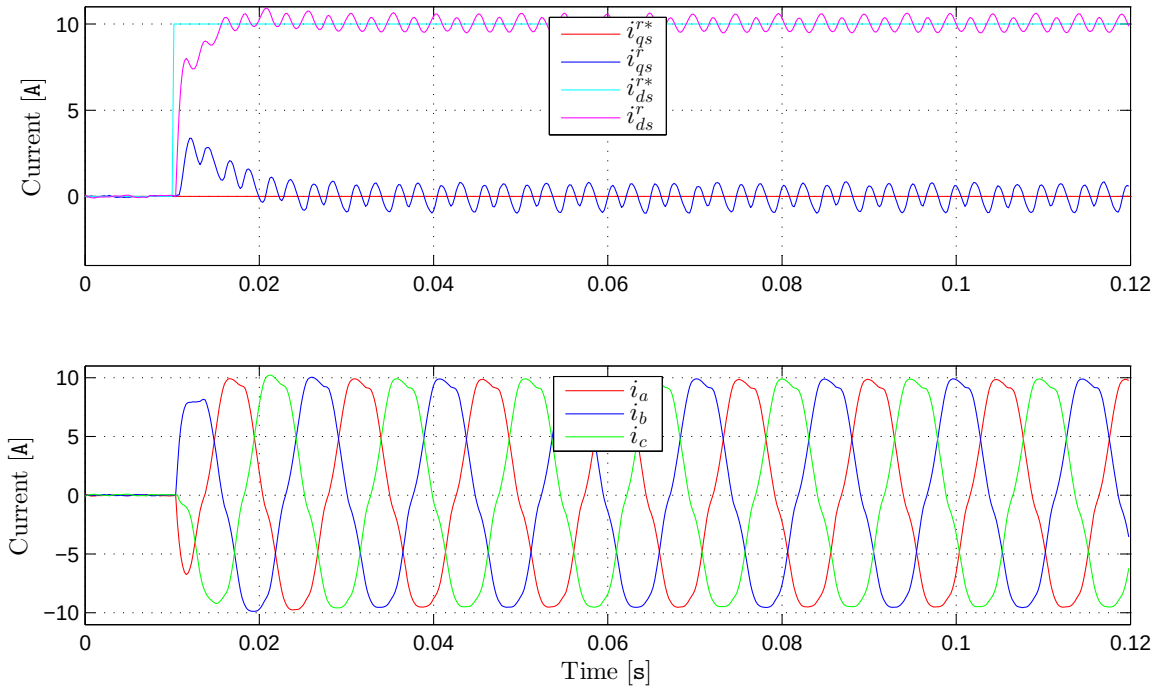

Figure 6.3. Performance of a 10 A d-axis current step response.

As seen in Figure 6.3 a similar response as for the q-axis current is obtained, with a settling time of approx. 4.9 ms, a small overshoot of approx. 2 %, and an average steady state error of 0 % for the d-axis current.

The measurement presented in Figure 6.4 constitute a d-axis current step command reversal from 10 A to -10 A.

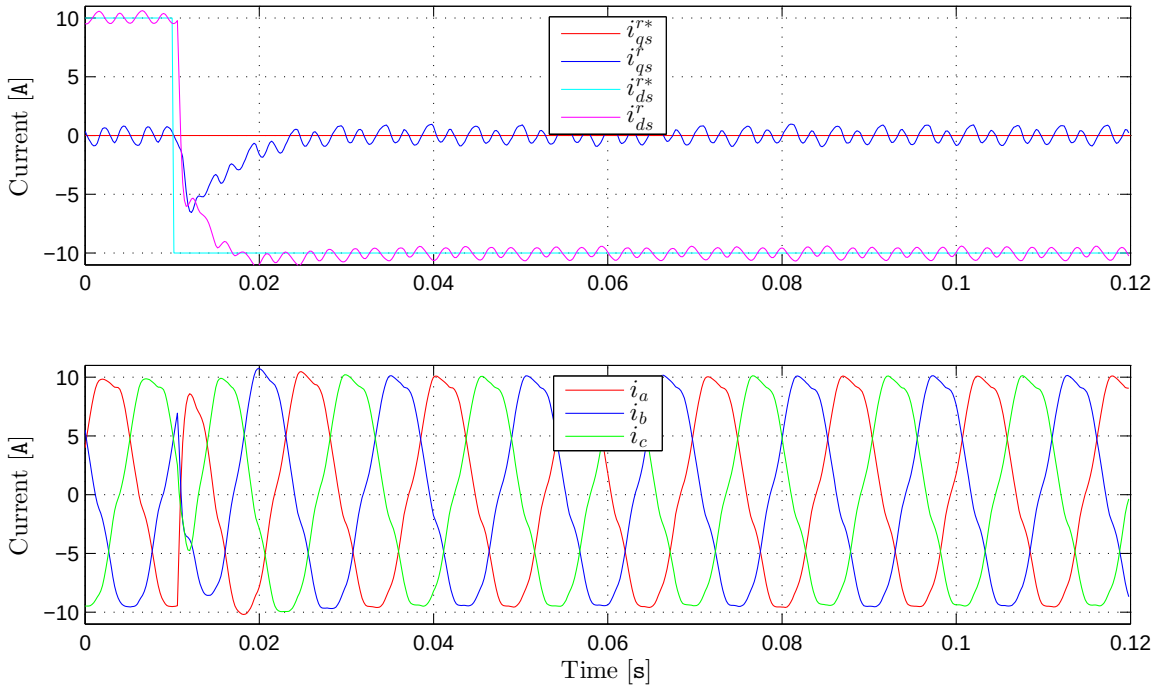

Figure 6.4. Performance of a -10 A d-axis current step command when the initial current is 10 A.

From Figure 6.4, a settling time of approx. 10 ms with a small overshoot of approx. 3 %, and an

average steady state error of 0 % for the d-axis current is observed.

As the d- and q voltages are coupled, as seen from (2.12) and (2.13), a change in the d-axis current occur when the q-axis current change is changed and vice versa. This behaviour is present in all the measurements in this section. As the PI controller eliminates the error continuously, the desired currents are reached independently, with similar characteristics as the d- and q-axis controllers are identical.

The steady state oscillations observed for both current loops, causes as seen distortion of the stationary three phase currents. The oscillations observed have a frequency of approx. 400 `Hz`, which corresponds to the sixth-harmonic frequency in the synchronous rotating dq reference frame. The oscillations are introduced by the inverter non-linearities, as explained in Section 4.5. By properly compensating the inverter voltage error, the amplitude of the sixth harmonic component can be decreased. [Hwang and Kim, 2010]

6.2 Predictive Deadbeat Control

This section presents the measurements obtained for the developed predictive deadbeat controller based on the theory in Chapter 4. First, measurements of the conventional deadbeat controller in Section 4.2 are presented. Second, the measurements of the dead-time compensated deadbeat controller are presented. Third, the measurements of the predictive current delay compensated deadbeat controller are presented. Last, the performance of the proposed predictive deadbeat controller is presented.

6.2.1 Deadbeat Control

The results contained in this section is obtained based on the deadbeat voltages presented in (4.4) and (4.5). Figure 6.5 presents the measurements obtained for a q-axis current step command of 5 `A`.

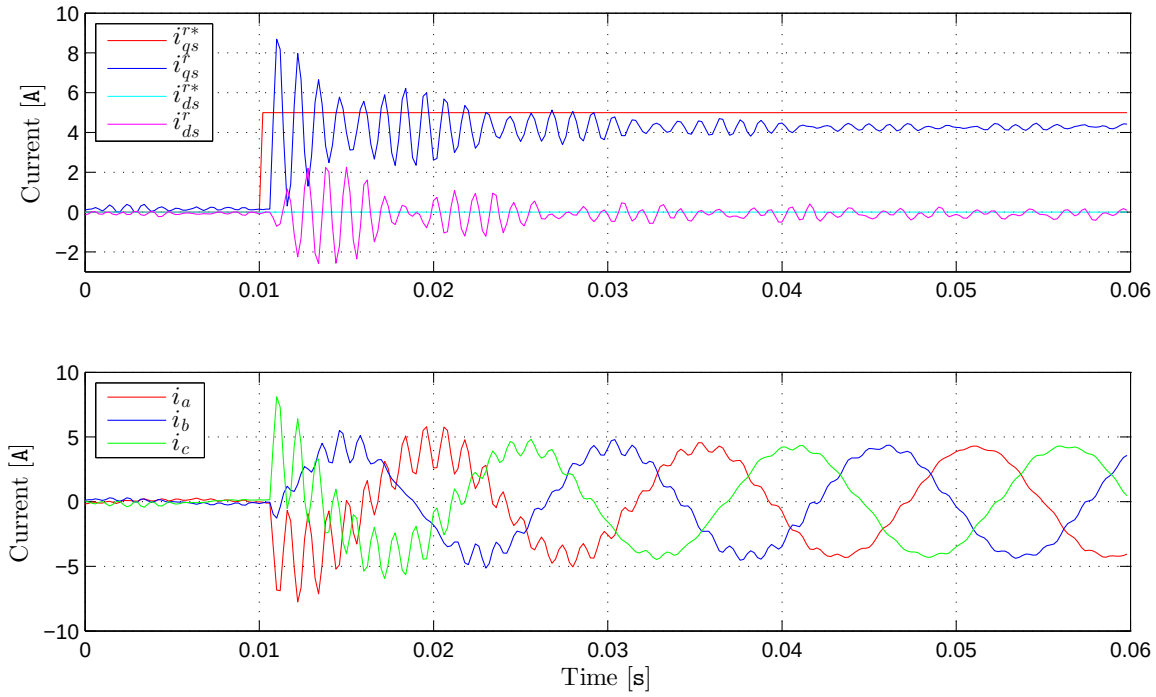

Figure 6.5. Performance of a 5 `A` q-axis current step response.

According to Figure 6.5 the q-axis current exhibits an oscillation that initially produces an overshoot of 73.8 %. At $t = 0.05$ `s` steady state is reached with a continuous low amplitude oscillation. The

settling time is 19.2 ms, while the final steady state value produces a steady state error of 14.87 %, which is large for a closed loop system. The average steady state d-axis current error is 0.1 A. Figure 6.6 presents the measurement of a 5-(-5) A q-axis current step change.

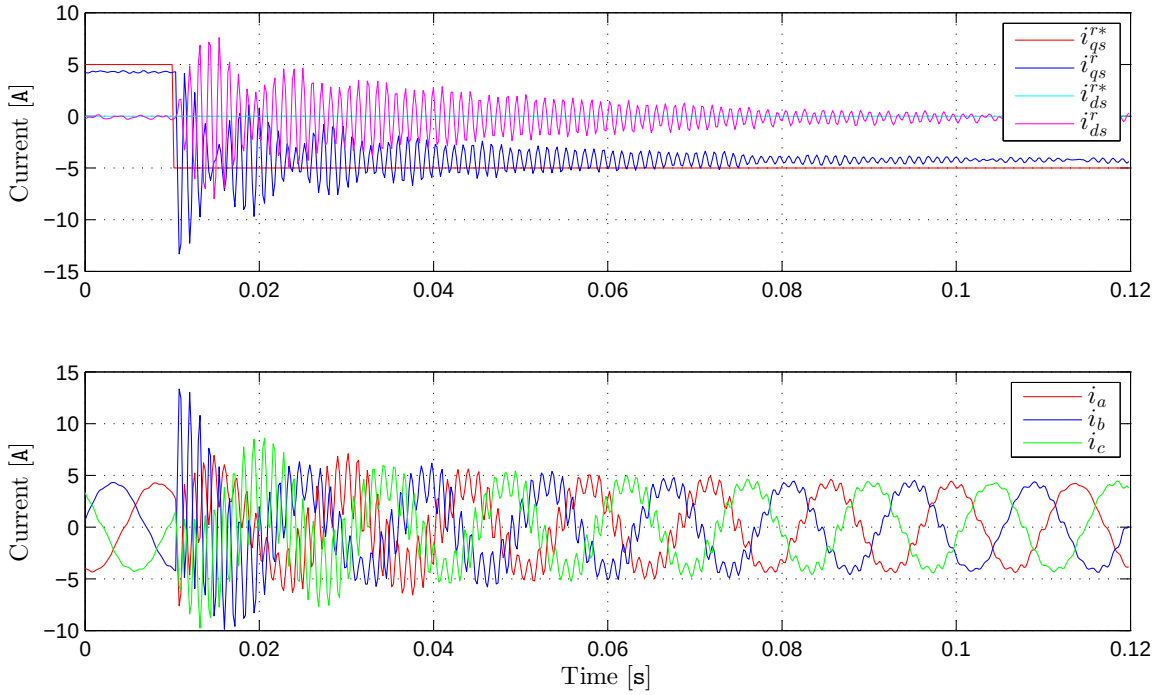

Figure 6.6. Performance of a -5 A q-axis current step command when the initial current is 5 A.

Again as shown in Figure 6.6, a large initial overshoot of 266.2 % is observed when the q-axis reference is stepped from 5 A to -5 A. The settling time is 49 ms, while the final steady state error is 15.1 %. The average d-axis current steady state error is 0.12 A.

The amplitude of the q-axis current step references are shown only for 5 A to -5 A as the oscillations observed for higher step changes caused triggering of the build-in hardware protections, which are based on the system parameters shown in Table 2.1.

It can be concluded based on the measurements shown in Figure 6.5 and 6.6 that the system is close to marginal stability when utilizing the conventional deadbeat controller. The observed oscillations are unacceptable in a high performance closed loop drive system. The oscillations are caused by the calculation of the deadbeat voltages using (4.4) and (4.5) as they do not take into account the system delays. The steady state errors which are approx. 15% are likewise undesired in a closed loop system. The observed steady state errors are possibly explained by the non-linearities of the inverter.

6.2.2 Deadbeat Control with Dead-time Compensation

In this section, the conventional deadbeat control voltages are modified by the addition of the dead-time technique found in Section 4.5. The addition can possibly improve the steady state accuracy. Figure 6.7 presents the performance of the deadbeat controllers when the dead-time compensation is added for a q-axis current step change of 5 A.

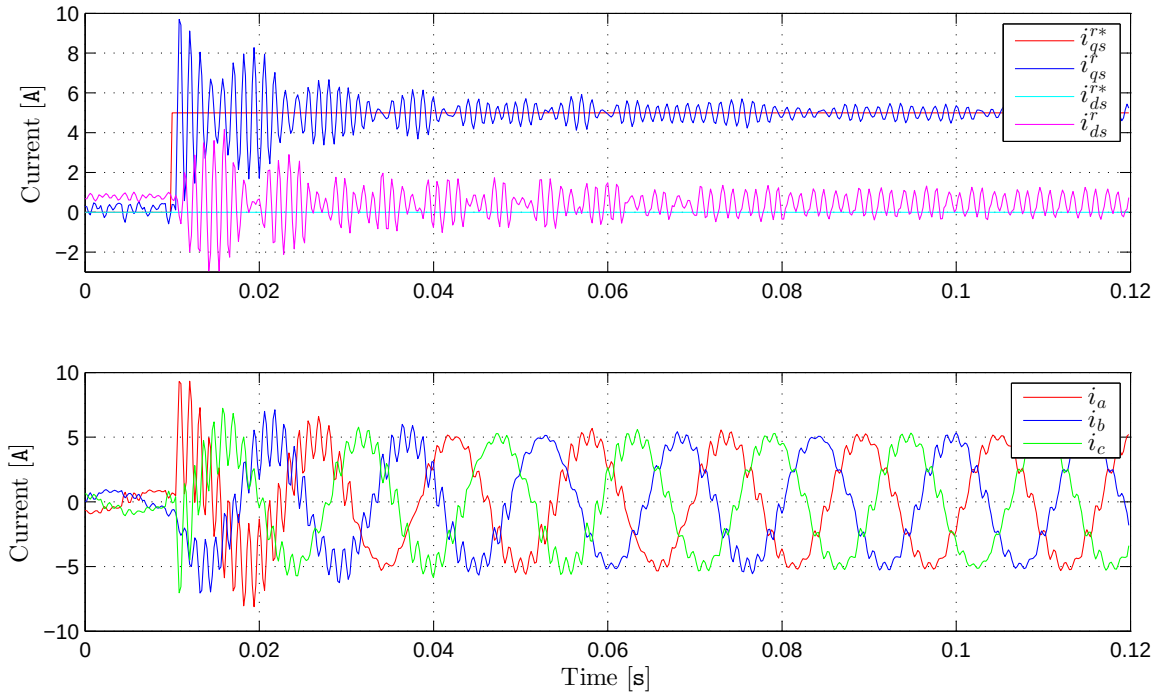

Figure 6.7. Performance of a 5 A q-axis current step response including dead-time compensation.

From Figure 6.7 a large initial overshoot of 94 % and a persistent oscillation is observed. The settling time is 29 ms, while the average q-axis steady state error in this case is reduced to 0.2 % when the dead-time compensation voltages are added. The average d-axis current error is 0.44 A.

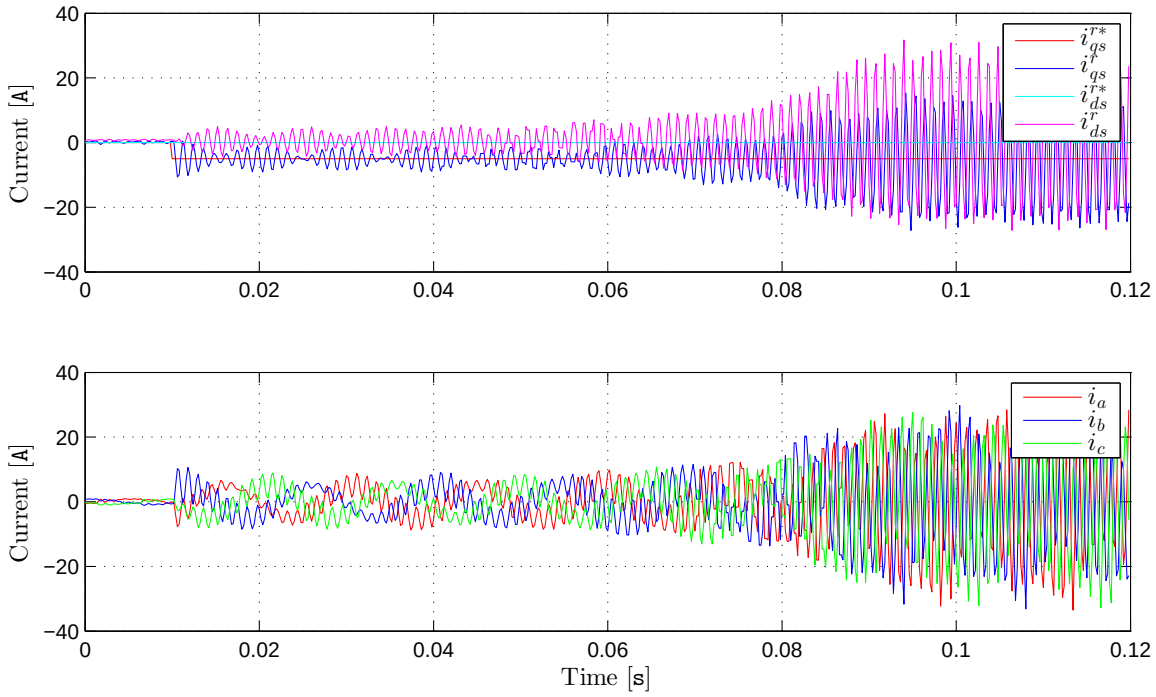

Figure 6.8. Performance of a -5 A q-axis current step response when the dead-time compensation technique is added.

Figure 6.8 presents the performance of the deadbeat controller when the dead-time compensation is added for a q-axis current step change of -5 A. The performance in this case is very poor, and the hardware protections are triggered very quickly. The observed oscillations starts to continuously increase in amplitude after approx. 0.05 s which implies that the system for a negative step change

of -5 A is unstable.

The improved steady state accuracy as seen in Figure 6.7 when adding the dead-time compensation voltages implies that the inverter dead-time is the primary explanation for the poor steady state accuracy. Another source of steady state accuracy is that the deadbeat voltages are calculated based on the experimentally determined machine parameters. The parameters are, as explained in Chapter 7, non-linear due to their operation point dependency. Their variation can cause the deadbeat algorithm to calculate slightly wrong deadbeat voltages which do not reach steady state precisely.

6.2.3 Predictive Current Deadbeat Control

The measurements contained in this section are obtained based on the deadbeat control voltages presented in (4.6) and (4.7) which incorporates the DSP signal delay compensation by using the current predictor. Figure 6.9 presents the performance of a 0-10 A q-axis current step change.

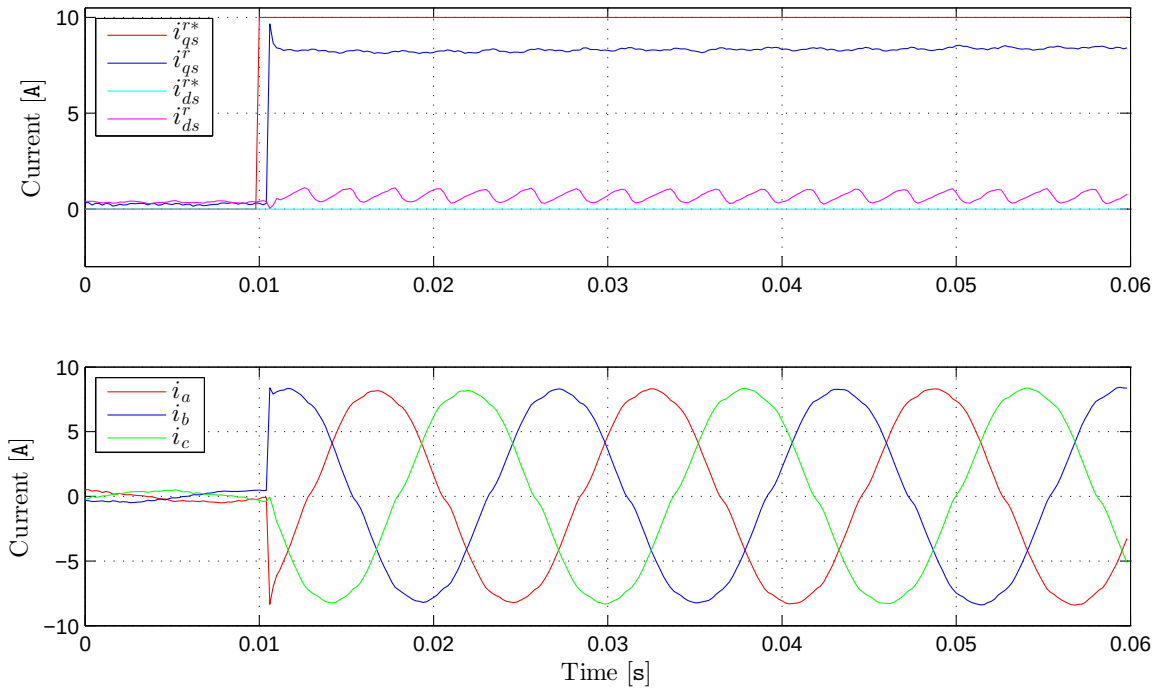

Figure 6.9. Performance of a 10 A q-axis current step when utilizing the current predictor.

As can be seen from Figure 6.9, the transient period is much improved compared to the conventional deadbeat controller. After 3.5 sampling periods corresponding to 0.7 ms the controller has settled at a steady state value of 8.41 A, which produces an error of 15.9 %. A 15 % overshoot is observed initially. The average steady state d-axis current error is 0.71 A.

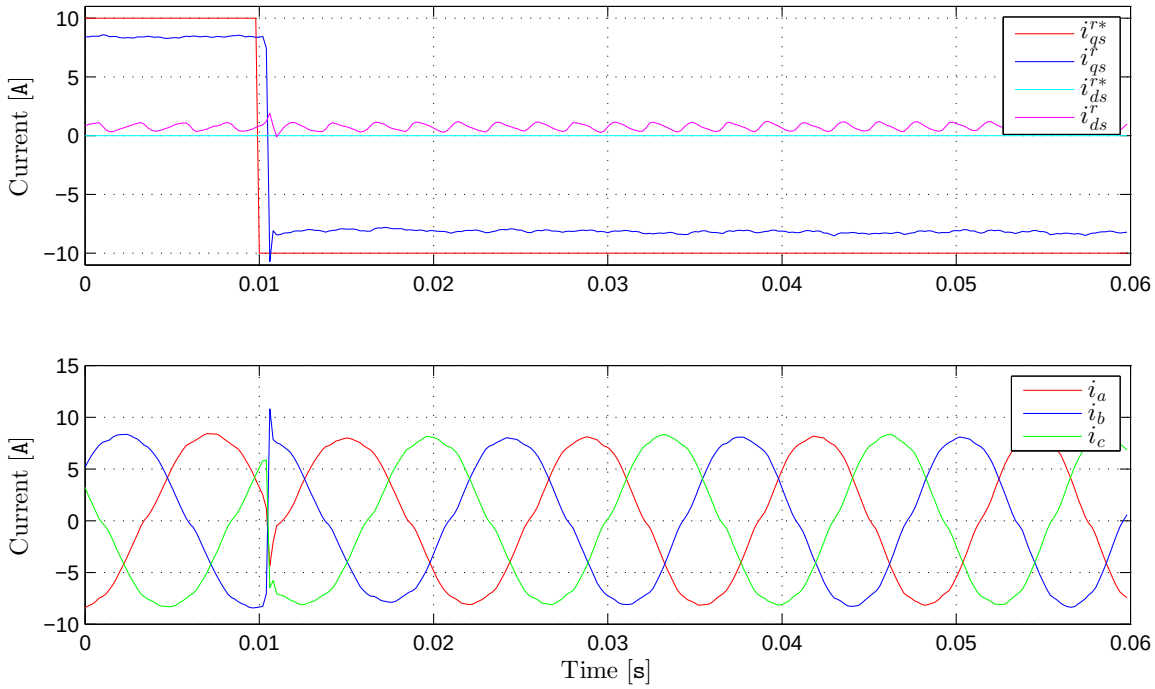

Figure 6.10. Performance of a -10 A q-axis current step response when utilizing the current predictor with an initial current reference of 10 A.

Figure 6.10, which shows the performance of a negative -10 A step change when the initial reference is 10 A, reveals a steady state error of 16.2 % and again a small initial overshoot. The settling time is again observed to 3.5 sampling periods corresponding to 0.7 ms. The average steady state d-axis current error is 0.62 A.

Based on Figure 6.9 and 6.10 the improvement of the current prediction is clearly observed. The steady state accuracy can as shown in the previous section be compensated for by adding the dead-time compensation voltages to the deadbeat voltages.

6.2.4 Predictive Current Deadbeat Control with Dead-time Compensation

This section contains the results obtained based on the deadbeat voltages presented in (4.6) and (4.7) with the addition of the dead-time compensation technique found in Section 4.5, hence both the DSP signal delay and the inverter dead-time are compensated for.

Since this controller is the outcome of Chapter 4, and the controller with the best performance, this section contains further measurements as they are essential for mapping out the experimental performance of the controller. In Figure 6.11 the measurement of a 0-10 A q-axis current step is shown.

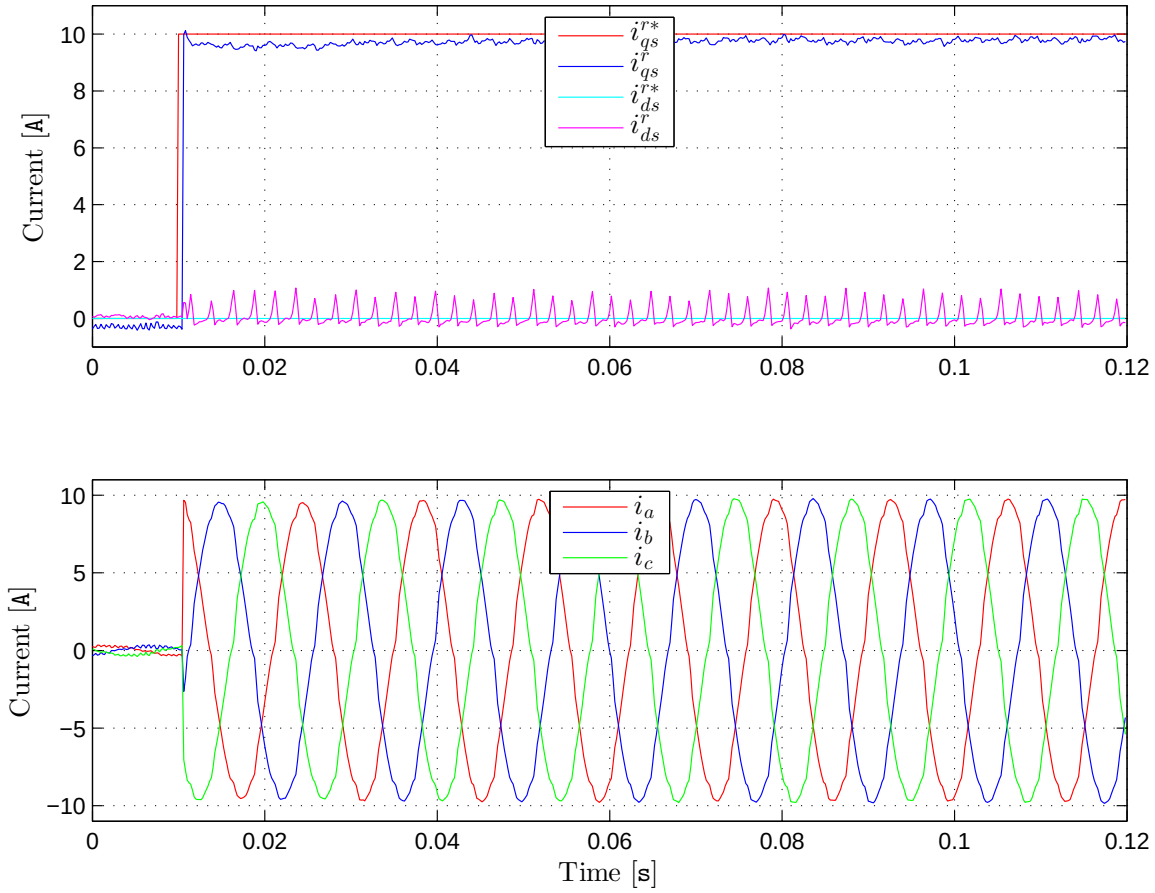

Figure 6.11. Performance of a 10 A q-axis current step response when utilizing the current predictor and the dead-time compensation technique.

In Figure 6.11 an initial overshoot of 1.2 % is observed, the settling time is approx. 3 sampling periods, and the final steady state value results in a steady state error of 2.1 %. The average steady state d-axis current error is 0.03 A. The d-axis current contains as seen a 400-450 Hz component corresponding to the 6-7th order harmonic component. This behaviour reflects the non-linearities of the inverter as the error voltage is operation point dependent, hence it might produce other frequencies in the output voltages.

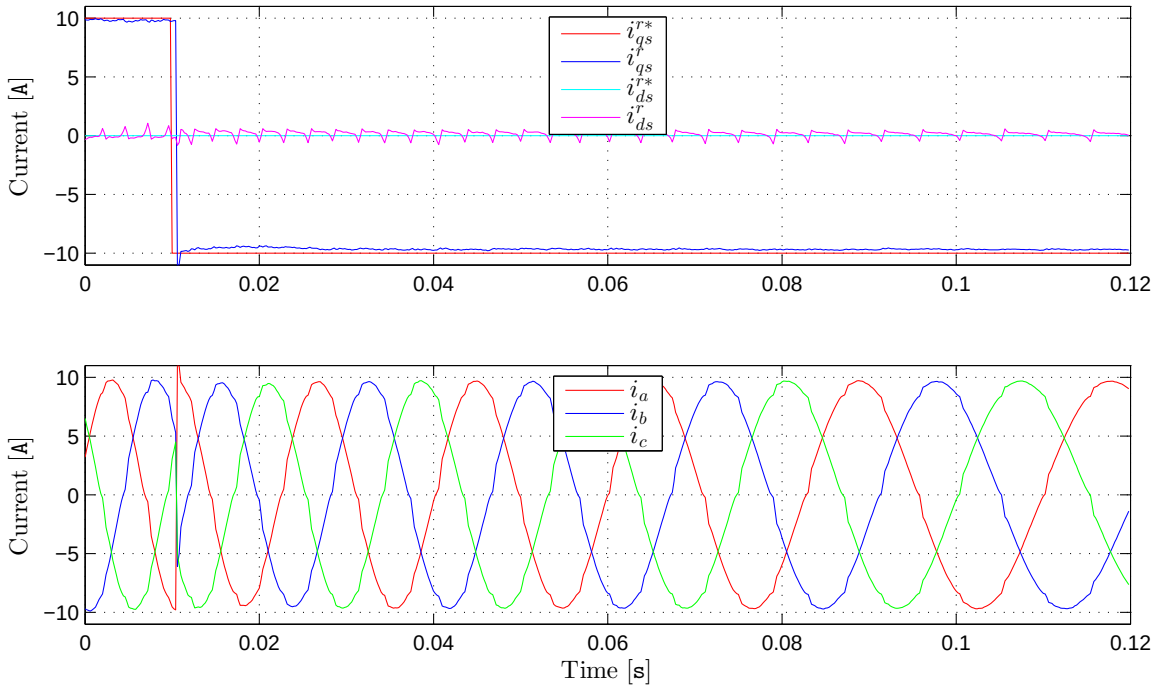

Figure 6.12. Performance of a -10 A q-axis current step response when utilizing the current predictor and the dead-time compensation technique with an initial current reference of 10 A.

Figure 6.12, which shows the performance of a negative 10-(-10) A step change, reveals a steady state error of 1 % and an initial overshoot of 11.5 %. The settling time is observed to approx. 4 sampling periods corresponding to 0.8 ms. The average steady state d-axis current error is 0.15 A. Also observed is that the frequency of the current decreases after the current reversal command. This is caused by the PMSM torque reversal, which affects the controlled IM speed. If the measurement is observed until 0.5 s, the frequency is restored to 66.66 Hz by the IM speed controller.

In order to map the performance of independent direct- and quadrature axis current control, Figure 6.13 presents the measurement of a solely 10 A d-axis current step command.

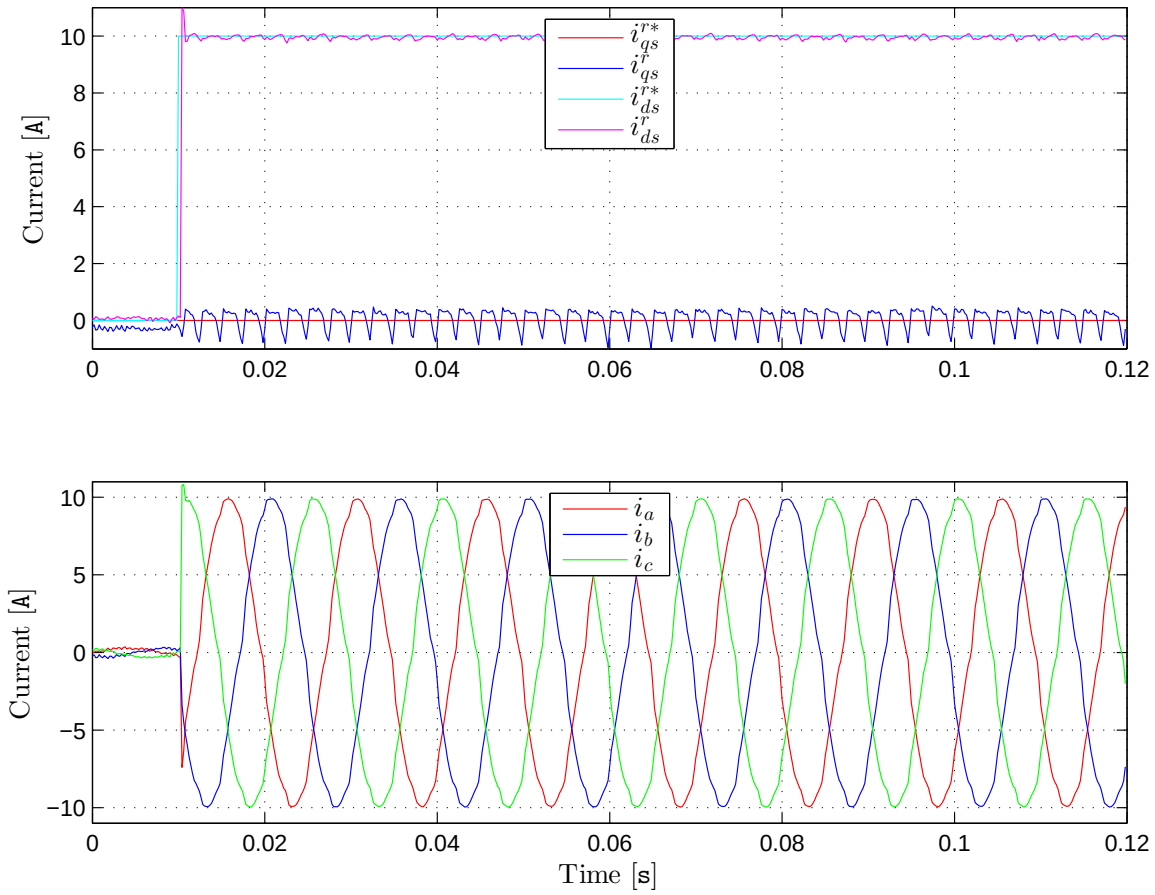

Figure 6.13. Performance of a 10 A d-axis current step response when utilizing the current predictor and the dead-time compensation technique.

From Figure 6.13 an initial overshoot of 10.2 % is observed. The steady state error in this scenario is 0.4 %, while the settling time is 4 sampling periods. The average steady state q-axis current error is 0.07 A. As seen the q-axis current ripple is increased compared to Figure 6.11. This is caused by the dead-time compensation technique which changes the compensation voltage shape, when the desired current vector argument changes as shown in Figure 4.8. This improves the current ripple of the desired current to be controlled.

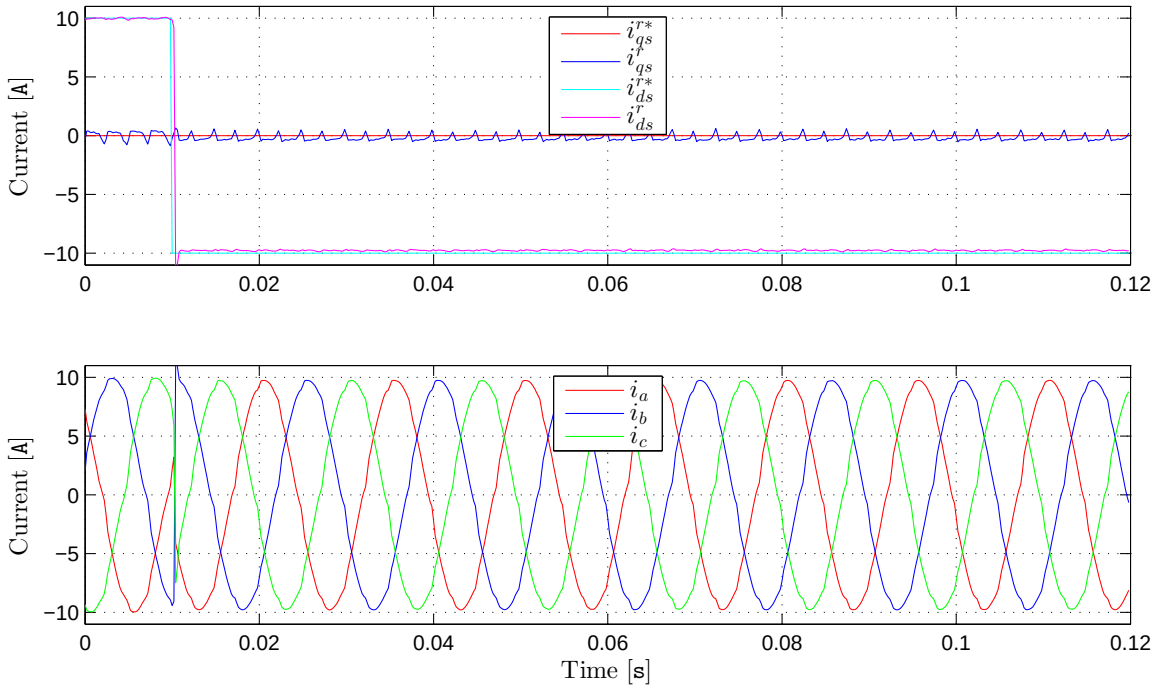

Figure 6.14. Performance of a -10 A *d*-axis current step response when utilizing the current predictor and the dead-time compensation technique with an initial current reference of 10 A.

The measurement presented in Figure 6.14 constitute a *d*-axis current step command reversal from 10 A to -10 A. The *d*-axis current response produces an initial overshoot of 10.2 %, a steady state error of 1.8 % and a settling time of approx. 4 sampling periods. The average steady state *q*-axis current error is 0.23 A.

Concerning the accuracy in a scenario where non-zero direct- and quadrature axis currents are required the response shown in Figure 6.15 presents the performance of a -5 A *d*-axis step change when the *q*-axis current is 10 A.

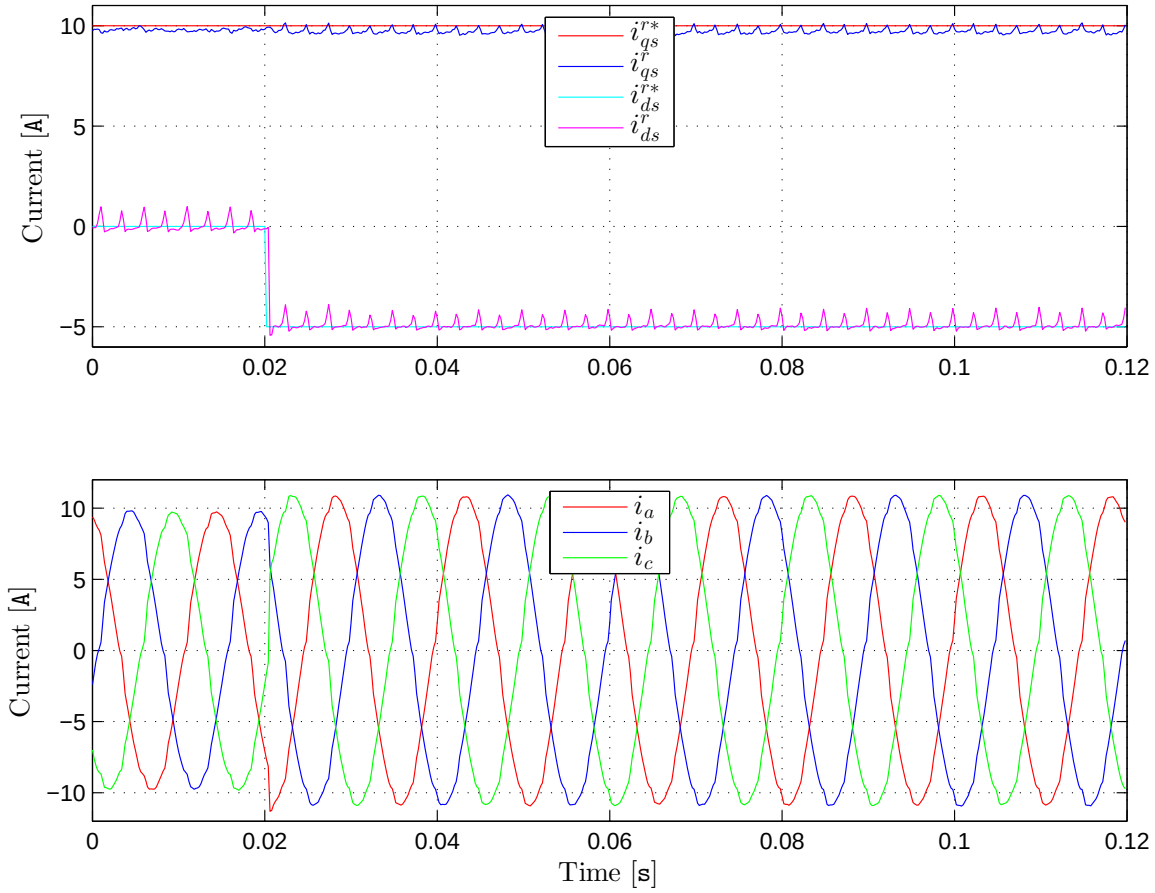

Figure 6.15. Performance of a -5 A d-axis current step response when utilizing the current predictor and the dead-time compensation technique with a q-axis current reference of 10 A.

As shown in Figure 6.15 a settling time of 4 sampling periods and a d-axis average steady state error of 1.2 % is present. The q-axis steady state error is increased from 1.2 % to 2.7 % after the d-axis step.

Since the signal variables, i.e. the measured currents and rotor position, are accurate only at the sampling intervals and change dynamically between the sampling intervals, a prediction error when applying a step command can occur i.e. an initial overshoot can be expected as is also seen from the results. The significance of the error caused by this phenomenon is relatively small compared to the model parameter accuracy, as it is much more dominant for the dynamic performance.

Regarding the measurements of the predictive deadbeat controller, the average steady state error was seen to be around 0-3 %. In the experimental work, to eliminate the errors and evaluate the performance, a d- and q-axis voltage was therefore either subtracted or added to the deadbeat voltages using the developed dSPACE Control Desk model. Table 6.1 shows the added or subtracted d- and q-axis voltages required to reach the desired steady state values for several scenarios.

Table 6.1. Voltages added to d- and q-axis voltage references to reach desired steady state currents.

i_{ds}^{r*} [A]	i_{qs}^{r*} [A]	$\pm v_{ds}^{r}$[V]	$\pm v_{qs}^{r}$ [V]
0	0	-1.3	3.1
0	10	-1.9	1
0	-10	0.3	-0.8
-5	10	-2.2	0.4

The voltage biases shown in Table 6.1 are highly likely caused by non considered inverter non-linearities and possibly model parameter mismatches. The amount of additional voltage added or subtracted, will decrease if the steady state accuracy is improved by modification of the deadbeat algorithm. As seen in Figure 6.11 and in the top row of Table 6.1, the measured currents were not zero with the current references set to zero.

In the experimental work, it was found that the addition of the dead-time compensation voltages in this case resulted in an increased PMSM power flow. Therefore the dead-time compensation technique was disabled in the experimental work when $i_{ds}^{r*} = 0$ `A` and $i_{qs}^{r*} = 0$ `A`.

6.3 Performance Comparison

Based on the data presented in this chapter, it is clear that the performance of the predictive current deadbeat controller with dead-time compensation has a proper functionality compared to the non-modified deadbeat controller. Comparing the PI controller with the proposed predictive deadbeat controller, reveals that the transient occurring under a q-axis current step change, is improved significantly. The settling time decreases from approx. 5 `ms` using the PI controller to approx. 0.7 `ms` utilizing the deadbeat controller. Furthermore, as the electromagnetic torque is a product of the q-axis current, it was seen to improve when using the predictive deadbeat controller. The current prediction together with the dead-time compensation removed the persistent oscillations, and improved the accuracy significantly. The predicitve deadbeat control method suffers from small steady state errors which are not eliminated over time. This is caused by its dependency on model parameters and non considered inverter non-linearities.

Again for gaining a further insight into the experimental controller performances Figure 6.16 presents the dSPACE 5 `Khz` sampled frequency spectrum of the phase a machine current. The frequency spectrum is obtained in steady state for $i_{ds}^{r*} = 0$ `A` and $i_{qs}^{r*} = 10$ `A` for respectively the PI controller and the predictive deadbeat controller.

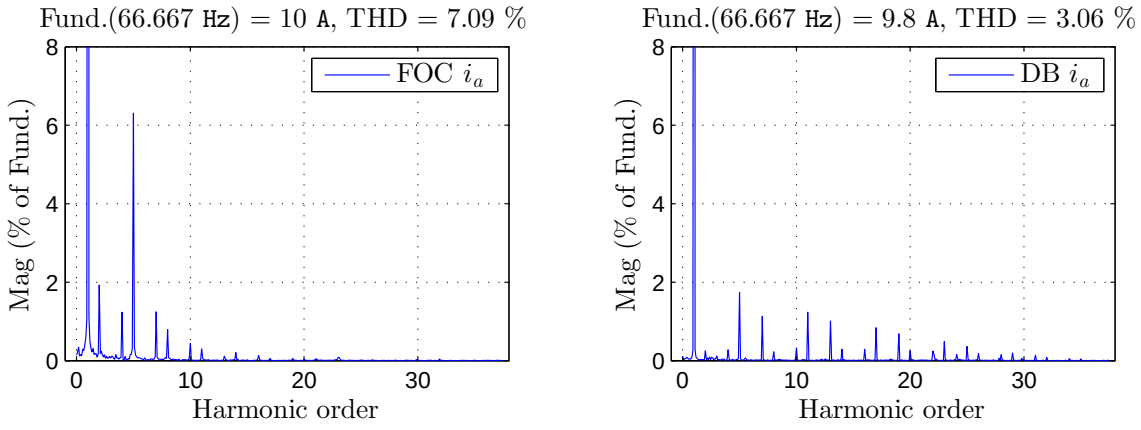

Figure 6.16. Frequency spectrum of the experimental 5 `kHz` sampled phase a machine current. Left: PI Control, Right: Deadbeat Control.

As seen from Figure 6.16 the amplitude of the 5th order current harmonic is significant for the FOC PI controller current as the inverter non-linearities are not properly compensated. The frequency spectrum obtained for the deadbeat controlled system reveals that the dead-time compensation technique functions properly, decreasing the amplitude of the 5th order harmonic from 6.2 % for to PI controller to 1.8 % and therefore improves the dynamic response and THD level of the machine current. Figure 6.17 presents the frequency spectrum of the experimental torque current i_{qs}^{r} under the same conditions.

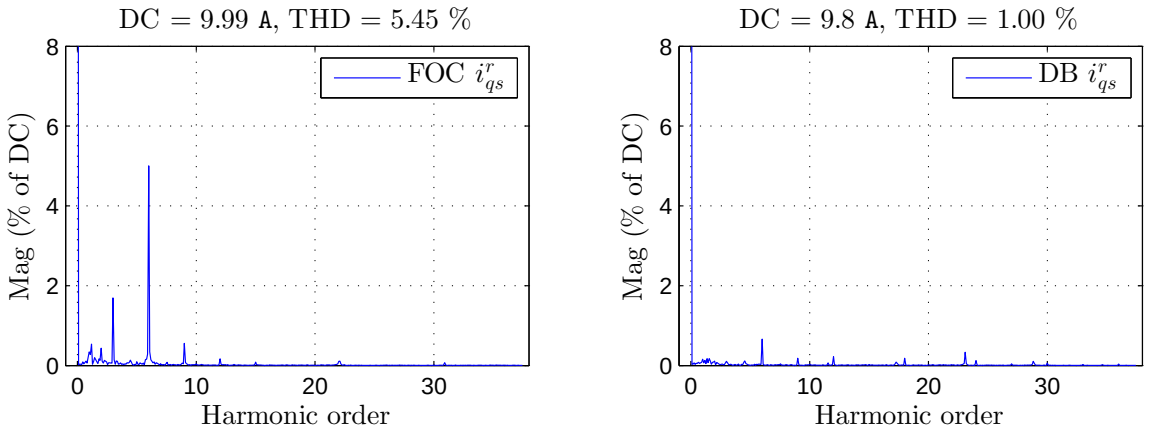

Figure 6.17. Frequency spectrum of the experimental 5 kHz sampled torque current i_{qs}^r. Left: PI Control, Right: Deadbeat Control.

As expected, the amplitude of the 6th order harmonic, introduced by the inverter non-linearities, is decreased for the deadbeat controller improving the THD level and thereby the dynamic machine performance. The spectral analysis is based on the 5 kHz sampled dSPACE measurements. Using an oscilloscope measurement would more precisely indicate the THD level as the 5 kHz switching frequency is not present in the dSPACE signals. In order to include the switching frequency the dSPACE sampling frequency should be increased to at least 10 kHz according to the Nyquist criteria to avoid aliasing. Since the switching frequency is not considered dominant for the performance, the measurements acquired using dSPACE are considered sufficient, as the demonstration of the dead-time compensation is seen using dSPACE.

Chapter 7
Parameter Sensitivity

Utilizing deadbeat control for controlling the PMSM currents, requires a precise machine model since the deadbeat voltage are calculated based on the model parameters. Considering the that parameters may vary due to temperature changes or machine saturation, or that a precise measurement of the parameters are difficult to acquire due to the non-linear nature of the electrical machine, it is important to evaluate and map how the deadbeat controllers perform in the presence of such model parameter errors. This chapter evaluates and maps, based on the simulation models, the performance of the traditional PI current controller and the predictive current deadbeat controller when parameter errors are present.

The results obtained in this chapter are based partly on the two simulation models, one using the FOC PI current controller and the other using the predictive deadbeat controller. Both models make use of a non-linear inverter model with a 2.5 μs dead-time. For evaluating the performance, the PMSM is sped up to 1000 $\mathtt{min}^{-1}$, and the d- and q-axis current references are respectively commanded to $i_{ds}^r = 0$ A and $i_{qs}^r = 10$ A. The sampling time of the Simulink controller sub-system, and the inverter switching frequency is 5 kHz to imitate the experimental conditions.

Furthermore, this chapter contains experimental results which are obtained under deadbeat algorithm parameter errors. These results are incorporated as an important section regarding the controller sensitivity.

7.1 Parameter Errors

To analyse the influence of parameter errors, some criteria must be set up for evaluating the performance. The resistance of the cobber windings in the stator, varies with temperature according to (7.1)

$$R_{ph} = R_{ph0}\left(1 + \alpha(T_{amb} - T_{ref})\right) \quad [\Omega] \tag{7.1}$$

where:
α is the temperature coefficient of cobber. $\alpha = 0.003862$ $1/^{\circ}\mathtt{C}$ for cobber. [Giancoli, 2009]
R_{ph0} is the measured stator resistance at approx. $20^{\circ}\mathtt{C}$.
T_{amb} is the ambient temperature around the stator windings.
T_{ref} is the reference temperature at approx. $20^{\circ}\mathtt{C}$.

Assuming the parameter measurements acquired from Appendix A are valid for a temperature of approx. $20^{\circ}\mathtt{C}$, and that a maximum ambient temperature of $100^{\circ}\mathtt{C}$ can build up around the stator windings, a maximum increase of $\sim$30% percent is calculated using (7.1). For caution and uncertainty, additionally $\pm$20% variation is added. The stator resistance is therefore varied in the interval shown in (7.2).

$$0.5R_{ph} \leq R_{ph} \leq 1.5R_{ph} \quad [\Omega] \tag{7.2}$$

When the stator current amplitude reach a certain level the magnetic properties of the iron material in the stator changes due to the saturation phenomenon. This causes the reluctance path of the stator flux to change, hence the machine inductances changes. Therefore, it is important to analyse the effects of saturation when utilizing model based deadbeat control. As the synchronous inductances are a product of mechanical construction dimensions, material properties, and machine operating

point, the interval of which the inductances varies is hard to establish and out of scope of this thesis. Therefore, the inductances are varied according to (7.3).

$$0.5L_{d,q} \leq L_{d,q} \leq 1.5L_{d,q} \quad [\mathrm{H}] \tag{7.3}$$

In order to analyze the behaviour of the system under variations of its parameters, simulations will be performed by varying only one parameter while keeping the other at its nominal value.

7.2 PI Controller Stability

This section contains the effect of model parameter errors and its performance influence for the traditional FOC PI controller. Since the PI controller is designed based on classical linear control theory, the stability can be assessed based on the position of the system poles under parameter variations. As explained in Section 3.3, the controller is designed based on the current loop transfer functions in (3.3) and (3.4). Assuming that the Back-EMF terms are removed using the decoupling technique and that both inductances are changed simultaneously, the pole-zero map shown in Figure 7.1 illustrates the closed-loop stability under parameter variations for both current loops.

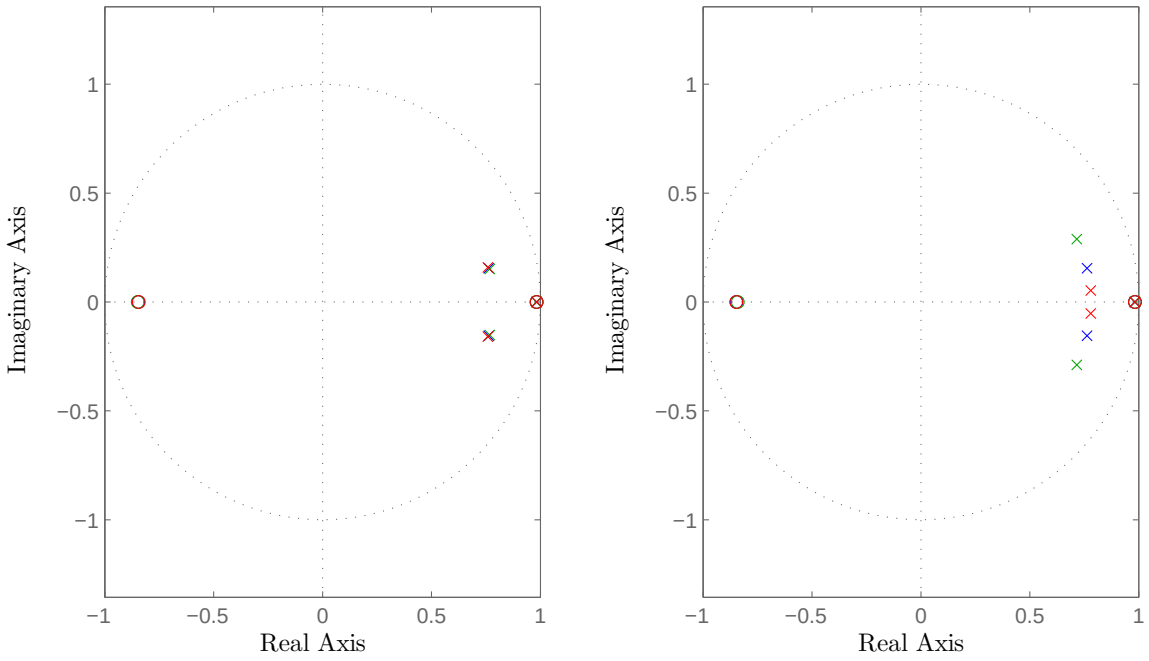

Figure 7.1. Discrete pole-zero map of the PI current controller at 5 kHz. Left: Resistance value variation. Right: Inductance value variation.

As seen from Figure 7.1 the largest influence on the stability, is determined by the inductance due to its position in the transfer function. The pole-zero map reveals that the system poles remains within the unit circle, hence the PI controller stabilizes the system under such parameter variations. Observed, is that the inductance variation, causes the poles to move away or closer to the real axis, hence changes the damping of the system. Therefore it is expected that the characteristics of a step response will be affected. The resistance value variation only slightly move the poles, hence the step response is affected at the minimum by the resistance variation.

7.3 Predictive Deadbeat Control

This section contains the analysis of parameter errors for the predictive current deadbeat control with dead-time compensation. As the deadbeat controller is based on the discretized machine voltage equations, classical linear control theory is not easily used for analysis. Instead the analysis is based

upon simulation results obtained under the above specified parameter errors. In order to evaluate the performance of the deadbeat controller, the d- and q-axis current steady-state errors and current ripples are compared to results obtained using the classical PI current controller, under the same parameter errors.

The steady-state error and current ripple are calculated respectively using (7.4) and (7.5), for a time period of 0.1 s in steady state, corresponding to $n = 500$.

$$\epsilon i_{ds}^r = i_{ds}^{r*} - \frac{1}{n}\sum_{j=1}^{n} i_{ds,j}^r \quad [\mathrm{A}] \tag{7.4}$$

$$\Delta i_{ds}^r = \max\left(i_{ds}^r\right) - \min\left(i_{ds}^r\right) \quad [\mathrm{A}] \tag{7.5}$$

Figure 7.2 presents the simulated currents for nominal parameters for both the PI controller and the predictive deadbeat controller.

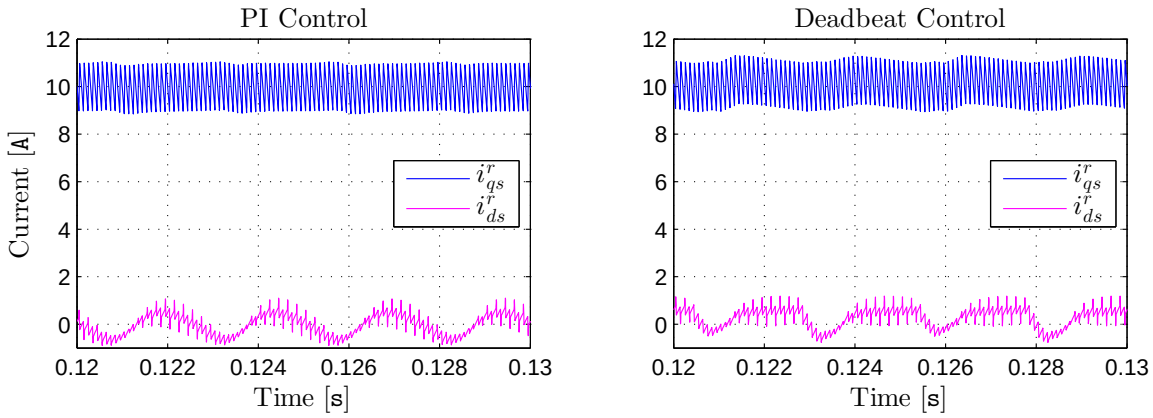

Figure 7.2. Simulated d- and q-axis currents. Left PI control and right deadbeat control.

In this case it is seen that the ripple of the q-axis current is higher for the predictive deadbeat controller. Based on the data in Figure 7.2, Figure 7.3 presents a bar-chart of the simulation results obtained, and serves as a reference for comparison to the scenarios with parameter errors.

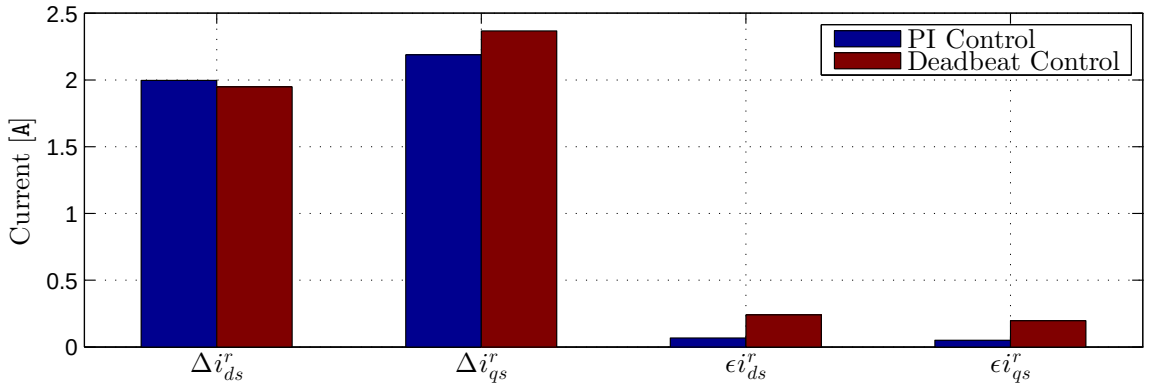

Figure 7.3. Simulated steady state error and current ripple for nominal parameters.

In Figure 7.3 it is seen that both controllers satisfactory work for controlling the PMSM currents. The current ripples for both controllers have similar amplitudes as they both use the same SVPWM technique.

Concerning steady state error, the PI current controller is as expected superior due to its integrator part which eliminate steady state error continuously. The steady state error for the deadbeat controller

is relatively low corresponding to approx. 2 % for both currents. Figure 7.4 shows the simulations results obtained for a 50 % stator resistance.

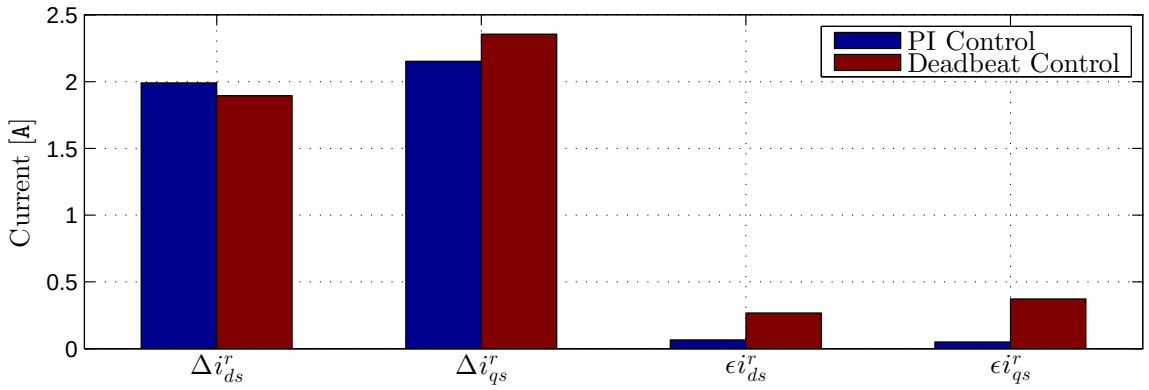

Figure 7.4. Simulated steady state error and current ripple for 50% stator resistance.

As seen in Figure 7.4 the current ripples are almost identical to those obtained for nominal parameters. A decrease of approx. 1-3 % is observed for both controllers. The steady state error for the PI controller is unaffected, while the steady state error for the deadbeat controller is increased since the deadbeat voltages are calculated based on the nominal model parameters. Figure 7.5 presents the simulation results for the scenario with a 150 % stator resistance.

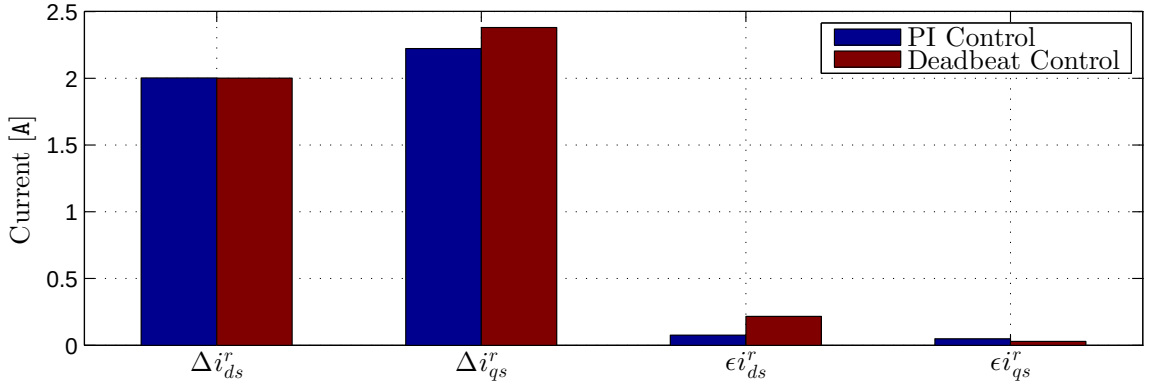

Figure 7.5. Simulated steady state error and current ripple for 150% stator resistance.

From Figure 7.5 the affection for the PI current controller is at the minimum, only producing a few percents deviation from the scenario with nominal parameters.

For the deadbeat controller, the increase in stator resistance corresponds to applying increased deadbeat voltages. This has as seen caused the steady state current ripple to increase at the minimum. The steady state error is decreased for both the d- and q-axis currents, hence the increase in machine stator resistance actually has resulted in more accurate deadbeat voltages. Figure 7.6 presents the results obtained for 50 % synchronous inductances.

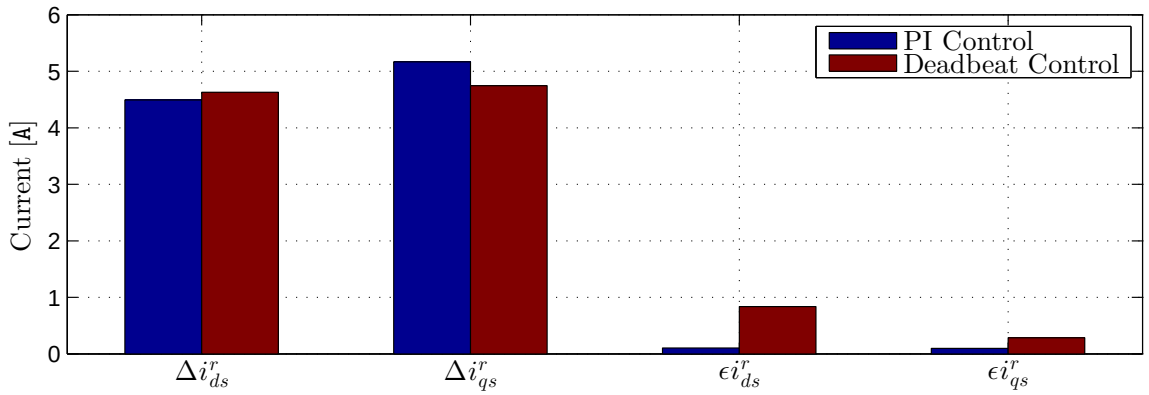

Figure 7.6. Simulated steady state error and current ripple for 50% synchronous inductance.

As the inductance value is inversely proportional to the rate of change of the current, the current ripple will increase for a decreased inductance value. From Figure 7.6 this is seen, which has an increased y-axis scale. The steady state current ripple is approx. doubled for both the PI controller and the deadbeat controller. The steady state error for the PI controller is increased to approx. twice the nominal. The deadbeat d-axis steady state error is increased with approx. 350 % compared the the nominal, while the q-axis error is increased with 150 %. Figure 7.7 presents the results obtained for 150 % synchronous inductances.

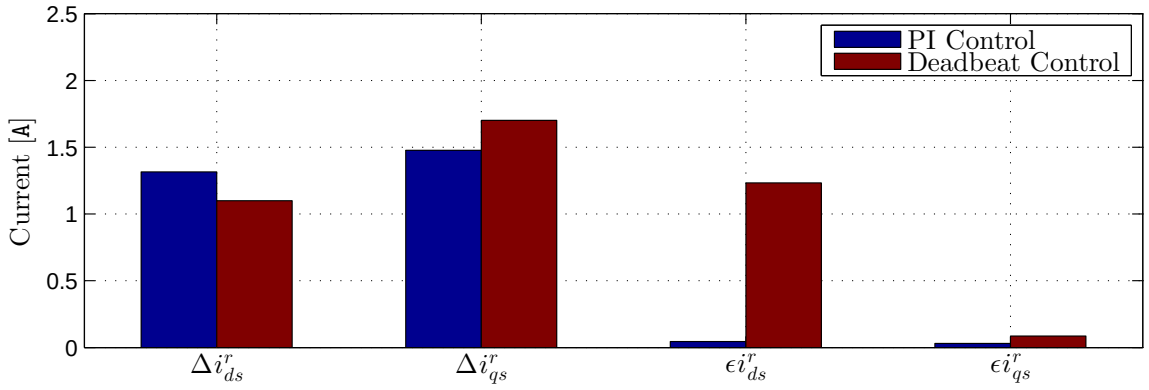

Figure 7.7. Simulated steady state error and current ripple for 150% synchronous inductance.

As Figure 7.7 shows, the current ripple is decreased due to the increased machine inductance. The PI controller current ripple is decreased, which results in a smaller steady state error. The deadbeat current ripples are likewise reduced, respectively with 44 % and 29 % for the d- and q-axis currents. The steady state error for the d-axis current is increased with 500 %, while the q-axis error is decreased with 50 %.

Based on the results obtained in this analysis, it can be concluded that the FOC PI controller results as expected vary very little when the stator resistance is changed. As expected the current ripple is affected for machine inductance variation since it is directly dependent on that.

The deadbeat controller has been shown to be noticeable affected when the machine parameters are varied. Since the deadbeat control voltages are calculated based on the nominal parameters in all cases the behaviour is expected. The worst scenario concerning the steady state accuracy of the torque current is when the machine stator resistance is decreased to 50 %, while for the d-axis current when the machine inductance is increased to 150 %. The torque current ripple of the deadbeat controller was shown in Chapter 5 to contain an equal level of harmonics as the PI controller. When parameter errors are present, the torque current ripple is seen in this analysis to increase in all cases except when the inductance is decreased to 50 %. This underlines the importance for a proper identification of the

machine parameters, in order to minimize the torque current THD level when using deadbeat control. Furthermore, the deadbeat controller have been shown not to become unstable due to parameter mismatches, showing similar stability to the FOC PI controller.

7.4 Experimental Sensitivity

In order to further evaluate the sensitivity of parameter mismatches for the deadbeat controller, this section presents some experimental performance of the deadbeat controller under the previous specified parameter errors introduced in the predictive deadbeat controller algorithm. Figure 7.8 presents the measurements obtained for a q-axis current step command of 10 A with a controller stator resistance of 50 %.

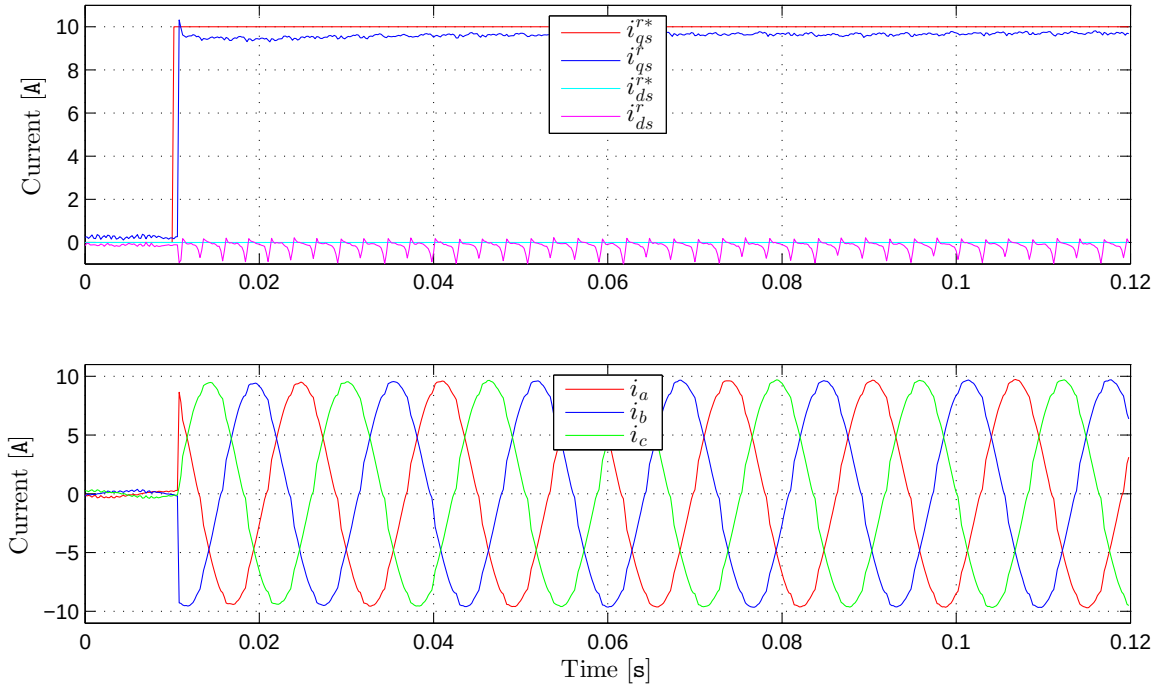

Figure 7.8. Measured performance of a 10 A q-axis current step response for a controller stator resistance of 50%.

As seen from Figure 7.8 the response is affected due to the decreased stator resistance. The steady state error is increased to 3.3 % compared to Figure 6.11 for the q-axis current. The settling time is 3.5 sampling periods or 0.7 ms. A small overshoot of 6.7 % is also seen. As the d-axis current also is a product of the deadbeat voltages, its performance is also affected by the parameter errors. The average steady state error for the d-axis current is calculated to 0.175 A. Concerning an increased stator resistance, the performance under the same conditions are presented in Figure 7.9.

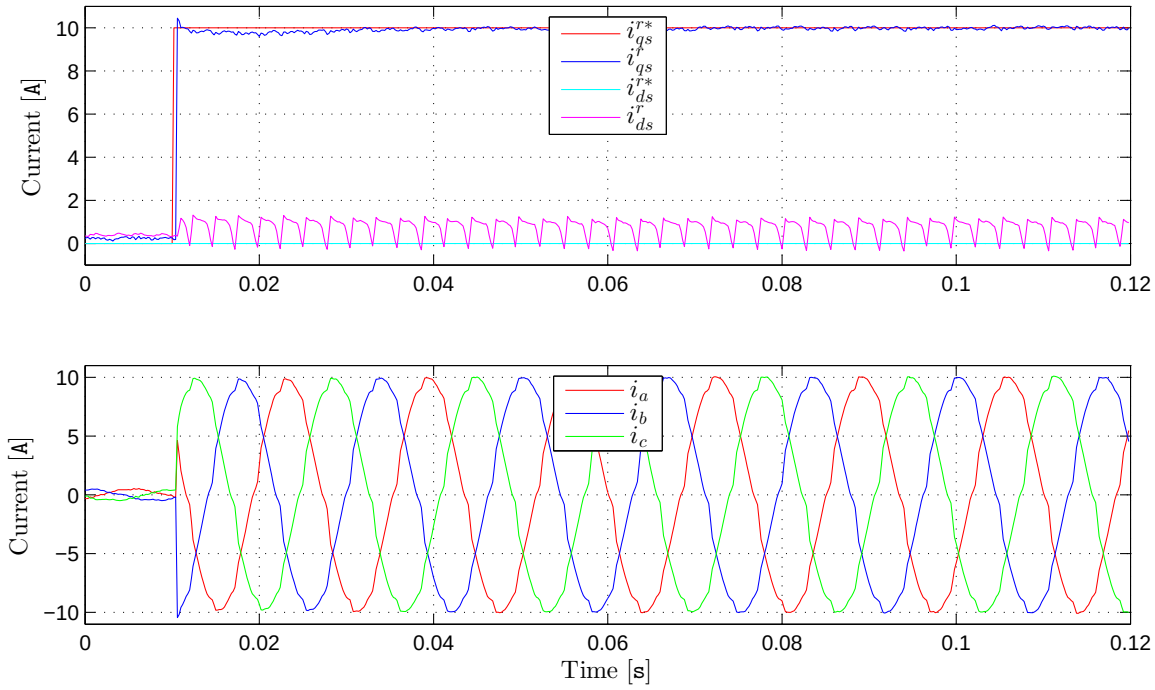

Figure 7.9. Measured performance of a 10 A q-axis current step response for a controller stator resistance of 150%.

From Figure 7.9 an almost eliminated q-axis current steady state error of 0.1 % is seen. The settling time is 3 sampling periods, and an overshoot of 4.6 % is seen. The average d-axis current steady state error is increased to 0.740 A. Figure 7.10 presents the experimental performance for a controller synchronous inductance of 50 %.

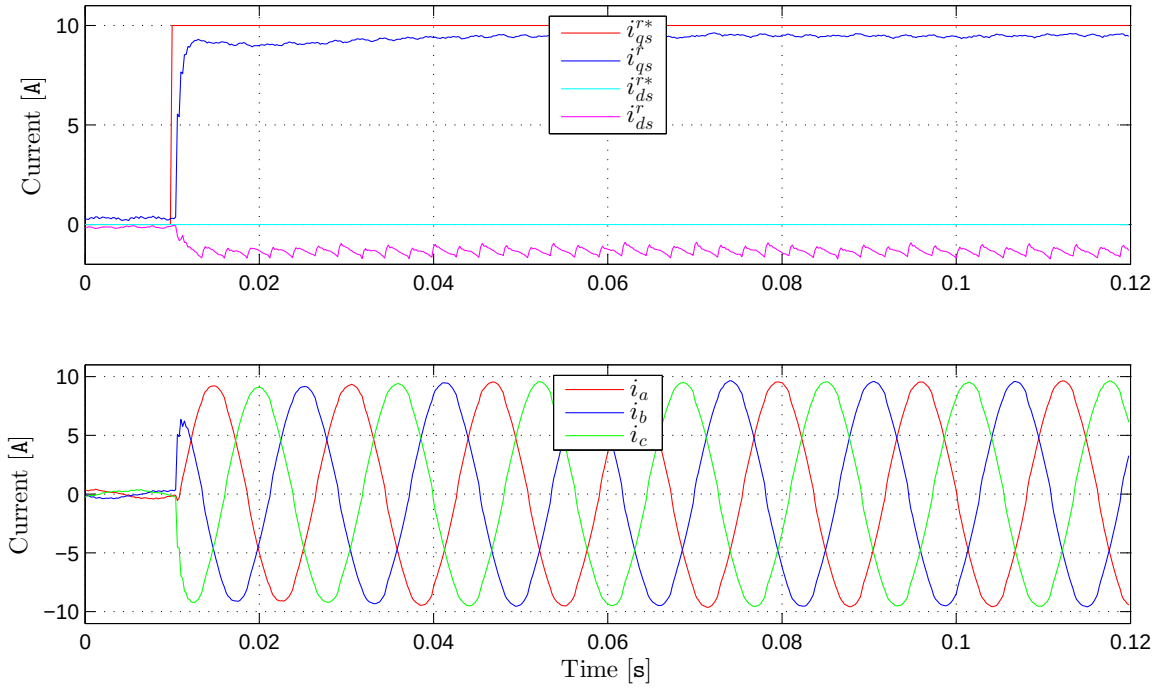

Figure 7.10. Measured performance of a 10 A q-axis current step response for a controller synchronous inductance of 50%.

Figure 7.10 shows a q-axis current steady state error of 5.2 %, and an increased settling time of approx. 14 ms. The d-axis current steady state error is increased to 1.350 A which indicates a clear performance

decrease. In Figure 7.11 the measurement obtained for a controller synchronous inductance of 150 % is presented.

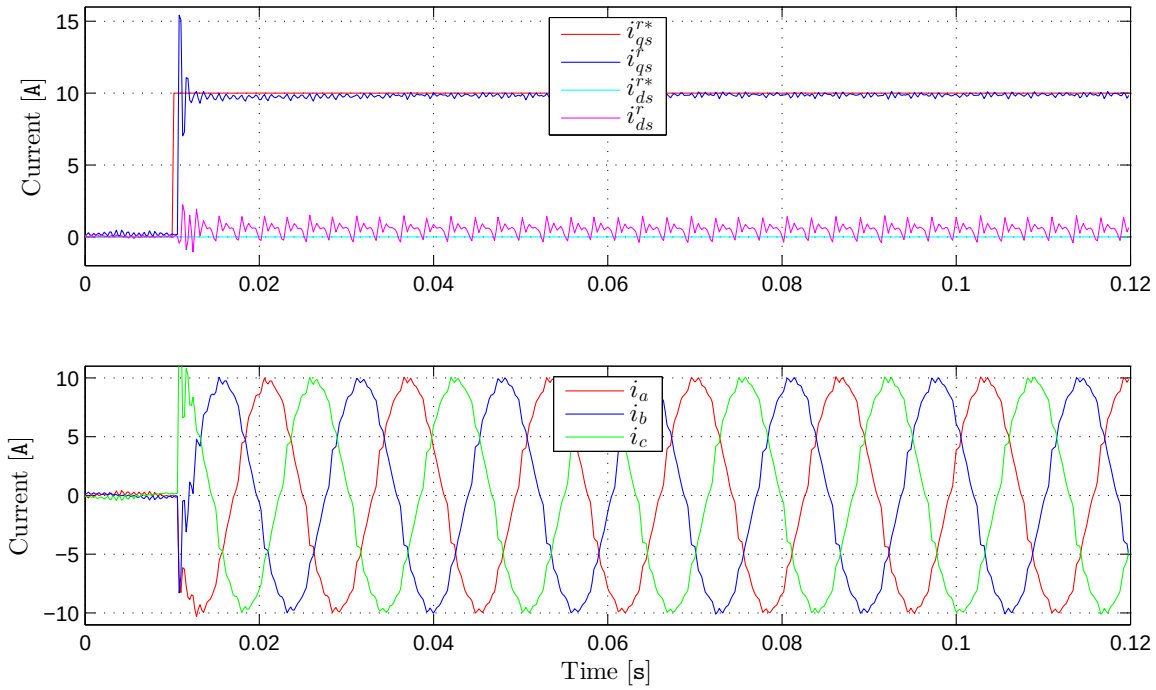

Figure 7.11. Measured performance of a 10 A q-axis current step response for a controller synchronous inductance of 150%.

Figure 7.11 shows an initial overshoot followed by a decreasing oscillation for the q-axis current. The overshoot is calculated to 54.5 %, while a low amplitude persistent oscillation is observed in steady state. The settling time is approx. 18 ms, while an average steady state error of 1.2 % is observed. For the d-axis current, an average steady state error of 0.536 A is seen.

Based on the results shown in this section, the most affecting parameter is the synchronous inductance. The transient period is almost not affected by the resistance variation, and the resistance variation causes as seen the steady state accuracy of both currents to vary.

The inductance variation is more dominant and controls both the steady state accuracy and the transient. By comparing Figure 6.11, 7.9, and 7.11 the q-axis steady state accuracy is increased when the deadbeat parameters are increased, while the d-axis steady state accuracy is decreased. The THD level of the q-axis currents for all three cases are respectively 1 %, 1 %, and 2 %, hence the significant improvement is the q-axis current accuracy, while the THD level is almost not affected by the parameter variations. The phase a current THD level is increased to 6.7 % for Figure 7.11, compared to 3 % for the nominal deadbeat controller parameters, shown in Figure 6.11 and 6.16.

A decreased inductance causes an increased steady state error and a decreased settling time, while an increased inductance introduce undesired oscillations, that affect the transient torque performance and an increased steady state accuracy with an increased settling time due to oscillations. Therefore, it could be of interest to investigate methods for estimating a proper inductance value for different current levels to obtain the most accurate results, reducing the steady state error and sustaining a low settling time without oscillations and significant overshoot.

Chapter 8
Discussion and Improvements

To further improve and analyse the performance of the deadbeat controller this chapter discusses the observed problems and suggests possible techniques, that can be applied to obtain even more attractive results. The simulation and experimental results have shown that the deadbeat algorithm is sensitive to model parameter mismatch, decreasing the dynamic performance and the steady state accuracy.

The most affecting parameter error was shown to be the synchronous inductance, which introduced undesired oscillations in the currents and decreased the accuracy. This algorithm sensitivity calls for a method, that can account for a proper model inductance value at different operation points. Therefore an attempt to identify the inductance at different operation points i.e. current levels based on applying the zero voltage vector to the machine terminals is made in the simulations.

Additionally, from an industrial point of view, the efficiency of the drive system is important. This chapter also discusses how the electrical losses can be decreased by applying a negative d-axis current that decrease the core losses of the machine, hence increasing the efficiency.

The aim of this chapter is not to experimentally test the proposed techniques in the dSPACE laboratory setup, but rather to discuss and investigate possible areas of improvement for the deadbeat algorithm, which can positively benefit the control performance and promote the efficiency of the drive system.

8.1 Compensation of the Inductance Variation

The field inductance varies as the reluctance path in the PMSM change under different operation points i.e. current levels. When the machine iron core becomes saturated the reluctance path change, causing the inductance value to decrease.

A possible method for compensating the inductance variation is to use the procedure in Appendix A and obtain the inductance value at different current levels. This produces coordinates in a coordinate system which can be fitted to a function or stored in a look-up table for representing the inductance variation at different current levels. This method requires additional offline testing, but offers compensation for the inductance variation.

An online technique is rather useful since offline testing is avoided, and at the same time the technique can be adopted for other machines. By manipulating the machine voltage equations, an attempt to determine the machine inductance can be carried out. By trusting (2.12) and (2.13), these can be used to estimate the inductance. For the Siemens SMPMSM the synchronous inductances are equal, hence $L = L_q = L_d$ which produces (8.1) and (8.2).

$$v_{ds}^r = R_{ph} i_{ds}^r - \omega_r L i_{qs}^r + L \frac{d}{dt} i_{ds}^r \quad [\mathtt{V}] \tag{8.1}$$

$$v_{qs}^r = R_{ph} i_{qs}^r + \omega_r (L i_{ds}^r + \lambda_{pm}) + L \frac{d}{dt} i_{qs}^r \quad [\mathtt{V}] \tag{8.2}$$

The outcome is two possible equations that can be used to determine L. A rough estimate of L can possibly be obtained by assuming the derivative terms to be zero in steady state i.e. after any transients induced by start-up or a step change of the currents.

Unfortunately, simulation results show that the derivative term cannot be neglected in (8.1) and (8.2), causing the identification of the machine inductances to fail, as the machine currents are non-constant in steady state. This is because the assumption is rather imprecise, as the derivative terms are non-zero at all times due to the on/off nature of the inverter voltages.

The estimation of the inductance is difficult as the voltages are controlled by the inverter causing continuous current ripples in steady state. Compared to the locked rotor test in Appendix A, a more convenient method could though be advantageous.

In order to estimate the inductance the derivative terms must be removed for this method to work, as otherwise (8.1) and (8.2) cannot be reliably isolated for L. In order to get rid of the derivative terms, a zero voltage vector can be commanded to the inverter in a short time period, causing the derivative terms to become zero. This will eventually allow estimation of the inductance using either (8.3) or (8.4).

$$L = -\frac{R_{ph} i^r_{ds}}{\omega_r i^r_{qs}} \quad [\mathtt{H}] \tag{8.3}$$

$$L = \frac{R_{ph} i^r_{qs} + \omega_r \lambda_{pm}}{\omega_r i^r_{ds}} \quad [\mathtt{H}] \tag{8.4}$$

As (8.3) or (8.4) are reliable only when i^r_{ds}, i^r_{qs}, and ω_r are non-zero this is a criteria for using the proposed method. By initially operating the machine at a given speed level, the conditions are fulfilled as the three variables will be non-zero.

To verify the above suggestion, Figure 8.1 presents the simulation results of the proposed method. The results are obtained in the case where the PMSM initially is sped up to 1000 $\mathtt{min}^{-1}$, with $i^{r*}_{ds} = -1$ $\mathtt{A}$ and $i^{r*}_{qs} = 10$ $\mathtt{A}$. At $t = 0.02$ $\mathtt{s}$ the zero voltage vector $\mathbf{V}_0(000)$ is applied.

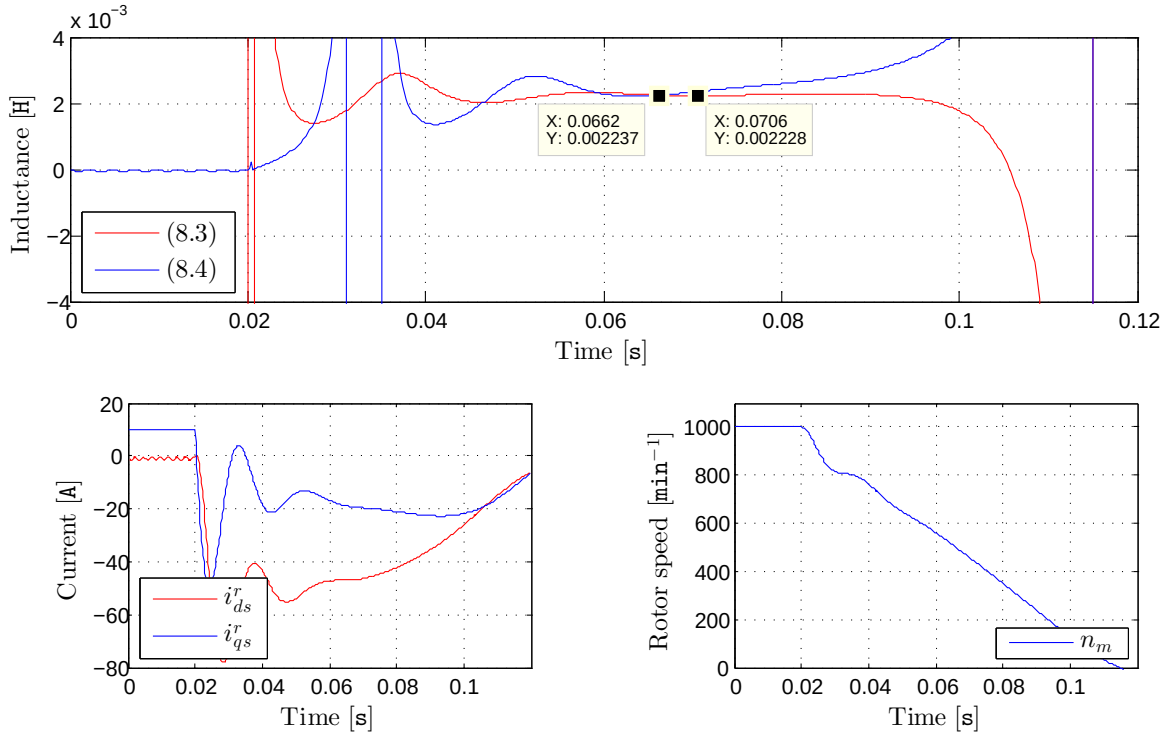

Figure 8.1. Zoomed view of the inductance identification using (8.3) and (8.4). The variables are sampled at 5 $\mathtt{kHz}$.

As seen in Figure 8.1 the inductance prior to applying the zero voltage vector is not identified properly. When the zero voltage vector is applied, a sudden change in the d- and q-axis currents occur, and the

rotor speed starts to decrease. After approx. 0.02 s the functionality of the inductance identification is demonstrated. The two data points indicates that the inductance obtained respectively using (8.4) and (8.3) is close to the model inductance of $L = 2.2$ mH. Figure 8.1 suggests in the given scenario that (8.3) is the best choice for identification as the output is approx. constant for a longer time, before diverging due to the decreasing rotor speed and currents.

Based on Figure 8.1, the current levels exceed the dSPACE system limitations. This happens as the speed voltages are significant at this level, causing the currents to increase when the zero voltage vector is applied. The high current levels cause the machine iron to saturate, hence in a practical setup the inductance obtained is decreased. To overcome these high current levels in the dSPACE setup the IM can be used to control the speed. By operating at a lower speed level, the currents can be limited since the speed voltages are a product of the rotor speed. Figure 8.2 presents the simulation results obtained for a constant rotor speed of 10 min^{-1} under the same initial conditions as Figure 8.1.

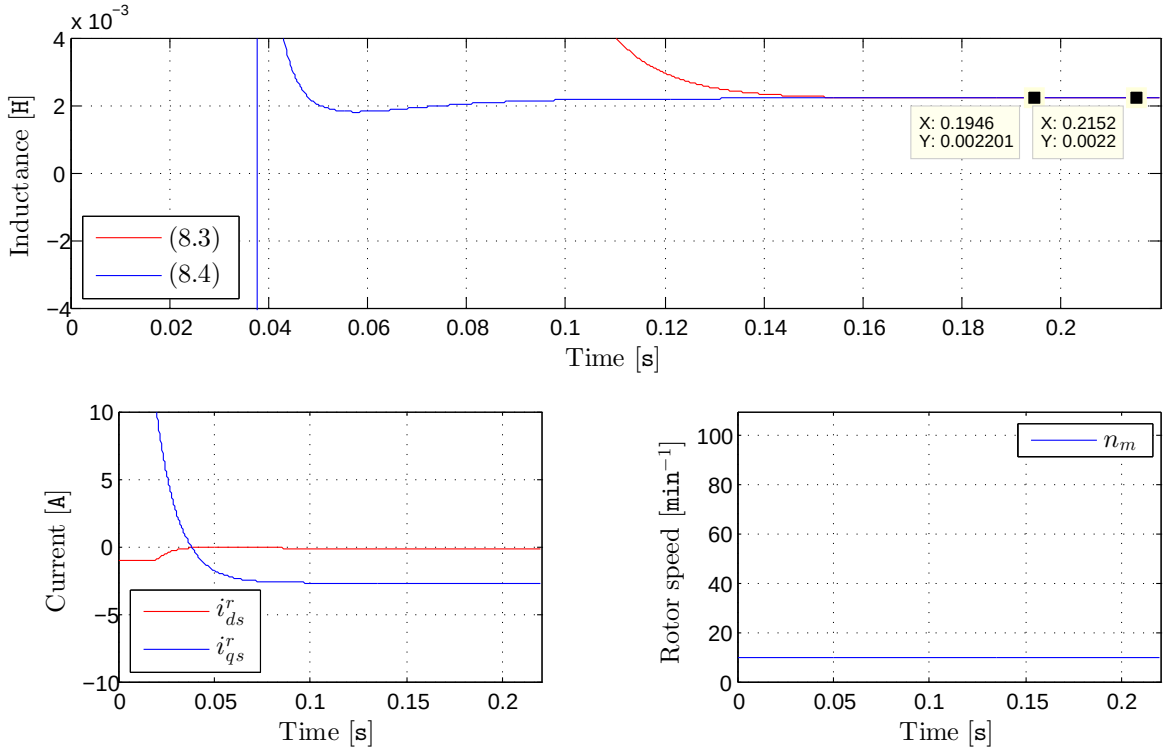

Figure 8.2. Zoomed window of the identification of L using (8.3) and (8.4) for a constant rotor speed of 10 min^{-1}. The variables are sampled at 5 kHz.

From Figure 8.2 the current levels are significantly lowered, resulting in identification of the inductance at proper current levels hence avoiding the saturation phenomenon. When the rotor speed is controlled using the IM, the speed voltages are constants, hence the variables used for identification are constant. This allows the algorithm to converge to the proper model inductance value, as shown by the two data points in Figure 8.2.

Both Figure 8.1 and 8.2 shows that in theory it is possible to estimate the machine inductance by applying the zero voltage vector. The current levels were shown controlled by the rotor speed, hence the inductance variation as a function of current level can be obtained by the discussed method.

The method cannot directly be categorized as an online estimation technique as the inductance variation must be identified prior to operation and stored in a look-up table for utilization. The method can possibly simplify the inductance determination compared to the locked rotor test, and might be automated by extending the functionality. As the technique is only demonstrated in the simulations, a further study on its experimental performance and automation options could be beneficial for

improving the deadbeat controlled performance of the PMSM.

It is known from [Lu et al., 2013] that the d- and q-axis inductances of a SMPMSM vary a as function of both the d- and q-axis currents. This discussion has neglected this phenomenon, and only demonstrated how the inductance may be determined by using the machine equations.

8.2 Maximum Efficiency Control

Operating the PMSM at its maximum efficiency at all operation points is a good candidate in many applications. With today's focus on energy optimization and consumption reduction, this control strategy is very interesting. An example of a drive system application with energy optimization in focus, is in an electrical vehicle. In this application the travel distance of the vehicle can be optimized if the losses of the electrical machine are minimized at all operation points. As the machine is supplied by a battery bank, the travel distance is limited by the energy storage capacity of the battery bank, hence operating at maximum efficiency optimizes the travel distance. Furthermore, operating at maximum efficiency enables higher thermal robustness and hence, a longer lifetime of the machine insulation which results in high operational reliability of the drive system. The analysis in this section ignores loss occurring in the VSI, hence only the machine losses are analysed. That the increased VSI loss under modified machine control is smaller than that of the incremental electrical loss in the machine is a fair assumption. [Krishnan, 2010]

The maximum efficiency is obtained when the total machine losses are minimized. The total losses in the machine constitute of the mechanical losses and the electrical losses. The mechanical losses are determined by the friction in the bearings and the Coulomb friction, whereas the total electrical losses by the stator resistive losses and the machine core losses. The mechanical losses cannot be optimized by changing the operation of the inverter supplying the PMSM, and is therefore considered as a constant proportional to the operational speed. In contrast the electrical losses can. They constitute of resistive stator winding losses and core losses.

The resistive stator winding losses are proportional to the square of the stator current amplitude, hence by decreasing the stator current amplitude the resistive losses are decreased. In other words, the losses are decreased to 1/4 if the current amplitude is halved. As the electromagnetic torque is a product of the machine currents, the amplitude of the currents cannot simply be commanded to a lower value.

The core losses of the machine constitute of hysteresis- and eddy current losses which depend upon the magnetic properties of the core material which are affected by the magnetic field flux density and frequency. The core losses are determined by the flux density in the machine core material which may be reflected by the total flux linkage of the machine. Hence by decreasing the flux density in the core, the core losses can be decreased. [Krishnan, 2010]

The total flux linkages, which are in the air gap between the stator and rotor cores, are the result of the rotor- and stator flux linkages. The rotor flux linkage is concentrated in the direction of the d-axis and its q-axis component is zero. The stator flux linkages have in turn two components; one in the direction of the d-axis, and one in the direction of the q-axis. The stator flux linkages are given by $L_d i^r_{ds}$ and $L_q i^r_{qs}$ respectively for the d- and the q-axis. The total flux linkages can be described by its phasor diagram shown in Figure 8.3.

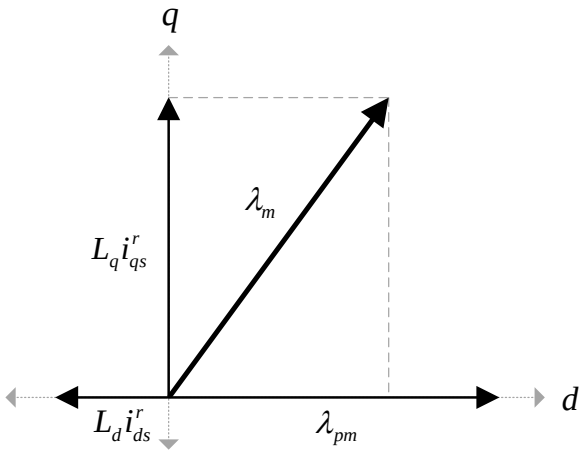

Figure 8.3. Phasor diagram illustrating the total flux linkages in the PMSM for the case when $i^r_{ds} < 0$ A.

According to the phasor diagram, the total flux linkages amplitude is described by (8.5), while the phase is the arc-tan of the ratio between the q-axis to the total d-axis flux linkages.

$$\lambda_m = \sqrt{\left(\lambda_{pm} + L_d i^r_{ds}\right)^2 + \left(L_q i^r_{qs}\right)^2} \quad [\text{Wb}] \tag{8.5}$$

As the total flux linkages are a product of the d- and q-axis currents, assuming the synchronous inductances are constants independent of current level, the zero direct axis control strategy can be modified by commanding a d-axis current, hence affecting the total flux linkages. By commanding a negative d-axis current the amplitude of the effective d-axis flux linkage decreases. This causes the total flux linkages to decrease, resulting in a decreased flux density in the machine core and hence a decreased core loss.

8.2.1 Strategy

Instead of controlling the torque angle to $\delta = 90°$ as in the case of zero direct axis control, the angle can as discussed be modified by commanding a d-axis current. Having in mind that the electromagnetic torque is solely controlled by the q-axis current for the SMPMSM as shown in (8.6)

$$T_e = \frac{3}{2} p_p \left[\lambda_{pm} + (L_d - L_q) i^r_{ds}\right] i^r_{qs} \quad [\text{Nm}] \tag{8.6}$$

the torque level can be maintained if the q-axis remains constant, independent of the commanded value of the d-axis current. The means that the total flux linkages can be decreased without affecting the torque performance by commanding a negative d-axis current according to (8.5).

Even though the amplitude of the stator current vector and thereby the resistive stator winding losses increase when commanding a negative d-axis current, there exist a trade off between decreasing the core losses while increasing the resistive winding losses and minimizing the total electrical machine losses. This means that for every operation point, there exist a combination of d- and q-axis currents that combined minimizes the electrical losses, if the core loss reduction is large enough to overcome the increase of the resistive stator winding losses.

8.2.2 Experimental Demonstration

To understand the influence of the PMSM core loss, a primitive power balance for the dSPACE setup can be formulated as in (8.7), when the IM is operated to control the speed of the system drive shaft,

$$P_{IM,in} = P_{mech} + P_{IM,cu} + P_{PMSM,cu} + P_{IM,co} + P_{PMSM,co} \quad [\text{W}] \tag{8.7}$$

where:
$P_{IM,in}$ is the input power to the IM

P_{mech} is the mechanical power
$P_{IM,cu}$ is the resistive stator winding losses of the IM
$P_{PMSM,cu}$ is the resistive stator winding losses of the PMSM
$P_{IM,co}$ is the core losses of the IM
$P_{PMSM,co}$ is the core losses of the PMSM

By maintaining the PMSM electromagnetic torque equal to zero, the IM experience no load torque produced by the PMSM q-axis current. In this case the IM input power is determined by the IM- and PMSM stator resistive losses, the IM- and PMSM core losses, and the mechanical losses.

Rearranging (8.7), allows for a formulation of the combined core losses of the machines, as shown in (8.8).

$$P_{IM,co} + P_{PMSM,co} = P_{IM,in} - P_{mech} - P_{IM,cu} - P_{PMSM,cu} \quad [\mathtt{W}] \tag{8.8}$$

As the input power to the IM, and the IM- and PMSM resistive stator winding losses can be estimated through the dSPACE setup, and that the mechanical losses can be estimated for a speed of 1000 $\mathtt{min}^{-1}$ as in (8.9)

$$P_{mech} = \omega_m \left(B_m \omega_m + J_0 \right) = 42.35 \quad [\mathtt{W}] \tag{8.9}$$

the combined core loss can be measured for different levels of PMSM d-axis current. Figure 8.4 presents the results obtained from a laboratory test at 1000 $\mathtt{min}^{-1}$ for different levels of PMSM d-axis currents.

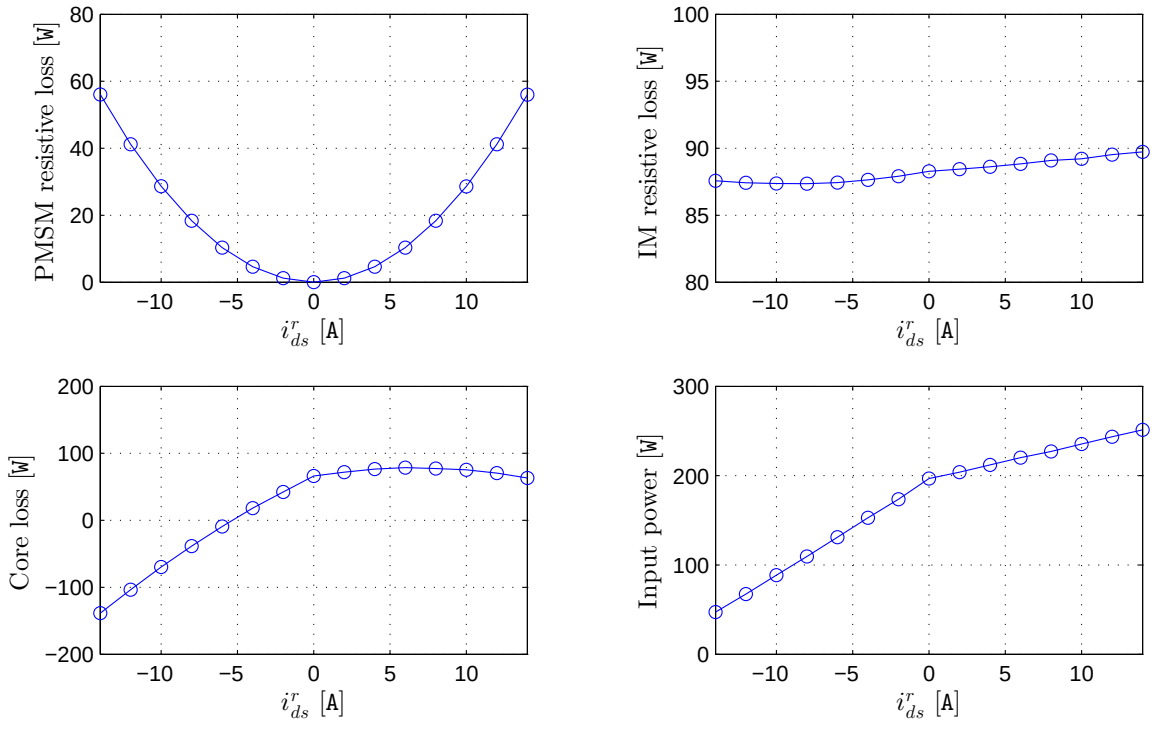

Figure 8.4. Obatined power flows of the dSPACE setup when the system is operated by the IM at 1000 $\mathtt{min}^{-1}$ as a function of PMSM d-axis current. The bottom left figure represents the core losses measured according to (8.8).

From Figure 8.4 it is seen that the IM input power decrease as the PMSM d-axis current is decreased. This trend is expected as the d-axis flux density of the PMSM is decreased, causing the interaction between the stator windings and the rotor magnetic field to weaken. Furthermore, as seen from the IM resistive loss the IM current amplitude is decreasing, which supports the decreasing IM input power. The PMSM resistive loss is likewise having the correct trend.

Looking at the combined core loss for positive *d*-axis current, the losses saturate and eventually start to decrease. This behaviour is caused by the saturation of the stator core material which becomes non-linear in its saturation region. The core material becomes saturated as the magnetic field flux density is increased.

Figure 8.4 is used to illustrate that the power balance is determined by variation of the PMSM *d*-axis current. The results are obtained under primitive conditions, not utilizing a torque transducer or a power analyzer, causing possible disagreements. Some disagreement exist in the results, as the core loss becomes negative for negative *d*-axis current levels lower than approx. -5 `A`. The wrong y-axis scale may be explained by wrong assumptions about the mechanical losses, which should be measured correctly. As the trends shown in Figure 8.4 appear as expected the principle of this strategy is demonstrated.

To verify the increasing efficiency of the PMSM another possibility is to operate the machine at a constant operation point i.e. speed level with a given load torque, and apply different levels of negative *d*-axis currents. This will eventually indicate the point of minimum input power, hence the point with maximum efficiency for this operation point.

8.2.3 Implementation

The concept of maximum efficiency control is simple and intuitive, but as the core loss is a complex quantity, the point of maximum efficiency is not easily identified using a simple algorithm for variable operation points. A possible solution is to identify the points of maximum efficiency in a separate test, and load them into look-up tables. Then depending on the speed and the torque current, the field current that minimizes the electrical losses, is commanded as the *d*-axis current reference.

Chapter 9
Conclusion

The objective of this thesis was according to the problem statement in Section 1.5 to analyse, design and implement deadbeat current controllers as a replacement for the classical PI current controllers in FOC of a PMSM. This was done in order to examine and map out the improvements and problems arising from such a replacement. In order to compare the results obtained with this alternative controller, a classical FOC strategy was also designed and implemented for the PMSM.

Chapter 3 was dedicated to the design of the classical PI current controllers. The controller design ended up in simulations to produce a settling time of 2.25 `ms` with a 2 % overshoot for a step response. However, the experimental response disagreed due to the non-linearities in the inverter. Therefore, the experimental PI controller parameters were readjusted to compensate for this system behaviour. The experimentally tuned parameters produced a settling time of approx. 4.7 `ms`, and a minimal overshoot of approx. 3 %.

The deadbeat current controller was introduced in Chapter 4. The deadbeat controller implementation was shown to be simple and intuitive, as it directly replaces the two PI controller loops. Based on simulation results obtained using the conventional deadbeat controller, it was observed that the system delay caused the response to oscillate. Predictive current delay compensation was therefore built-in together with inverter dead-time compensation, to improve the steady state accuracy. Simulation results, showed the significant improvement. Furthermore, rotor position delay compensation and deadbeat voltage constraint, were built-in to the model, to further improve the accuracy and functionality of the conventional deadbeat controller.

Simulation results based on the experimentally tuned PI parameters, found in Chapter 5, obtained at a constant speed of 1000 RPM and an inverter switching frequency of 5 `kHz`, pointed out the performance improvements introduced by the deadbeat current controllers. As the name deadbeat refers to, the transient period was improved significantly reducing the settling time from approx. 5 `ms` for the PI controlled response, to approx. 0.6-0.8 `ms` for the deadbeat controller. As the simulation models included modelling of the inverter dead-time, the effects of this was seen to decrease the model based deadbeat controller steady state accuracy, while the PI controller accuracy was unchanged. Spectral analysis revealed that the harmonic content of the deadbeat controlled machine currents was less than the PI controlled machine currents. The experimental performance was therefore expected to be similar, or the improvements even more distinct as the real system has a non-linear nature.

In Chapter 6 the experimental results obtained in the dSPACE setup were presented. Under the same conditions as in the simulations, the PI controller produced a settling time of approx. 4-6 `ms` and a steady state error below 1 %. As shown in the simulations, the effects of adding the dead-time compensation technique was shown to increase the steady state accuracy significantly for the deadbeat controller. Likewise, the current prediction, for compensating the DSP signal- and calculation delay, was shown to effectively eliminate the previous oscillations, improving the torque ripple momentous. The proposed deadbeat controller was in experiment shown to improve the transient significantly, producing settling times of approx. 0.6-0.8 `ms`, and a steady state accuracy of 1-3 % for the q-axis current. As the q-axis or torque current was controlled by the speed loop controller, the designed PI controller of the speed loop showed in the experimental work (not shown in thesis) to suppress the effects of a static error when controlling the PMSM in speed control mode. It was noticed that the field producing d-axis current could be controlled satisfactory when the rotor position compensation was implemented, producing current errors below 0.2 `A`. Spectral analysis revealed the q-axis steady state performance improvement. The amplitude of the 5th and 7th order machine current harmonics

were lowered significantly, improving the THD level from 7 % for the PI controller to 3 % for the deadbeat controller, causing an improved THD level of the torque current from 5 % to 1 % based on the dSPACE measurements.

In order to examine the influence of model parameter errors, Chapter 7 was dedicated to the analysis of such. It was, based on classical control theory, shown that the PI controller stability was affected at the minimum by the parameter errors, causing only small changes to the closed loop system. Simulations supported this analysis. The simulations showed that the deadbeat controller steady state accuracy and current ripple, were affected by the parameter errors, whereas the PI controller is almost unaffected concerning current ripple and steady state accuracy. The steady state accuracy for the PI controller was continuously eliminated due to the integrator of the controller. The most affecting parameter error for the deadbeat controller, was shown to be the inductance, which caused the steady state accuracy to decrease.

The sensitivity analysis was also performed in the experimental setup by changing the model parameters. It was observed again that the most affecting parameter error was the inductance, causing the transient to become slower for a decreased inductance, and overshoot and oscillate for an increased model inductance. The experimental sensitivity analysis also showed that the steady state accuracy was sacrificed, causing both the d- and q-axis current loops to exhibit errors, under parameter errors.

Based on the experimental results obtained in Chapter 6 and 7, the dynamic performance of the deadbeat controller was shown to outdo the PI controller dynamic performance. The current ripple obtained using the deadbeat controller was significantly lowered compared to the PI controller, and the spectral analysis showed the effectiveness of the dead-time compensation implemented in the deadbeat controller. The steady state accuracy was shown as the main drawback of the deadbeat controller, whereas a substantial improvement in the transient response was shown compared to the PI controller. The accuracy was shown to depend on the model parameters.

Chapter 8, therefore discussed and investigated a method based on the machine voltage equations to determine the synchronous inductance of the machine, for improving the deadbeat controller performance. Simulation results showed, that by applying a zero voltage vector, the inductance could be estimated. In theory, by utilizing this method, compensation of a varying inductance due to the saturation phenomenon could eventually be incorporated into the deadbeat algorithm.

As an extra input, Chapter 8, also discussed a method on how to decrease the electrical losses of the PMSM. By increasing the torque angle, by weakening of the magnetic field flux density, the core losses of the PMSM was experimentally shown to decrease, hence increasing the efficiency of the drive system.

9.1 Future Work

The performance of the deadbeat controller showed satisfactorily to decrease the transient period of the current loops, and it was shown that the current harmonics were significantly decreased, improving the torque ripple. The steady state accuracy however was shown as a drawback which could be of interest to increase. The voltage error introduced by the non-linear inverter can be a possible explanation for this accuracy. For maximizing the accuracy, it could be interesting to implement and test an algorithm which can compensate for this voltage error. As the voltage error is dependent on the system operation point, an online estimation is a possible candidate for improving the real time accuracy.

As the inductance is a determining factor for the accuracy, a future workload could be put on incorporating and testing the inductance estimation algorithm, and/or investigate other possibilities for estimating the synchronous inductances. Moreover, further work on developing an algorithm that automatically deceases the machine core losses could be very interesting, both in the case of using the deadbeat controller and the PI controller, as such a control strategy is coveted by the industry.

Bibliography

Giancoli, **2009**. Douglas Giancoli. *Physics for scientists and engineers with modern physics.* Pearson Prentice Hall, Upper Saddle River, N.J, 2009. ISBN 0-13-149508-9.

Hwang and Kim, **March 2010**. Seon-Hwan Hwang and Jang-Mok Kim. *Dead Time Compensation Method for Voltage-Fed PWM Inverter.* Energy Conversion, IEEE Transactions on, 25(1), 1–10, 2010. ISSN 0885-8969. doi: 10.1109/TEC.2009.2031811.

Kazmierkowski, Krishnan, and Blaabjerg, **2002**. Marian P. (ed.) Kazmierkowski, R. (ed.) Krishnan, and Frede Blaabjerg. *Control in Power Electronics.* Academic Press Series in Engineering. Academic Press, Incorporated, 2002. ISBN 0124027725.

Kim, Lee, Rho, and Park, **May 2010**. Sam-Young Kim, Wootaik Lee, Min-Sik Rho, and Seung-Yub Park. *Effective Dead-Time Compensation Using a Simple Vectorial Disturbance Estimator in PMSM Drives.* Industrial Electronics, IEEE Transactions on, 57(5), 1609–1614, 2010. ISSN 0278-0046. doi: 10.1109/TIE.2009.2033098.

Krishnan, **2010**. R Krishnan. *Permanent magnet synchronous and brushless DC motor drives.* CRC Press/Taylor & Francis, Boca Raton, 2010. ISBN 9780824753849.

Li, Ming, and Dian-guo, **Sept 2012**. Niu Li, Yang Ming, and Xu Dian-guo. *Deadbeat predictive current control for PMSM.* pages LS6b.1–1–LS6b.1–6, 2012. doi: 10.1109/EPEPEMC.2012.6397489.

Lu, Lei, and Blaabjerg, **Sept 2013**. Kaiyuan Lu, Xiao Lei, and F. Blaabjerg. *Artificial Inductance Concept to Compensate Nonlinear Inductance Effects in the Back EMF-Based Sensorless Control Method for PMSM.* Energy Conversion, IEEE Transactions on, 28(3), 593–600, 2013. ISSN 0885-8969. doi: 10.1109/TEC.2013.2261995.

Moon, Kim, and Youn, **Jan 2003**. Hyung-Tae Moon, Hyun-Soo Kim, and Myung-Joong Youn. *A discrete-time predictive current control for PMSM.* Power Electronics, IEEE Transactions on, 18(1), 464–472, 2003. ISSN 0885-8993. doi: 10.1109/TPEL.2002.807131.

Morel, Lin-Shi, Retif, Allard, and Buttay, **July 2009**. F. Morel, Xuefang Lin-Shi, J.-M. Retif, B. Allard, and C. Buttay. *A Comparative Study of Predictive Current Control Schemes for a Permanent-Magnet Synchronous Machine Drive.* Industrial Electronics, IEEE Transactions on, 56 (7), 2715–2728, 2009. ISSN 0278-0046. doi: 10.1109/TIE.2009.2018429.

Phillips, **2011**. Charles Phillips. *Feedback control systems.* Pearson, Boston Mass. London, 2011. ISBN 9780132478793.

Rodriguez, **2012**. Jose Rodriguez. *Predictive control of power converters and electrical drives.* Wiley-IEEE Press, 2012. ISBN 9781119963981.

Springob and Holtz, **Oct 1998**. L. Springob and J. Holtz. *High-bandwidth current control for torque-ripple compensation in PM synchronous machines.* Industrial Electronics, IEEE Transactions on, 45(5), 713–721, 1998. ISSN 0278-0046. doi: 10.1109/41.720327.

Sukegawa, Kamiyama, Mizuno, Matsui, and Okuyama, **May 1991**. T. Sukegawa, K. Kamiyama, K. Mizuno, T. Matsui, and T. Okuyama. *Fully digital, vector-controlled PWM VSI-fed AC drives with an inverter dead-time compensation strategy.* Industry Applications, IEEE Transactions on, 27(3), 552–559, 1991. ISSN 0093-9994. doi: 10.1109/28.81841.

Wang, Yang, Niu, and Xu, **June 2011**. Hongjia Wang, Ming Yang, Li Niu, and Dianguo Xu. *Improved deadbeat predictive current control strategy for permanent magnet motor drives.* pages 1260–1264, 2011. ISSN pending. doi: 10.1109/ICIEA.2011.5975779.

Appendix A
Parameter Determination Procedure

The advanced vector control algorithms applied to the control of the PMSM requires the machine electrical- and mechanical parameters for its proper functionality. The electrical parameters are used to tune the current PI controller gains in order to obtain the desired closed-loop performance and calculate the deadbeat voltages. The mechanical parameters are used to tune the outer speed loop for the desired closed-loop performance. This procedure explains how to determine the PMSM parameters using common measurement equipment.

Finally, the obtained parameters can be used to verify or adjust the parameters given by the manufacturer and afterwards be used for computer modelling purposes.

Electrical Parameters

The electrical parameters needed for vector control of the PMSM are listed in Table A.1.

Table A.1. Electrical parameters of the PMSM.

Required electrical parameters		
Parameter	**Dimension**	**Description**
P_p	[-]	Machine pole pairs
R_{ph}	[Ω]	Per phase winding resistance
L_d	[H]	Per phase d-axis inductance
L_q	[H]	Per phase q-axis inductance
λ_{pm}	[Wb]	Rotor magnetic flux

By following the procedures given in the next sections the electrical parameters can be determined.

Machine Pole Pairs

The machine number of pole pairs defines a ratio between mechanical and electrical quantities and represents the number of north- and south poles located on the permanent magnet rotor.

The number of pole pairs is determined by rotating the PMSM using an external driving motor at a known speed. By connecting an oscilloscope to the PMSM terminals the electrical frequency of the produced back EMF voltages can easily be calculated. Using that information and knowing the mechanical frequency the number of pole pairs is obtained according to (A.1).

$$P_p = \frac{f_e}{f_m} \quad [-] \tag{A.1}$$

Winding Resistance and Inductance

A PMSM is usually wye connected. The per phase winding resistance is the resistance between stator terminal and the neutral point inside the machine. The per phase inductance is dependent on the mutual inductances and the rotor magnetics. In vector control the required synchronous inductances are constants used as a result of Park's transformation which transforms machine variables into

constants by trigonometric relations. To obtain the d- and q-axis inductances the rotor must be locked in two electrical positions respectively $\theta_r = 0$ and $\theta_r = \pi/2$. For a Surface Mounted Permanent Magnet Synchronous Machine (SMPMSM) the d- and q-axis inductances are approximately equal, since the reluctance paths are almost identical, since the relative permeability of air and the permanent magnet material are approx. equal. This is not valid for Interior Permanent Magnet Synchronous Machine (IPMSM) as the reluctance paths are different.

The stator resistance and synchronous inductances are obtained considering the PMSM electrical diagram as shown in Figure A.1.

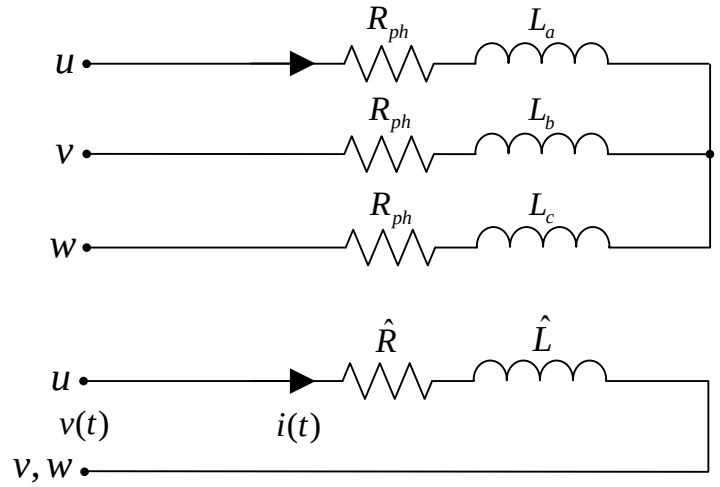

Figure A.1. Three phase electrical diagram of the PMSM (top). Equivalent circuit with phases v and w short circuited (bottom).

By short circuiting two phases, an equivalent PMSM stator circuit which reduces to a first order RL-circuit is obtained as shown in Figure A.1 (bottom). When the rotor is aligned with phase A ($\theta_r = 0$) the equivalent circuit inductance $\hat{L}$, corresponding to $(3/2)L_d$ can be calculated from the current transient waveform when applying a voltage step. When the rotor is locked to the d-axis ($\theta_r = 0$), only a d-axis voltage is present hence only a d-axis current will flow.

The current transient waveform, which is captured using an oscilloscope, is described by (A.2)

$$i(t) = \frac{V}{\hat{R}}\left(1 - e^{-\frac{t}{\tau}}\right), \tau = \frac{\hat{L}}{\hat{R}} \quad [-] \tag{A.2}$$

where:
τ is the time constant defined as the time it takes the current to reach 63.21% of the steady state value [s]
V is the magnitude of the DC voltage step applied [V]
$\hat{R}$ is the circuit resistance defined as $\hat{R} = v(\infty)/i(\infty)$ [Ω].

Rotor Position Alignment

Since the PMSM is controlled using an inverter, the rotor position can be controlled by commanding constant dq voltages, since the stator flux path of the machine then is controlled. By commanding the voltage space vector $V_1(100)$ consisting only of d-axis voltage from Section 2.2.1, the rotor will align to the d-axis or $\theta_r = 0$ since the stator flux path will point in the direction of the phase a axis. By commanding only a q-axis voltage, the stator flux will point in the direction 90° ahead of the d-axis, hence the rotor will align to the q-axis.

By obtaining the transient current waveform as shown in Figure A.2, the winding resistance and the synchronous inductances can be calculated using (A.2).

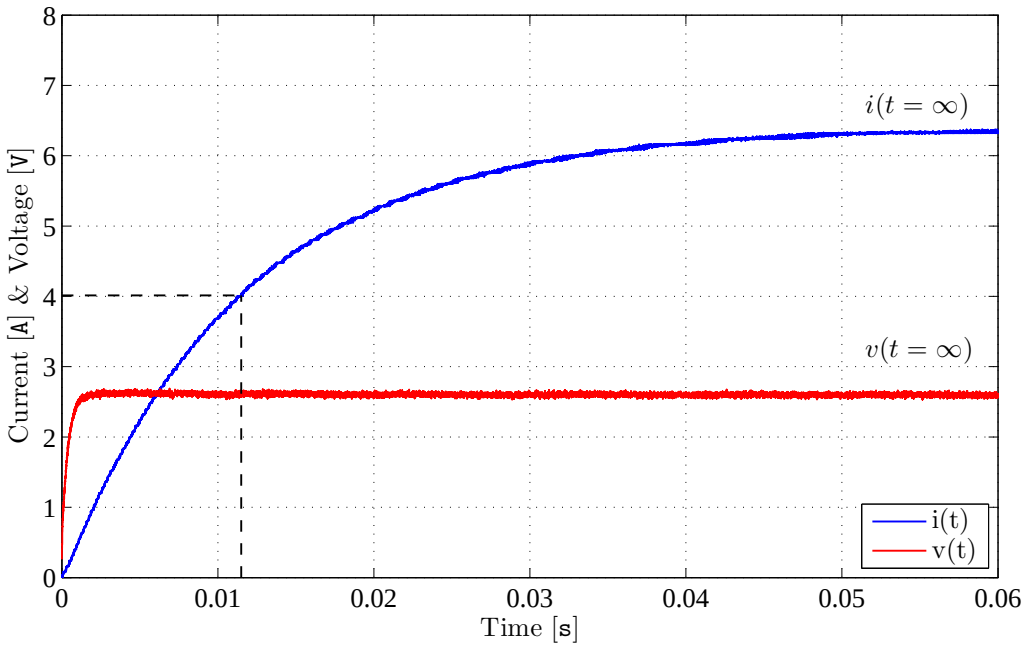

Figure A.2. Current and voltage waveform of the equivalent circuit when the rotor is locked to the d-axis. The dotted line indicates the time constant.

Rotor Magnetic Flux

The rotor flux linkage λ_{pm} or Back-EMF (BEMF) constant represent a ratio between the BEMF and the mechanical angular frequency. By measuring the no load PMSM line-to-line voltage while it is driven through the shaft at a known constant speed n_m, the rotor flux linkage is calculated using (A.3)

$$\lambda_{pm} = \sqrt{\frac{2}{3}}\frac{V_{ltl}}{\omega_r}\,,\ \omega_r = P_p n_m \frac{2\pi}{60} \quad [\mathtt{Wb}] \tag{A.3}$$

where:
V_{ltl} is the line-to-line RMS voltage [V]
ω_r is the electrical angular frequency of the induced voltage [rad/s]
n_m is the mechanical rotor speed [$\mathtt{min}^{-1}$]

The line-to-line voltage is measured using a multimeter connected to two phases of the PMSM, and the mechanical speed using a tachometer. The measurement is most precise at speeds close to rated speed, since the voltage measurement error is lower at high speeds compared to low speeds.

Mechanical Parameters

The mechanical parameters needed for vector control of the PMSM are listed in Table A.2.

Table A.2. Mechanical parameters of the PMSM system.

Required mechanical parameters		
Parameter	**Dimension**	**Description**
B_m	[Ns/m]	Viscous damping coefficient
J_m	[kg·$\mathtt{m}^2$]	System inertia coefficient
J_0	[Nm]	Coulomb friction coefficient

By following the procedures given in the next sections the mechanical parameters can be determined.

Viscous Damping and Coulomb Friction

Based upon the equation of motion of the PMSM mechanical system which is repeated in (A.4) it is possible to determine the mechanical constants.

$$T_e = T_l + B_m\omega_m + J_0 + J_m\frac{d}{dt}\omega_m \quad [\mathtt{Nm}] \tag{A.4}$$

The viscous damping B_m represents a torque opposite to the electromagnetic torque, which is proportional to the angular speed of the rotor. It can be identified together with the Coulomb friction which is independent of the magnitude of the speed, considering that (A.4) reduces to (A.5), when the angular speed is constant and no load torque is applied.

$$T_e = B_m\omega_m + J_0 \quad [\mathtt{Nm}] \tag{A.5}$$

By stepping up the speed of the PMSM and measuring the necessary electromagnetic torque according to (2.14) when the speed is constant, it is possible to obtain the linear coherence between the electromagnetic torque, the viscous damping and the Coulomb friction, and hence identify the viscous damping and Coulomb friction using a linear curve fit as shown in Figure A.3.

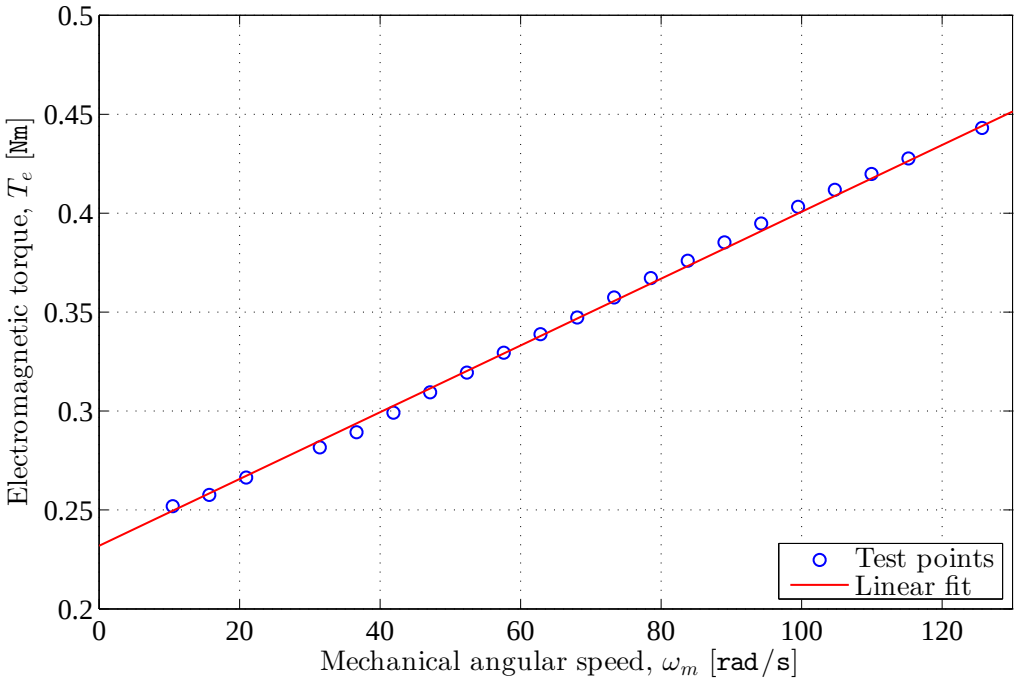

Figure A.3. Electromagnetic torque vs. mechanical angular speed used to identify the viscous damping and Coulomb friction.

Inertia

The inertia coefficient describes the resistance against movement of the mechanical system under speed changes, and is the dominating transient component. After identifying the viscous damping and coulomb friction, the inertia coefficient can be determined by a coast down test. To characterize the inertia J_m the rotor is accelerated up to an initial speed ω_{m0} and the rotational speed ω_m is measured as the rotor coasts to a stop. Using this measured result, the rotor inertia can be identified by curve fitting to (A.6) which describes the mechanical behaviour of the system, when it experience a coast down and the electromagnetic torque T_e and load torque T_l are zero.

$$\omega_m = \left(\omega_{m0} + \frac{J_0}{B_m}\right)e^{-\frac{B_m}{J_m}t} - \frac{J_0}{B_m} \quad [\mathtt{rad/s}] \tag{A.6}$$

where:
ω_m is the rotational speed of the shaft
ω_{m0} is the initial rotational speed of the shaft

In Figure A.4 the coast down test and the curve fitting under a test procedure are shown.

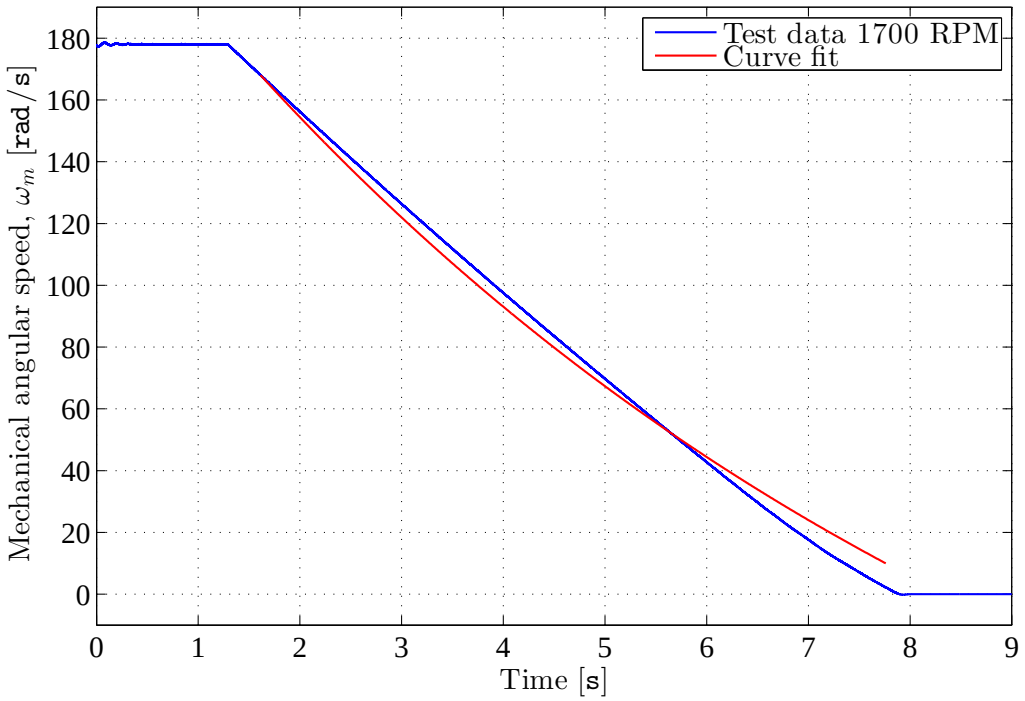

Figure A.4. Rotor speed during a coast down speed test with curve fitting.

Appendix B
PI Control Model

The Simulink model developed for the simulation of the classical FOC PI current controller is shown in Figure B.1.

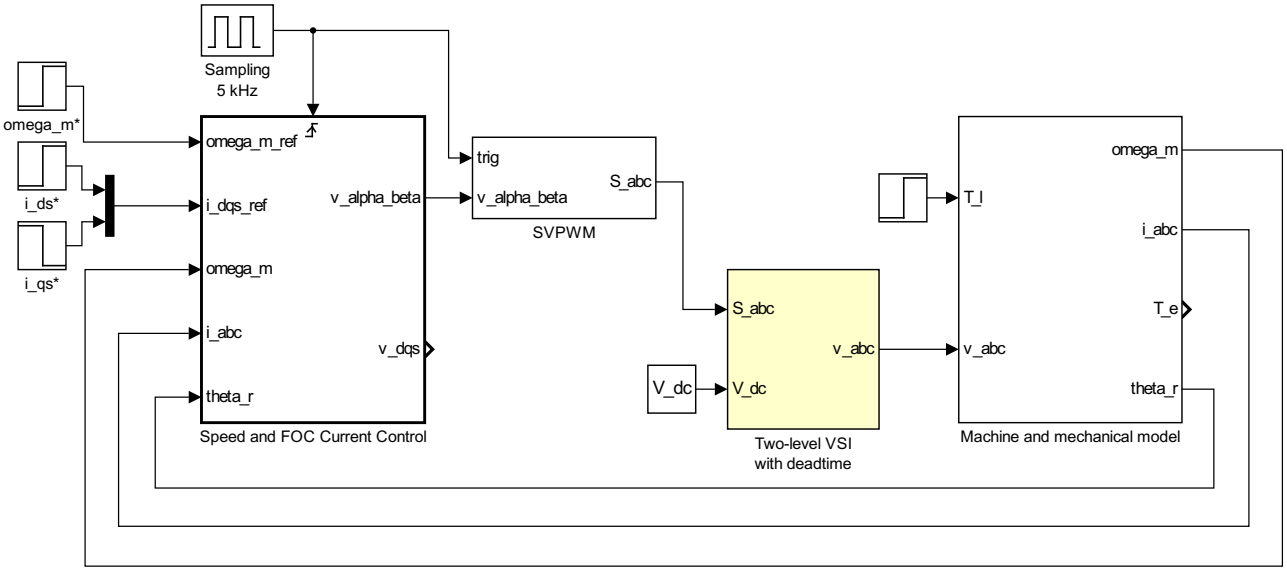

Figure B.1. Complete Simulink FOC PI controller model.

Inside the speed and FOC current control block, which is a sampled sub-system, the developed PI current controllers are found together with the developed speed controller. The content inside the block is shown in Figure B.2.

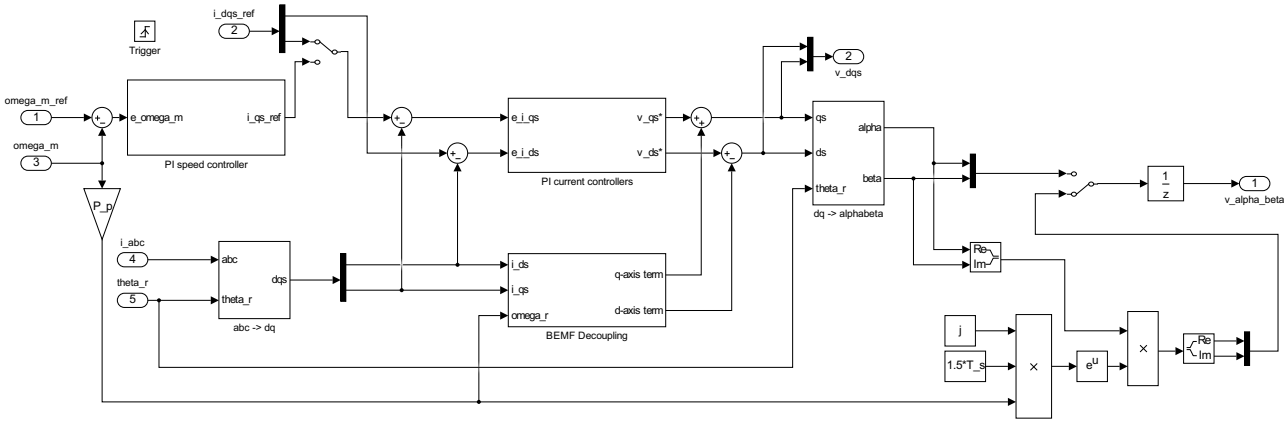

Figure B.2. Speed and FOC current controller model.

The two PI controller blocks consists of the controller gains, a discrete time integrator block and the anti-windup scheme shown in Section 3.5. The DSP delay is modelled as a unit delay. The inverter block is modelled with dead-time using PLECS, and is shown in Figure B.3.

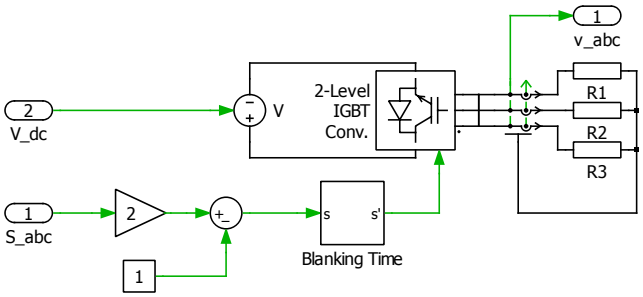

Figure B.3. PLECS inverter model with dead-time.

The voltages are generated by measuring the line-to-neutral voltage as shown in the PLECS model. The contents of the machine- and mechanical model are shown in Figure B.4.

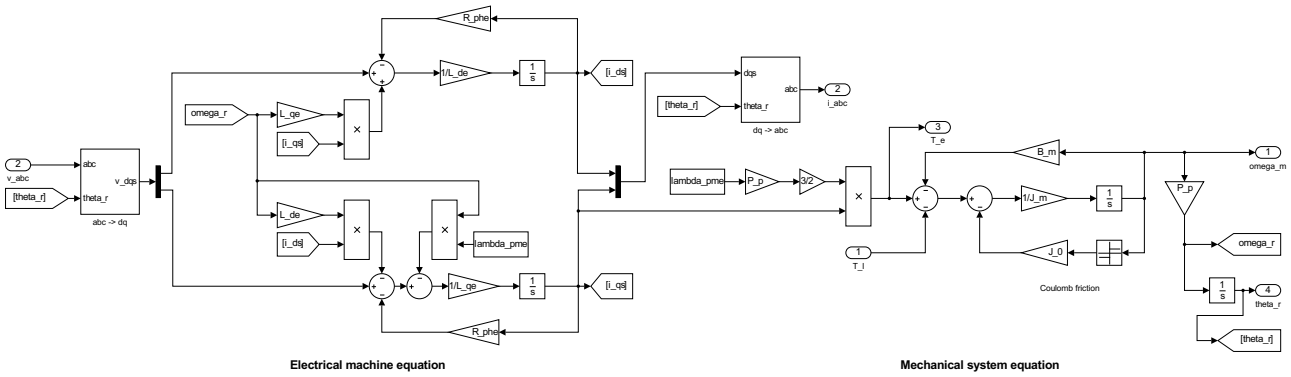

Figure B.4. Machine- and mechanical model.

The d- and q-axis voltage equations are modelled to the left in Figure B.4, while the mechanical system equation is modelled to the right. Inside the SVPWM block, which is also a sampled subsystem, the developed SVPWM signal generation for the PLECS inverter is found. Its content is shown in Figure B.5.

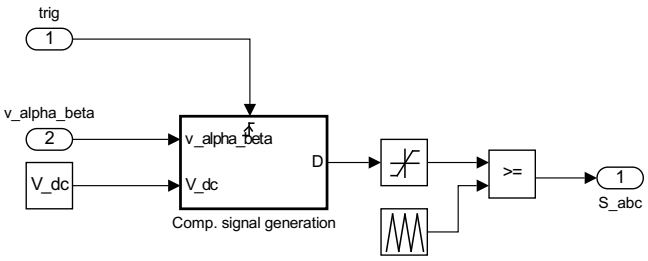

Figure B.5. SVPWM model.

Inside the compare signal generation block two MATLAB functions are found. The MATLAB codes for generating the compare signals are shown in Listings B.1 and B.2.

Listing B.1. MATLAB code: generates the duty cycles for the corresponding sector.

```
% Sector number determination
function duty = sector(v_alpha_beta,V_dc)

arg=atan2(v_alpha_beta(2),v_alpha_beta(1));
mag=hypot(v_alpha_beta(1),v_alpha_beta(2));

if arg>=0 & arg<pi/3
        n=1;
    elseif arg>=pi/3 & arg<2*pi/3
        n=2;
```

```
    elseif arg>=2*pi/3 & arg<pi
        n=3;
    elseif arg>=-pi & arg<-2*pi/3
        n=4;
    elseif arg>=-2*pi/3 & arg<-pi/3
        n=5;
    else arg>=-pi/3 & arg<0
        n=6;
end
% Calculation of the duty cycles
d_x = ((mag*sqrt(3))/V_dc)*sin((n/3)*pi-arg);
d_y = ((mag*sqrt(3))/V_dc)*sin(arg-((n-1)/3)*pi);
d_0 = 1-d_x-d_y;
duty = [d_x+d_y+d_0, d_x, d_y, d_0, n];
```

Listing B.2. MATLAB code: generates the compare signals.

```
function D = comp(u)
n=u(5); d_x=u(2); d_y=u(3); d_0=u(1);

if n==1
    D_a = (d_x+d_y);
    D_b = (-d_x+d_y);
    D_c = (-d_x-d_y);
elseif n==2
    D_a = (d_x-d_y);
    D_b = (d_x+d_y);
    D_c = (-d_x-d_y);
elseif n==3
    D_a = (-d_x-d_y);
    D_b = (d_x+d_y);
    D_c = (-d_x+d_y);
elseif n==4
    D_a = (-d_x-d_y);
    D_b = (d_x-d_y);
    D_c = (d_x+d_y);
elseif n==5
    D_a = (-d_x+d_y);
    D_b = (-d_x-d_y);
    D_c = (d_x+d_y);
else n==6
    D_a = (d_x+d_y);
    D_b = (-d_x-d_y);
    D_c = (d_x-d_y);
end

D = 0.5*(1+[D_a, D_b, D_c]);
```

The contents presented in this appendix make up the complete Simulink model of the FOC PI Controller.

Appendix C
Predictive Deadbeat Control Model

The Simulink model developed for the simulation of the predictive deadbeat current controller is shown in Figure C.1.

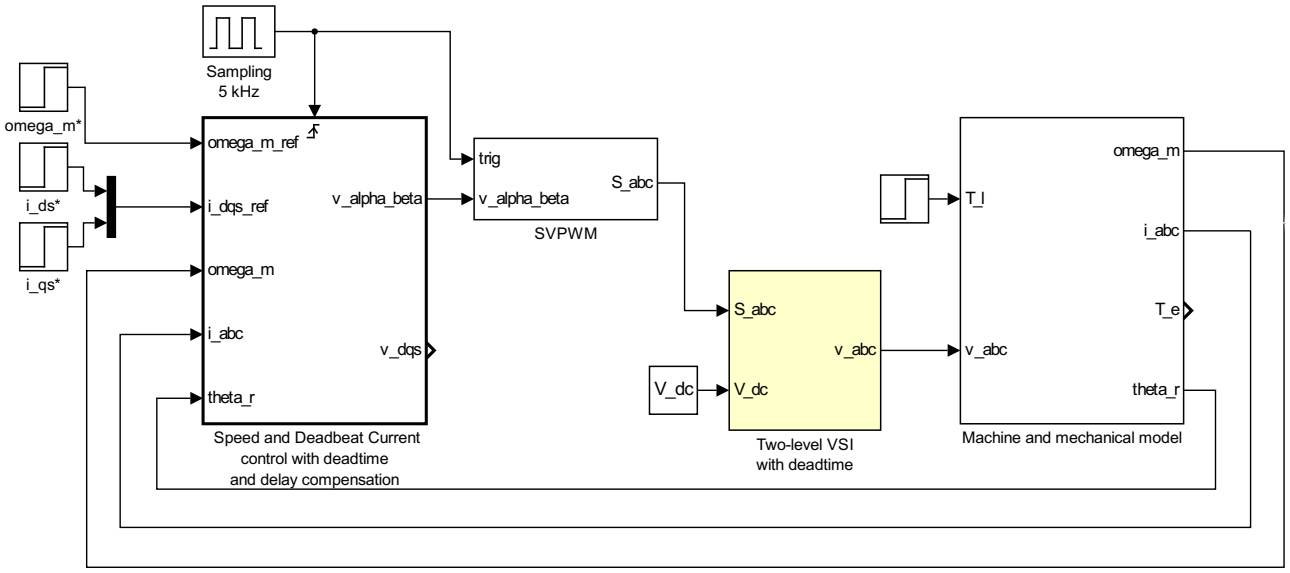

Figure C.1. Complete Simulink FOC predictive deadbeat controller model.

As seen the model is identical to the FOC PI controller model. The predictive controller has replaced the PI current controllers inside the controller block which is shown in Figure C.2.

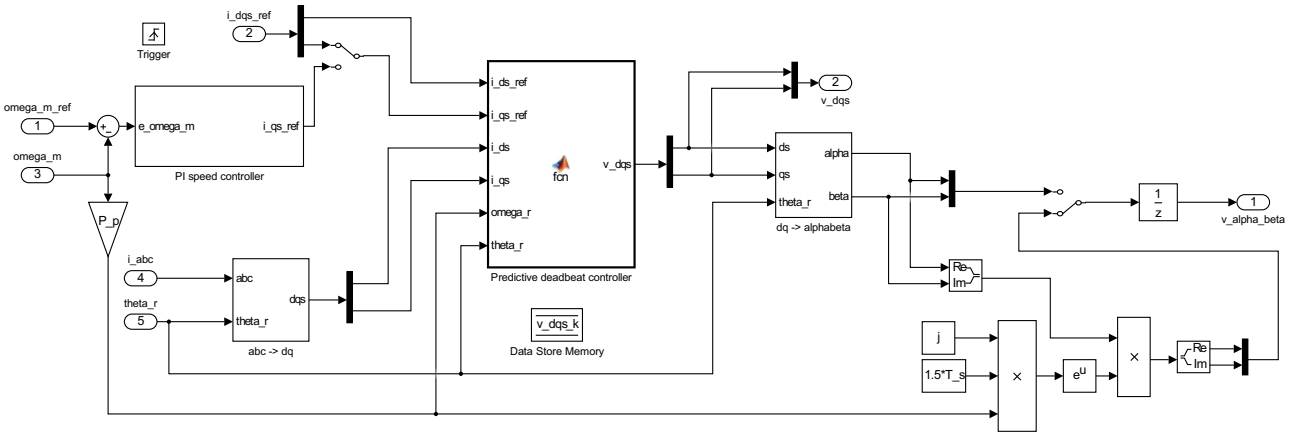

Figure C.2. Speed PI- and predictive deadbeat current controller.

The MATLAB code contained inside the MATLAB function block generates the predictive deadbeat control voltages and is shown in Listing C.1.

Listing C.1. MATLAB code: generates the predictive deadbeat voltages according to chapter 4.

```
function v_dqs = fcn(i_ds_ref, i_qs_ref, i_ds, i_qs, omega_r, theta_r, V_dc, R_ph, ...
    L_d, L_q, lambda_pm, T_s, T_dead)

% Initialisation (loading current voltage at k)
global v_dqs_k;

% Discretized motor model (predicts currents to k+1)
i_ds_kp1 = (T_s/L_d)*v_dqs_k(1,1) + i_ds - ((R_ph*T_s)/L_d)*i_ds + ...
    (T_s/L_d)*(omega_r*L_q)*i_qs;
i_qs_kp1 = (T_s/L_q)*v_dqs_k(2,1) + i_qs - ((R_ph*T_s)/L_q)*i_qs - ...
    (T_s/L_q)*(omega_r*L_d)*i_ds - (T_s/L_q)*omega_r*lambda_pm;

% Predicted deadbeat control voltages (output for k+1)
v_ds_db_kp1 = (L_d/T_s)*(i_ds_ref-i_ds_kp1) + R_ph*i_ds_kp1 - omega_r*L_q*i_qs_kp1;
v_qs_db_kp1 = (L_q/T_s)*(i_qs_ref-i_qs_kp1) + R_ph*i_qs_kp1 + omega_r*L_d*i_ds_kp1 + ...
    omega_r*lambda_pm;

% Deadtime compensation voltages
delta_V = (T_dead*V_dc)/(T_s);
ang_ref = atan2(i_qs_ref,i_ds_ref);

if i_ds_ref==0 && i_qs_ref==0
    v_ds_comp = (4/3) * delta_V * sin( (pi/3) * floor( (theta_r+0+(pi/6)) / (pi/3) ) ...
        - theta_r );
    v_qs_comp = (4/3) * delta_V * cos( (pi/3) * floor( (theta_r+0+(pi/6)) / (pi/3) ) ...
        - theta_r );
else
    v_ds_comp = (4/3) * delta_V * cos( (pi/3) * floor( (theta_r+ang_ref+(pi/6)) / ...
        (pi/3) ) - theta_r );
    v_qs_comp = (4/3) * delta_V * sin( (pi/3) * floor( (theta_r+ang_ref+(pi/6)) / ...
        (pi/3) ) - theta_r );
end

% Addition of dead-time compensation voltages
v_ds = v_ds_db_kp1 + v_ds_comp;
v_qs = v_qs_db_kp1 + v_qs_comp;

% Deadbeat voltage constraint
if hypot(v_ds,v_qs) > V_dc/sqrt(3);
    v_ds = ((V_dc/sqrt(3))/hypot(v_ds,v_qs))*v_ds;
    v_qs = ((V_dc/sqrt(3))/hypot(v_ds,v_qs))*v_qs;
    v_dqs = [v_ds; v_qs;];
else
    v_dqs = [v_ds; v_qs;];
end

% Store voltage vector
v_dqs_k = [v_ds_db_kp1; v_qs_db_kp1;];

v_dqs = [v_ds; v_qs;];
```

The contents presented in this appendix make up the complete predictive deadbeat controller Simulink model. The machine- and mechanical model, inverter model, and SVPWM model are identical to the models presented in Appendix B.